TECHNISCHE
UNIVERSITÄT
WIEN
Vienna University of Technology

Diplomarbeit

Coupled DEM-CFD Simulation of a Sinter Shaft Cooler

ausgeführt zum Zwecke der Erlangung des akademische Grades

Master of Science

Unter der Leitung von

Univ.Prof. Dipl.-Ing. Dr.techn. Markus Haider
E302 - Institut für Energietechnik und Thermodynamik

In Kooperation mit
ENRAG GmbH
Primetals Technologies Austria GmbH

eingereicht an der Technischen Universität Wien
Fakultät für Maschinenwesen und Betriebswissenschaften

Harald Unger
E 066 445/0928805
An den Kohlenrutschen 12/1/12, 1020 Wien

Wien, May 11, 2016

Die approbierte gedruckte Originalversion dieser Diplomarbeit ist an der TU Wien Bibliothek verfügbar
The approved original version of this thesis is available in print at TU Wien Bibliothek.
TU Bibliothek Your knowledge hub WIEN

Ich habe zur Kenntnis genommen, dass ich zur Drucklegung meiner Arbeit unter der Bezeichnung

Diplomarbeit

nur mit Bewilligung der Prüfungskommission berechtigt bin.

Ich erkläre weiters an Eides statt, dass ich meine Diplomarbeit nach den anerkannten Grundsätzen für wissenschaftliche Abhandlungen selbstständig ausgeführt habe und alle verwendeten Hilfsmittel, insbesondere die zugrunde gelegte Literatur, genannt habe.

Weiters erkläre ich, dass ich dieses Diplomarbeitsthema bisher weder im In- noch Ausland (einer Beurteilerin/einem Beurteiler zur Begutachtung) in irgendeiner Form als Prüfungsarbeit vorgelegt habe und dass diese Arbeit mit der vom Begutachter beurteilten Arbeit übereinstimmt.

Wien, May 11, 2016

Harald Unger

Die approbierte gedruckte Originalversion dieser Diplomarbeit ist an der TU Wien Bibliothek verfügbar
The approved original version of this thesis is available in print at TU Wien Bibliothek.
TU Bibliothek Your knowledge hub WIEN

Die approbierte gedruckte Originalversion dieser Diplomarbeit ist an der TU Wien Bibliothek verfügbar
The approved original version of this thesis is available in print at TU Wien Bibliothek.

Acknowledgment

First of all, I would like to express my gratitude to Dr. Roland Eisl, CEO of ENRAG GmbH, who made this work possible. He was an enthusiastic supervisor and I was able to benefit from numerous fascinating discussions. Because of his expertise and competence in the field of numerical simulations he provided useful feedback and spurred me to complete this thesis. Furthermore, I am thankful to my colleagues for the exchange of ideas and the pleasant working environment.

I would like to thank Primetals Technologies Austria GmbH for providing the enormously fascinating and likewise challenging topic for this thesis. A special thanks goes to Dr. Michaela Böberl, who was a reliable contact person at the company and provided professional guidance whenever necessary.

I am grateful to Univ. Prof. Dr. Markus Haider, head of the Institute of Energy Systems and Thermodynamics at the Vienna University of Technology, for his efforts in supervising and contributing to this thesis.

I would like to express my appreciation to Wolfgang Steindl, who was a brilliant colleague and friend during the time at school and university. He was always a cheerful and extremely professional associate.

I am deeply thankful to Milena Viviana Fumarola for her understanding and great patience regarding my work. She was a big support and this thesis would not have been possible in the present form without her.

Last but not least, I would like to thank my family and friends for their encouragement and aid during my studies and thesis. I am especially grateful to my parents, Christa and Gerhard, who supported me in every possible way.

Die approbierte gedruckte Originalversion dieser Diplomarbeit ist an der TU Wien Bibliothek verfügbar
The approved original version of this thesis is available in print at TU Wien Bibliothek.

Abstract

In this work the application possibility of the Discrete Element Method (DEM) to enhance the development process of a cross-flow sinter cooler is examined. Through coupling with Computational Fluid Dynamics (CFD), the momentum exchange and convective heat transfer between the solid and fluid phase can be simulated. This enables the reproduction of granular flow phenomena such as segregation and the prediction of the pressure drop across the packed bed as well as the heat exchange between particles and fluid.

An open source software framework consisting of LIGGGHTS, OpenFOAM and CFDEMcoupling is used for the numerical calculations. The provided incompressible coupled solver is modified to account for the influence of temperature on fluid density and velocity field. Test simulations are performed to verify basic requirements such as mass and energy conservation of the extended solver.

The computation time of DEM simulations depends intrinsically on the number of particles in the simulation domain. Numerous techniques were developed to increase the computational efficiency. In this work, coarse-graining is used to scale up the particle diameter and consequently reduce the number of particles in the domain. Moreover, the particle-size distribution is truncated to exclude the large particles as a limiting factor on the coarse-graining approach.
One of the fundamental problems related to the simulation of industrial processes with a coupled DEM-CFD method are different time-scales. The residence time of a particle in the sinter cooler can be in the scope of hours, while the time-step size of DEM simulations is in the range of milliseconds or even microseconds. Thus, a time-scaling approach is used to speed up the granular flow and reduce the processing time significantly.
To decrease the computational effort even further, the three-dimensional geometry is reduced to a quasi-axisymmetric representation.

On the basis of the above mentioned modeling techniques, coupled DEM-CFD simulations are successfully applied to investigate the processes inside the sinter cooler. The trajectory of the particles through the shaft cooler facility is illustrated as well as segregation effects and formation of dead zones. It is shown that the coupled approach is suitable for prediction of the pressure drop across the packed bed and the temperature field of the cooling air and the sinter material in a plausible manner. Additionally, velocity peaks and the reason for their appearance are identified.
A plausibility check is performed by comparison of the simulation results with an existing calculation tool for the shaft cooler facility written in Excel-VBA. This confrontation demonstrates the shortcomings of the applied modeling approaches in the coupled DEM-CFD simulation and permits the assessment of associated errors.
Eventually the combination of different modeling techniques provides a feasible method to improve and expedite the development process of the innovative counter-flow sinter cooler.

Die approbierte gedruckte Originalversion dieser Diplomarbeit ist an der TU Wien Bibliothek verfügbar
The approved original version of this thesis is available in print at TU Wien Bibliothek.

Kurzfassung

In dieser Arbeit werden die Anwendungsmöglichkeiten der Diskreten Elemente Methode (DEM) zur Verbesserung des Entwicklungsprozesses eines Gegenstrom-Sinterkühlers untersucht. Durch Koppelung mit einer numerischen Strömungssimulation (CFD) kann der Impulsaustausch und der konvektive Wärmeübergang zwischen fester und fluider Phase simuliert werden. Dies ermöglicht die Untersuchung von Phänomenen in granularen Strömungen, wie beispielsweise Segregation, sowie eine Abschätzung des Druckabfalls in der Schüttung und den Wärmeaustausch zwischen den Partikeln und dem Fluid.

Ein Open-Source Software Gerüst bestehend aus LIGGGHTS, OpenFOAM und CFDEMcoupling wird für die numerischen Berechnungen verwendet. Der bereitgestellte inkompressible, gekoppelte Löser wird modifiziert, um den Temperatureinfluss auf die Fluiddichte und das Geschwindigkeitsfeld zu berücksichtigen. Testläufe werden durchgeführt, um Grundanforderungen wie Massen- und Energieerhaltung des erweiterten Lösers zu überprüfen.

Die Rechenzeit von DEM Simulationen ist untrennbar mit der Anzahl der Partikel im Simulationsbereich verbunden, daher wurden zahlreiche Techniken entwickelt um die Recheneffizienz zu steigern. Eine Coarse-graining Methode wird angewendet um den Partikeldurchmesser maßstäblich zu vergrößern und folglich die Anzahl der Partikel im Simulationsgebiet zu verringern. Weiters wird die Partikelgrößenverteilung reduziert, um die großen Partikel als Begrenzungsfaktor für das Coarse-graining auszuschließen. Die unterschiedlichen Zeitskalen stellen ein wesentliches Problem in Bezug auf die Simulation von industriellen Prozessen dar. Die Aufenthaltsdauer eines Partikels im Sinterkühler kann sich auf Stunden belaufen, während die Größe des Zeitschrittes für die DEM Simulation im Bereich von Milli- oder sogar Mikrosekunden liegt. Daher wird eine Zeitskalierungsmethode angewendet, um die granulare Strömung zu beschleunigen und die Rechenzeit deutlich zu verkürzen. Zur weiteren Verringerung des Rechenaufwandes wird die dreidimensionale Geometrie auf eine quasi-achsensymmetrische Darstellung reduziert.

Auf Basis der oben angeführten Modellierungstechniken werden die gekoppelten DEM-CFD Simulationen erfolgreich angewendet, um die Prozesse innerhalb des Sinterkühlers zu untersuchen. Sowohl die Bewegungsbahn der Partikel als auch Segregationseffekte und die Ausbildung von Totzonen werden abgebildet. Die gekoppelte Berechnung ist geeignet um den Druckabfall durch die Schüttung und das Temperaturfeld der Kühlluft und des Sintermaterials plausibel darzustellen. Weiters können damit Geschwindigkeitsspitzen identifiziert werden.

Eine Plausibilitätsprüfung der Simulationsergebnisse wird anhand des Vergleichs mit einem bestehenden Berechnungstool für die Schachtkühleranlage, welches in Excel-VBA implementiert ist, durchgeführt. Diese Gegenüberstellung zeigt die Defizite der angewendeten Modellierungsansätze auf und erlaubt eine Bewertung der damit verbundenen Fehler.
Schlussendlich bietet die Kombination unterschiedlicher Modelle eine praktikable Methode um den Entwicklungsprozess des innovativen Gegenstrom-Sinterkühlers zu verbessern und voranzutreiben.

Die approbierte gedruckte Originalversion dieser Diplomarbeit ist an der TU Wien Bibliothek verfügbar
The approved original version of this thesis is available in print at TU Wien Bibliothek.

Contents

1. Introduction **1**
1.1. Sinter Cooling Plants . . . 1

2. Granular Materials **2**
2.1. Modeling of Granular Materials . . . 2
2.1.1. Segregation . . . 3
2.2. Numerical Simulations of Granular Materials . . . 4
2.2.1. Force-Based Molecular Dynamics (MD) . . . 4
2.2.2. Event-Driven Molecular Dynamics . . . 4
2.2.3. Direct Simulation Monte Carlo (DSMC) . . . 5
2.2.4. Combined Finite-Discrete Element Method . . . 5
2.2.5. Other Simulation Methods . . . 5

3. Discrete Element Method (DEM) **6**
3.1. Equations of Motion . . . 6
3.2. Time-Integration Schemes . . . 6
3.2.1. Velocity-Verlet Scheme . . . 7
3.2.2. Time-Step Estimation . . . 8
3.3. Contact Model for Spherical Particles . . . 9
3.3.1. Normal and Tangential Forces . . . 9
3.3.2. Hertz-Mindlin Contact Model . . . 12
3.4. Rolling-Friction Model . . . 13
3.4.1. Constant Directional Torque (CDT) . . . 13
3.4.2. Elastic-Plastic Spring-Dashpot (EPSD) . . . 13
3.4.3. EPSD Formulation . . . 14
3.5. Conductive Heat Transfer . . . 15
3.6. Non-Contact Forces . . . 16
3.7. Neighbor List Algorithm . . . 16
3.7.1. Verlet Lists . . . 17
3.7.2. Cell Linked Algorithm . . . 17
3.7.3. Combined Approach . . . 17
3.8. Non-spherical particle shape . . . 18

4. Speed-Up of DEM Simulations **19**
4.1. Algorithms . . . 19
4.1.1. Neighbor Lists . . . 19
4.1.2. Parallelization . . . 19
4.1.2.1. Static Domain Decomposition . . . 19

Die approbierte gedruckte Originalversion dieser Diplomarbeit ist an der TU Wien Bibliothek verfügbar
The approved original version of this thesis is available in print at TU Wien Bibliothek.

4.1.2.2. Dynamic Load Balancing . . . 20
4.2. Modeling Approach . . . 20
4.2.1. Coarse-Graining . . . 21
4.2.2. Young's Moldulus . . . 22
4.2.3. Density-Scaling . . . 22
4.2.4. Time-Scaling . . . 23

5. Software **24**
5.1. LIGGGHTS and CFDEMcoupling . . . 24
5.2. Drawbacks in LIGGGHTS-PUBLIC . . . 25

6. DEM-CFD Coupling **26**
6.1. Computation Fluid Dynamics (CFD) . . . 26
6.2. Coupling Approach . . . 26
6.2.1. Unresolved DEM-CFD Coupling . . . 27
6.2.2. Resolved DEM-CFD Coupling . . . 27
6.3. Solver Modifications . . . 27
6.3.1. Void Fraction . . . 28
6.3.2. Relative Density . . . 28
6.3.3. Incompressible Ideal Gas Law . . . 29
6.4. Governing Equations . . . 30
6.4.1. Continuity Equation . . . 30
6.4.2. Momentum Equation . . . 30
6.4.3. Energy Equation . . . 34
6.5. Coarse-Graining Correction . . . 38
6.5.1. Momentum Equation . . . 39
6.5.2. Energy Equation . . . 39
6.6. Time-Scaling Correction . . . 40

7. Solver Verification **42**
7.1. Coarse-Graining . . . 42
7.1.1. Fluidization Test Case . . . 42
7.1.2. Convection Test Case . . . 45
7.2. Cold Model . . . 47
7.3. Mass Conservation . . . 48
7.4. Energy conservation . . . 49

8. Objectives **51**
8.1. Objectives of the DEM Simulations . . . 51
8.2. Objectives of the Coupled DEM-CFD Simulations . . . 51

Die approbierte gedruckte Originalversion dieser Diplomarbeit ist an der TU Wien Bibliothek verfügbar
The approved original version of this thesis is available in print at TU Wien Bibliothek.

9. Excel-Tool **53**

10. Simulation Setup **55**
10.1. Geometry . . . 55
10.2. Particle-Size Distribution (PSD) . . . 56
10.3. Solid Material Properties . . . 57
10.4. Fluid Material Properties . . . 58
10.5. Boundary Conditions . . . 59
10.5.1. Turbulent Boundary Conditions . . . 59
10.6. Time-Step Settings . . . 60
10.6.1. CFL condition . . . 61
10.7. CFD Mesh . . . 61

11. DEM Simulation Results **63**
11.1. Angle of Repose Test . . . 63
11.2. Discharging Test . . . 64
11.3. Segregation Analysis . . . 66
11.4. Dead Zones . . . 68
11.5. Particle Trajectories . . . 69

12. Coupled DEM-CFD Simulation Results **72**
12.1. Verification of the Simulation Results . . . 72
12.1.1. Critical Review of the Quasi-Axisymmetric Representation . . . 72
12.1.2. Excel-Tool vs. DEM-CFD Simulation . . . 74
12.2. DEM-CFD Results for PSD-B . . . 75

13. Conclusion and Outlook **81**
13.1. Model Assumptions . . . 81
13.1.1. Solid Flow . . . 81
13.1.2. Fluid Flow and Heat Transfer . . . 82
13.2. Improvements and Future Work . . . 82

A. Nomenclature **84**
A.1. List of Abbreviations and Acronyms . . . 84
A.2. List of Symbols . . . 84

B. Governing Equations for Multiphase Flows **88**
B.1. Compressible . . . 88
B.2. Incompressible . . . 88

Die approbierte gedruckte Originalversion dieser Diplomarbeit ist an der TU Wien Bibliothek verfügbar
The approved original version of this thesis is available in print at TU Wien Bibliothek.

C. Material Properties **90**
C.1. Solid Material Properties 90
C.2. Fluid Material Properties 92

Bibliography **94**

Die approbierte gedruckte Originalversion dieser Diplomarbeit ist an der TU Wien Bibliothek verfügbar
The approved original version of this thesis is available in print at TU Wien Bibliothek.

List of Figures

2.1. Segregation of particles on an established pile due to different particle size. . . . 3
2.2. Comparison of numerical simulation methods in terms of computational costs and accuracy [8], [14]. . . . 5

3.1. Schematic illustration of the forces acting on particle i from contacting particle j and non-contacting particle k (capillary force here), from [12]. . . . 7
3.2. Spring-dashpot model for normal (left) and tangential (right) contact forces, from [13]. . . . 10
3.3. Breakdown of a particle collision into different stages. Attractive forces due to the artificial force effect are highlighted in boxed notation, from [8]. . . . 11
3.4. Methods to resolve non-spherical particle shapes. . . . 18

4.1. Decomposition of the simulation domain into sub-areas and boundaries for data exchange between processes, from [8]. . . . 20
4.2. Static domain decomposition (left) compared to domain composition with dynamic load balancing (right), from [11]. . . . 21

6.1. Comparison of unresolved (left) and resolved (right) DEM-CFD method with regard to the relation of cell and particle size. . . . 28
6.2. Comparison of the laminar and the turbulent part of the Ergun equation for $d_p = 0.022\,\mathrm{m}$, $\rho_f = 1.293\,\mathrm{kg/m^3}$, $\nu_f = 1.5 \times 10^{-5}\,\mathrm{m^2/s}$, $L = 0.9\,\mathrm{m}$, $\alpha_f = 0.434\,75$ and $\Phi = 1$. . . . 33
6.3. Nusselt number with dependece on the void fraction for $Re = 50$ and $Pr = 0.7$. . 37
6.4. Nusselt number with dependece on the void fraction for $Re = 5000$ and $Pr = 0.7$. 38

7.1. Fluidization test case setup. . . . 42
7.2. Snapshot of the fluidization test case comparing different particle sizes with regard to coarse-graining correction. . . . 43
7.3. Average height of the free surface between the particulate and fluid phase with regard to particle size and coarse-graining correction. . . . 44
7.4. Pressure drop across the fluidized bed with regard to particle size for activated coarse-graining correction. . . . 45
7.5. Particle column geometry and snapshot of the particle temperature distribution for the convection test case at $t = 1.5\,\mathrm{s}$. . . . 46
7.6. Plot of the fluid temperature distribution of the convective test case a $t = 1.5\,\mathrm{s}$. . 47
7.7. Plot of the fluid temperature profile across the column height. . . . 48
7.8. Plot of the fluid temperature at the outlet boundary over time. . . . 50

9.1. Geometry, mesh and pressure contour plot of the Excel-tool. . . . 54

Die approbierte gedruckte Originalversion dieser Diplomarbeit ist an der TU Wien Bibliothek verfügbar
The approved original version of this thesis is available in print at TU Wien Bibliothek.

10.1. Shaft cooler geometry. 56
10.2. Hexahedral CFD mesh and detailed view of the mesh cell size compared to the largest particle size of PSD-B. 62

11.1. Comparison of rolling-friction models with regard to the angle of repose on a flat plane. 64
11.2. Comparison of the mirrored quasi-axisymmetric geometry (left) and the symmetric geometry (right), both filled up with particles. 65
11.3. Comparison of the normalized number of particles inside the shaft cooler during the discharging test. 65
11.4. Snapshot of segregated particle flows for PSD-B (left), PSD-C (middle) and PSD-D (right) with indication of the supply chute exit and the geometrical bottleneck. 66
11.5. Time-averaged segregation analysis for the truncated particle-size distributions. . 67
11.6. Solid velocity contour plot with a region of low velocity magnitude (1) and two dead zones (2) and (3). 69
11.7. Particle trajectories for different particle-size distributions (in magenta) and particle ID (transparent). 70

12.1. Progression of the pressure drop across the sinter bed in the shaft cooler for a velocity boundary condition of 0.25 m/s at the outer air inlet. 74
12.2. Progression of the pressure drop across the sinter bed in the shaft cooler for a velocity boundary condition of 0.25 m/s at the outer and 0.20 m/s at the inner air inlet. 76
12.3. Contour plots of the time-averaged fluid data and particle temperature field. . . 77
12.4. Velocity vector plot and streamline plot for the fluid phase and time-averaged solid velocity contour plot. 78
12.5. Solid velocity profile at various heights of the sinter cooler, the heights are specified in the vertical axis of Figure 12.4 (b). 80

C.1. Thermal conductivity of the sinter as a function of temperature. 91
C.2. Thermal capacity of the sinter as a function of temperature. 91
C.3. Dynamic viscosity of dry air as a function of temperature. 92
C.4. Thermal conductivity of dry air as a function of temperature. 93
C.5. Specific heat capacity of dry air as a function of temperature. 93

Die approbierte gedruckte Originalversion dieser Diplomarbeit ist an der TU Wien Bibliothek verfügbar
The approved original version of this thesis is available in print at TU Wien Bibliothek.

List of Tables

6.1. Temperature dependence of the material properties for dry air, from [57]. 32

7.1. Solid material properties for the fluidization test case. 43
7.2. Time-averaged fluidization height with regard to particle diameter (d_p), coarse-graining correction deactivated (h_1) or activated (h_2), and area-averaged pressure drop (Δp) at the end of the simulation time for activated coarse-graining correction. 45
7.3. Fluid and solid material properties for the convection test case. 46
7.4. Fluid material properties for the cold model test case. 47
7.5. Summary of the test cases for conservation of mass. 49

10.1. Particle-size distribution based on mass and numbers. 57
10.2. Truncated particle-size distributions used for the DEM and coupled DEM-CFD simulations with the corresponding coarse-graining factor and the number of particles. 57
10.3. Composition of the sinter material in mass-percent, dry analysis. 58
10.4. Material properties of the particles (p), the walls (w) and the symmetry axis (s). 58
10.5. Material parameters of the Hertz contact model and the EPSD rolling-friction model for particle-particle (p-p), particle-wall (p-w) and particle-symmetry axis (p-s) interaction. 59
10.6. Fluid material properties for dry air. 59
10.7. Boundary conditions for the coupled DEM-CFD simulation. 60
10.8. Default turbulence model coefficients of the incompressible realizable k-ε model in OpenFOAM. 60
10.9. Selected time-step sizes for the DEM, CFD and coupled DEM-CFD simlation with regard to the employed particle-size distribution and the resulting fraction of the Rayleigh-time $\Delta t/t_R$ and Hertz-time $\Delta t/t_H$. 61

11.1. Through-put time of selected particles in minutes. The particle-size ratio with respect to the smallest particle of the PSD is specified in brackets. 71

12.1. Differences between the Excel-tool and the coupled DEM-CFD simulation. 73
12.2. Comparison of the simulation results for one fluid inlet (pressure drop Δp, average velocity $\bar{v}$ at an altitude range of 5 m to 7 m, inlet standard volume flow $\dot{V}_{in}^n$ and solid outlet mean temperature $\bar{T}_{s,out}$). 75
12.3. Mean particle outlet temperatures of PSD-B. 79

C.1. Polynomial coefficients for thermal conductivity (λ_s) and thermal capacity (c_s) of the sinter material, and dynamic viscosity (μ_f), thermal conductivity (λ_f) and thermal capacity ($c_{p,f}$) for dry air. 90

Die approbierte gedruckte Originalversion dieser Diplomarbeit ist an der TU Wien Bibliothek verfügbar
The approved original version of this thesis is available in print at TU Wien Bibliothek.

1. Introduction

The main purpose of burden preparation in iron and steel making is the utilization of fine ore. The agglomeration of fine-grained material is used to allow proper gas flow through the furnace and prevent problems like fluidization. Sintering or pelletizing improves the performance of the blast furnace process and reduces the demand of coke [1].

1.1. Sinter Cooling Plants

The worldwide sinter capacity is approximately 830 million tons per year, of which about 130 million tons are attributable to the European Union [2]. Around 50 % of the energy consumption in sintering processes is carried away by the flue-gas and the cooling air [3]. This indicates the necessity for highly efficient sinter cooling facilities.

In a sinter plant, the material is commonly discharged within a temperature range of 400 °C to 800 °C. For further processing such as transportation, the sinter has to be cooled down to less than 100 °C.
Nowadays, cross-flow sinter coolers are state of the art, i. e. the cooling medium (air) flows perpendicular to the moving direction of the sinter bed. A problem that arises is the varying effective cooling time along the bed height. Furthermore, the specific cooling air demand is very high [4].

On the contrary, counter-flow coolers are capable to guarantee the same effective cooling time for the entire sinter. In a counter-flow facility, the temperature of the cooling air is maximized, which allows more efficient waste heat recovery than in conventional cross-flow coolers. Additionally, a lower amount of specific cooling air is needed. The hot air can be used for downstream processes, e. g. generation of steam or electricity and preheating or drying of materials.
Challenges that arise from the operation counter-flow sinter coolers are to ensure homogeneous flow of the solid material, i. e. formation of a core flow has to be avoided. Segregation effects inside the cooler can lead to inhomogeneous air flow through the packed bed and consequently to non-uniform cooling down of the sinter. Moreover, the discharging method should prevent varying residence time of the sintered material in the cooler [4].

To cope with these non-trivial phenomena, computer simulations using the Discrete Element Method are appropriate to improve and expedite the engineering process of counter-flow sinter cooling plants.

Die approbierte gedruckte Originalversion dieser Diplomarbeit ist an der TU Wien Bibliothek verfügbar
The approved original version of this thesis is available in print at TU Wien Bibliothek.

2. Granular Materials

In [5], a granular material is defined as follows: "*A granular material is a collection of solid particles or grains, such that most of the particles are in contact with at least some of their neighboring particles. The terms 'granular materials', 'bulk solids', 'particulate solids', and 'powders' are often used interchangeably in the literature. Common examples of granular materials are sand, gravel, food grains, seeds, sugar, coal, and cement.*"

Granular materials occur in a broad range of industrial applications, e. g. in the processing of cement, coal or ore, in food, chemical, metallurgical or pharmaceutical industry, powder coating, etc. In those areas bulk solids need to be transported, stored or handled in another way. Phenomena and problems such as arching, clogging, discontinuous flow, undesired separation or segregation can occur during the discharging of silos, containers and feeding hoppers. Therefore, a good understanding of the properties and behavior of granular flows is very important to avoid problems during the operation of facilities [5], [6]. A readable overview of the phenomenology of granular materials is given in [7].
At present the mechanics of granular materials are not well understood compared to other materials. There is no comprehensive theory which is able to reliably predict the behavior in industrial applications. Hence, the constitutive laws on bulk solids still need to be improved. Numerical simulations are suitable to help with this issue. They can also be used to complement or replace expensive and time consuming experiments to some extent. Another field of application is the use as an optimization tool [8].
The flow of granular materials is usually referred to as granular or particulate flow. The granular material is surrounded by an interstitial fluid in many industrial applications. Due to the presence of two or more phases, such multiphase problems are challenging to model and simulate. If the influence of the ambient fluid on the solid flow is insignificant, the fluid is often neglected in the modeling process, e. g. transportation of iron ore on a conveyor belt. In such a case the flow is addressed as dry granular flow.

2.1. Modeling of Granular Materials

There are two modeling approaches with regard to bulk solids, namely the continuum and the discrete or discontinuous approach. If the granular material is replaced by an artificial continuous medium, the forces on single particles are not resolved. Rather volume cells are considered, which are chosen sufficiently big in comparison to the particle size. Stresses and strains similar to fluid or solid continuum mechanics and their effect on the solid flow are investigated in an Eulerian frame of reference.
In the discrete modeling approach, the contacts between the individual particles are resolved and the motion of particles along trajectories is computed in a Lagrangian frame of reference.

Die approbierte gedruckte Originalversion dieser Diplomarbeit ist an der TU Wien Bibliothek verfügbar
The approved original version of this thesis is available in print at TU Wien Bibliothek.

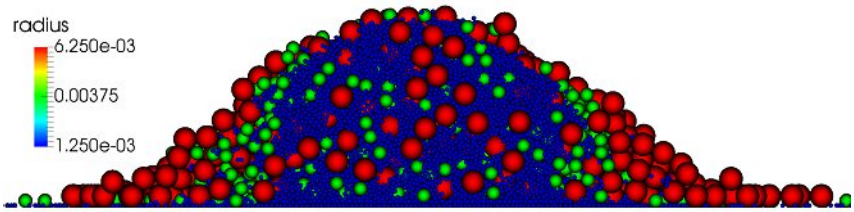

Figure 2.1.: Segregation of particles on an established pile due to different particle size.

Therefore, local phenomena such as segregation and even complex particle shapes can be investigated. Generally, technical systems consist of a huge number of particles, which makes a discontinuous examination of industrial applications computationally very expensive. In recent years this relatively new discipline became more feasible due to the increase of computational power [6].

2.1.1. Segregation

Segregation is the tendency of particles to separate due to different properties like size, density, shape or frictional properties. Problems can occur due to segregation effects in terms of product quality, which in many industrial processes depends on the homogeneity of a blend. The primary mechanisms causing segregation in granular flows are summarized in [9]:

- **Percolation**: smaller particles fall into the void of larger particles in the direction of gravitational acceleration (*'Brazil nut effect'* [10]).
- **Angle of repose**: frictional surface forces tend to stabilize particle piles, while volume forces, such as gravity, have a destabilizing effect. Due to a higher surface-to-volume ratio (specific surface area), smaller particles form heaps with a higher angle of repose than larger particles. Therefore, material with a lower angle of repose (larger particles) flows over material with a higher angle of repose (smaller particles) on already established heaps, see Figure 2.1.
- **Trajectory**: the velocity of small particles is reduced more efficiently than of larger particles due to frictional effects because of a higher surface-to-volume ratio, e. g. granular materials moving down a chute.
- **Fluid drag forces**: smaller particles are fluidized or entrained more easily than larger particles.

According to [11], segregation commonly takes place during filling or discharging processes, inside the solid bed as a result of granular flow moving through facilities (e. g. silos, bins) or due to fluid-solid interaction.

Die approbierte gedruckte Originalversion dieser Diplomarbeit ist an der TU Wien Bibliothek verfügbar
The approved original version of this thesis is available in print at TU Wien Bibliothek.

2.2. Numerical Simulations of Granular Materials

A comprehensive overview of numerical simulation methods for granular materials including commonly used algorithms and further references can be found in [8]. Here, a short overview of the most common methods is given.

2.2.1. Force-Based Molecular Dynamics (MD)

At the beginning, Molecular Dynamics (MD) was mainly used for the simulation of molecular gases and simple liquids. Later the algorithm was adapted for the computation of granular flows. Thus, the force-based molecular dynamics is also known as soft-particle discrete element method (DEM), distinct element method or discrete element modeling. The main difference between MD and DEM is the consideration of forces of different length scales [12]. The dynamics of a granular material is governed by the Newton-Euler equations. A system of coupled nonlinear differential equations has to be solved simultaneously for all particles to compute the trajectories within a given system [8]. Since a constant time-step is used for the integration of the equations of motion, the method is also known as time-driven DEM. The forces acting on particles are a function of position, orientation, velocity and angular velocity and are determined by contact laws and material properties. Moreover, the prevailing forces can be divided into short-range forces (e. g. mechanical contact) and long-range forces (e. g. electrostatic forces). This method is used for ubiquitous applications and spherical or non-spherical particle shapes can be taken into account.
In this work, the force-based molecular dynamics is the method of choice. The method is furthermore only regarded as Discrete Element Method (DEM) and no long-range forces are taken into account.

2.2.2. Event-Driven Molecular Dynamics

In event-driven molecular dynamics, a system of particles is determined by pairwise collisions of infinitesimal or vanishing duration [8]. It is assumed that only one collision at a time occurs in the whole system of particles [13]. Between such collisions, the particles move along ballistic trajectories without interaction. This method is preferably used for dilute granular flows. Often a variable time-step size is applied, which is maximized until the next particle collision. The application of event-driven molecular dynamics is not always justified, e. g. for systems with long-lasting, multiple particle contacts, e. g. in static packings like a sand pile.
Event-driven molecular dynamics is also known as hard-particle DEM and the computational effort is in general smaller than in soft-particle DEM.

Die approbierte gedruckte Originalversion dieser Diplomarbeit ist an der TU Wien Bibliothek verfügbar
The approved original version of this thesis is available in print at TU Wien Bibliothek.

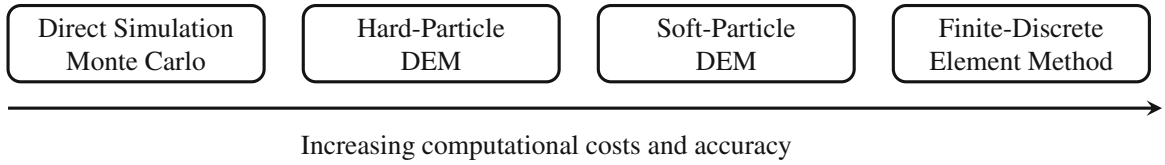

Figure 2.2.: Comparison of numerical simulation methods in terms of computational costs and accuracy [8], [14].

2.2.3. Direct Simulation Monte Carlo (DSMC)

The Direct Simulation Monte Carlo method does not compute particle trajectories, but solves the Boltzmann equation describing the time-dependent flow probability rather than solving the Newton-Euler equations for real particles [7], [8]. In other words, Direct Simulation Monte Carlo is a statistical method considering quasi-particles. It is even more efficient than event-driven molecular dynamics and is preferably used for dilute granular or molecular gases.

2.2.4. Combined Finite-Discrete Element Method

The Combined Finite-Discrete Element Method merges the Discrete Element Method (DEM) and the Finite Element Method (FEM). It is a combination of the dynamic analysis of a large number of deformable particles in a mechanical system. It is used if the deformation of particles is not negligible or for problems in solid mechanics such as failure, fracture, etc. The Combined Finite-Discrete Element Method can be applied in a broad field of engineering areas, e. g. powder technology, composite materials, rock blasting or mining [14].

2.2.5. Other Simulation Methods

Further details regarding other simulation methods for granular flows, such as rigid-body dynamics, cellular automata, the bottom-to-top reconstruction or Brownian dynamics can be found in [8].

Die approbierte gedruckte Originalversion dieser Diplomarbeit ist an der TU Wien Bibliothek verfügbar
The approved original version of this thesis is available in print at TU Wien Bibliothek.

3. Discrete Element Method (DEM)

The Discrete Element Method, as it is commonly used for computer simulations nowadays, was originally developed by Cundall and Strack [15]. It has recently gained in importance, which is shown by the rising number of related publications [12]. The basic concept of DEM is described in 2.2.1. In this chapter the fundamentals such as governing equations, contact laws and rolling-friction models for spherical particles are discussed. Furthermore an overview on time-integration schemes, conductive heat transfer between spherical particles and long-range forces is given.

3.1. Equations of Motion

The dynamics of the granular material is governed by the Newton-Euler equations

$$m_i \frac{\partial^2 \vec{r}_i}{\partial t^2} = \sum_j \vec{F_{ij}}^{\,c} + \vec{F_i}^{\,f} + \vec{F_i}^{\,g} + \sum_k \vec{F_{ik}}^{\,nc} , \tag{3.1}$$

$$I_i \frac{\partial^2 \vec{\varphi}_i}{\partial t^2} = \sum_j \vec{M}_{ij} . \tag{3.2}$$

These equations describe the translational and rotational motion of each individual particle i with the mass m_i and the moment of inertial I_i. The sum of contact forces $\sum \vec{F_{ij}}^{\,c}$ and the sum of torques $\sum \vec{M}_{ij}$ act on the particle i by particle j or walls and are determined by contact laws and material properties. They are functions of particle position $\vec{r}$, orientation $\vec{\varphi}$, velocity $\vec{v}$ and angular velocity $\vec{\omega}$. The torque $\vec{M}_{ij}$ can be split into a component resulting from tangential forces and a component resulting from other sources like rolling-friction, see 3.4. The fluid-particle interaction force $\vec{F_i}^{\,f}$ and the gravitational force $\vec{F_i}^{\,g}$ are non-contact forces. The influence of an ambient fluid on a granular flow is discussed in 6.4. Other non-contact forces on particle i by particle k, such as Van-der-Walls or capillary forces, are taken into account by $\sum \vec{F_{ik}}^{\,nc}$, see 3.6. The forces acting on a particle are illustrated in Figure 3.1.

3.2. Time-Integration Schemes

A brief introduction into the fundamentals of numerical analysis such as relative and absolute error, truncation error or stability of numerical schemes is given in [7]. Furthermore, commonly used explicit and implicit time-integration algorithms for DEM simulations are discussed. The important distinction between symplectic and non-symplectic integrators is emphasized. Symplectic integrators are preferably used for the solution of the Hamilton's equations. They conserve

Die approbierte gedruckte Originalversion dieser Diplomarbeit ist an der TU Wien Bibliothek verfügbar
The approved original version of this thesis is available in print at TU Wien Bibliothek.

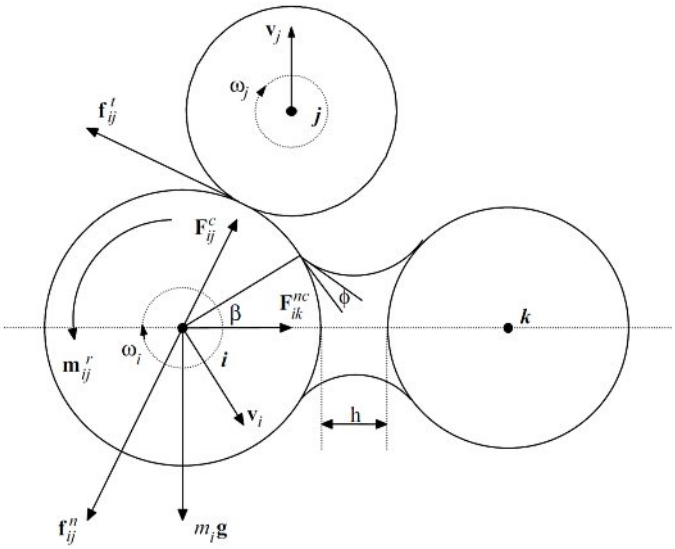

Figure 3.1.: Schematic illustration of the forces acting on particle i from contacting particle j and non-contacting particle k (capillary force here), from [12].

energy better than non-symplectic integrators and are therefore more suitable for the integration of the equations of motion in DEM. Schemes such as implicit or explicit Euler and Runge-Kutta fall into the category of non-symplectic integrators, while Verlet [16], Velocity-Verlet or Gear's integration scheme [8] belong to the group of symplectic integrators.

3.2.1. Velocity-Verlet Scheme

In granular flows, the particle velocities at every time-step are of particular interest. Some time-integration methods, e. g. the classical Verlet scheme [16], do not track the velocities explicitly. On the contrary, the Velocity-Verlet scheme computes the velocities in sub-steps. Since the algorithm is a one-step method, it is self-starting. Only the position, velocity and acceleration values from the previous time-step are needed for the next calculation step, i. e. less memory is necessary compared to multi-step algorithms [7].

Sketch of the Algorithm

First, the velocity $\vec{v}$ at the sub-step $t + \frac{\Delta t}{2}$ is calculated according to

$$\vec{v}(t + \frac{\Delta t}{2}) = \vec{v}(t) + \vec{a}(t)\frac{\Delta t}{2}\,. \tag{3.3}$$

Then, the particle position $\vec{r}$ at the time $t + \Delta t$ is computed as follows

Die approbierte gedruckte Originalversion dieser Diplomarbeit ist an der TU Wien Bibliothek verfügbar
The approved original version of this thesis is available in print at TU Wien Bibliothek.

$$\vec{r}(t+\Delta t) = \vec{r}(t) + \vec{v}(t+\frac{\Delta t}{2})\,\Delta t\,. \tag{3.4}$$

The acceleration $\vec{a}$ at the time $t+\Delta t$ is evaluated from short-range and long-range particle interaction as discussed in 3.3, 3.4 and 3.6. In a final step, the velocity at the time $t+\Delta t$ is equal to

$$\vec{v}(t+\Delta t) = \vec{v}(t+\frac{\Delta t}{2}) + \vec{a}(t+\Delta t)\frac{\Delta t}{2}\,. \tag{3.5}$$

3.2.2. Time-Step Estimation

Granular materials are rather stiff because of the high Young's modulus. Therefore, it is of utmost importance to choose the time-step sufficiently small to capture the basic phenomena of energy transmission in the particle assembly.

On the one hand, the elastic wave propagation through particles in dynamic granular flows has to be captured. According to [17], Rayleigh waves are the most important transport mechanism in this context. The critical time-step has to be chosen as a fraction of the time needed by a wave to propagate through a particle. This value, sometimes called Rayleigh-time, can be estimated by the following equation

$$t_R = \frac{\pi\, R}{0.8766 + 0.163\,\nu_{Po}}\sqrt{\frac{\rho}{G}}\,, \tag{3.6}$$

with the particle radius R, the Poisson's ratio ν_{Po}, the particle density ρ and the shear modulus G.

On the other hand, the particle contact has to be resolved over several time-steps for stable and reproducible DEM simulations. In accordance with Hertzian theory, wave motion can be neglected for perfectly elastic and frictionless contact of spheres over a circular contact area. According to [18], the impact time, also called Hertz time, is estimated by

$$t_H = 2.87\left(\frac{m^{*2}}{R^*\,Y^*\,v_{max}}\right)^{1/5}\,, \tag{3.7}$$

where m^* is the effective mass, R^* the effective radius, Y^* the effective Young's modulus and v_{max} the maximum particle velocity. The effective values are calculated according to (3.18) to (3.20).

Die approbierte gedruckte Originalversion dieser Diplomarbeit ist an der TU Wien Bibliothek verfügbar
The approved original version of this thesis is available in print at TU Wien Bibliothek.

As a rule of thumb, the selected time-step size should be around 10 % to 30 % of the Rayleigh-time or 5 % to 15 % of the Hertz-time.

3.3. Contact Model for Spherical Particles

In reality, particles do not contact in a single point but rather in a finite area due to deformation. The soft-particle DEM approach does not consider the deformation of particles, but they are permitted to overlap slightly. The quantity ξ_{ij} is called spatial overlap, normal overlap or mutual compression and is greater or equal than zero if two spherical particles are in mechanical contact. Two particles are in contact, if the distance of their centers of mass is smaller than the sum of their radii

$$\xi_{ij}{}^{n} = R_i + R_j - |\vec{r_i} - \vec{r_j}| > 0\,. \tag{3.8}$$

3.3.1. Normal and Tangential Forces

The contact force is decomposed into a normal and a tangential component and it is equal to zero if two particles are not in contact.

$$\vec{F_{ij}}^{\,c} = \begin{cases} \vec{F_{ij}}^{\,n} + \vec{F_{ij}}^{\,t} & \text{if } \xi_{ij}{}^{n} > 0\,, \\ 0 & \text{otherwise.} \end{cases} \tag{3.9}$$

In a two-dimensional case, the normal and tangential component of the contact force can be written as

$$\vec{F_{ij}}^{\,n} = F_{ij}{}^{n}\,\vec{e_{ij}}^{\,n}\,, \qquad \vec{F_{ij}}^{\,t} = F_{ij}{}^{t}\,\vec{e_{ij}}^{\,t}\,, \tag{3.10}$$

with the normal and tangential unit vector

$$\vec{e_{ij}}^{\,n} = \frac{\vec{r_i} - \vec{r_j}}{|\vec{r_i} - \vec{r_j}|}\,, \qquad \vec{e_{ij}}^{\,t} = \begin{pmatrix} 0 & -1 \\ 1 & 0 \end{pmatrix} \cdot \vec{e_{ij}}^{\,n}\,. \tag{3.11}$$

The normal and tangential force is calculated using a linear spring-dashpot model. Hence, both parts contain a linear elastic and a viscous damping term, see Figure 3.2. For better legibility, the indices ij are dropped in the following. The normal force component can be written as

Die approbierte gedruckte Originalversion dieser Diplomarbeit ist an der TU Wien Bibliothek verfügbar
The approved original version of this thesis is available in print at TU Wien Bibliothek.

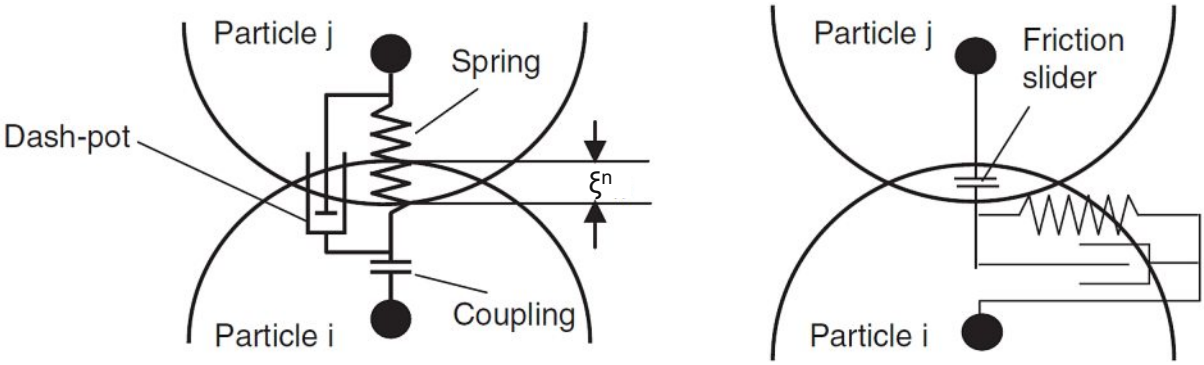

Figure 3.2.: Spring-dashpot model for normal (left) and tangential (right) contact forces, from [13].

$$F^n = k^n \xi^n + \gamma^n v^n \,, \tag{3.12}$$

with the normal elastic constant k_n, the normal damping constant γ_n and the relative normal velocity

$$v^n = \frac{d\xi^n}{dt} = \dot{\xi}^n \,. \tag{3.13}$$

Since the normal overlap $\xi^n > 0$, the elastic part of the normal force is purely repulsive. The formulation of the linear spring-dashpot model leads to an artifact, which can cause attractive particle forces. This phenomenon is sometimes called *'artificial force effect'*. The attractive damping force may become bigger than the repulsive elastic spring force leading to an overall non-repulsive normal force component, see Figure 3.3. This artifact can cause non-realistic collision forces and therefore has to be eliminated in the simulation code.

The tangential force component results to

$$F^t = k^t \xi^t + \gamma^t v^t \,. \tag{3.14}$$

A commonly used formulation for the tangential overlap is

$$\xi^t = \int_{t_0}^{t} v^t(\tau)\, d\tau \,. \tag{3.15}$$

This integral represents the elastic tangential deformation of the particle surfaces that occurred since the time when the particles initially touched ($t = t_0$). The restoring tangential force can be determined by the elongation of the tangential spring that stores the energy from tangential

Die approbierte gedruckte Originalversion dieser Diplomarbeit ist an der TU Wien Bibliothek verfügbar
The approved original version of this thesis is available in print at TU Wien Bibliothek.

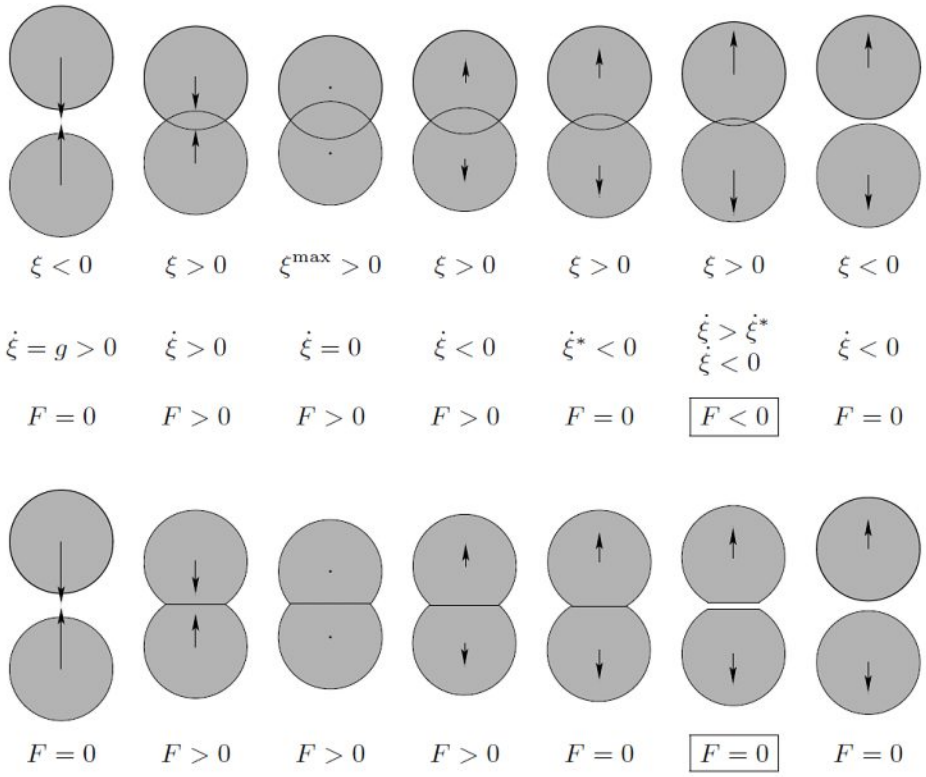

Figure 3.3.: Breakdown of a particle collision into different stages. Attractive forces due to the artificial force effect are highlighted in boxed notation, from [8].

motion. The consideration of ξ^t is also called *'shear history effect'*. The relative tangential velocity between particle i and j can be expressed as

$$v^t = (\vec{v_j} - \vec{v_i}) \cdot \vec{e_{ij}}^t + R_i\omega_i + R_j\omega_j \,. \tag{3.16}$$

Furthermore the tangential force is limited by Coulomb's friction law

$$\left|F^t\right| \leq \mu_s \left|F^n\right| \,, \tag{3.17}$$

with the sliding-friction parameter μ_s. When the particles begin to slide, the tangential overlap term ξ^t has to be re-scaled to account for slippage.

The simple tangential force model by Cundall and Strack [15] described here is a trade-off between good agreement with experimental results and computational efficiency. There are more comprehensive models, which are computationally more expensive and therefore not feasible for large-scale simulations, e. g. the model proposed by Walton and Braun [19].

Die approbierte gedruckte Originalversion dieser Diplomarbeit ist an der TU Wien Bibliothek verfügbar
The approved original version of this thesis is available in print at TU Wien Bibliothek.

3.3.2. Hertz-Mindlin Contact Model

A detailed discussion on contact force models can be found in [20]. The following formulations describe the generalized contact law between two viscoelastic particles according to [21] based on the Hertzian contact theory for elastic spheres. The effective, or sometimes called equivalent, quantities radius R^*, mass m^*, Young's modulus Y^* and shear modulus G^* of two colliding particles i and j can be written as

$$\frac{1}{R^*} = \frac{1}{R_i} + \frac{1}{R_j}\,, \tag{3.18}$$

$$\frac{1}{m^*} = \frac{1}{m_i} + \frac{1}{m_j}\,, \tag{3.19}$$

$$\frac{1}{Y^*} = \frac{(1-\nu_i^2)}{Y_i} + \frac{(1-\nu_j^2)}{Y_j}\,, \tag{3.20}$$

$$\frac{1}{G^*} = \frac{2(2-\nu_i)(1+\nu_i)}{Y_i} + \frac{2(2-\nu_j)(1+\nu_j)}{Y_j}\,, \tag{3.21}$$

with the Poisson's ratio ν. The normal and tangential stiffness and damping coefficients k_n, γ_n, k_t and γ_t for viscoelastic particle contact are chosen as follows

$$k_n = \frac{4}{3} Y^* \sqrt{R^* \xi_n}\,, \tag{3.22}$$

$$\gamma_n = -2\sqrt{\frac{5}{6}}\beta\sqrt{S_n m^*}\,, \tag{3.23}$$

$$k_t = 8 G^* \sqrt{R^* \xi_n}\,, \tag{3.24}$$

$$\gamma_t = -2\sqrt{\frac{5}{6}}\beta\sqrt{S_t m^*}\,, \tag{3.25}$$

with the normal and tangential shear stiffness S_n and S_t and the damping factor β

$$S_n = 2 Y^* \sqrt{R^* \xi_n}\,, \tag{3.26}$$

Die approbierte gedruckte Originalversion dieser Diplomarbeit ist an der TU Wien Bibliothek verfügbar
The approved original version of this thesis is available in print at TU Wien Bibliothek.

$$S_t = 8G^* \sqrt{R^* \xi_n}\,, \tag{3.27}$$

$$\beta = \frac{\ln(e)}{\sqrt{\ln^2(e) + \pi^2}}\,, \tag{3.28}$$

where e represents the coefficient of restitution.

3.4. Rolling-Friction Model

The terms rolling-friction and rolling-resistance are often used interchangeably in the literature. Rolling-friction is used to model two different phenomena in particulate systems. On the one hand, the resistance to a rolling motion can be depicted. On the other hand, a torque applied to spherical particles is used to account for the effect of non-spherical particle shapes, see 3.8. Different rolling-friction models are available in the Discrete Element Method. A review of commonly used rolling-friction models can be found in [22]. In [23] a more generalized model is proposed and several test cases for two-dimensional disks are investigated.

3.4.1. Constant Directional Torque (CDT)

A constant torque is applied against the relative rotational motion of two particles in contact. A shortcoming of this model is the step-wise oscillation of the constant torque once a stationary position is accomplished [23]. Therefore it is not suitable for the simulation of pseudo-static systems such as sand piles. However, the CDT-model is computationally cheap and commonly used in dynamic particulate flows to account for energy dissipation due to rolling-friction between particles.

3.4.2. Elastic-Plastic Spring-Dashpot (EPSD)

Similar to the formulation of normal and tangential contact forces, the torque of the elastic-plastic spring-dashpot model consists of an elastic spring torque and a viscous damping torque. Sometimes the epsd-model is applied without the damping term. In this case the behavior is similar to the cdt-model, except that the oscillating frequency depends on material properties instead of the time-step. If the viscous damping term is included, the epsd-model was found to be *"superior in its ability to form a static pile without any significant residual kinetic energy and its insensitivity to the computational time step"* [23]. Furthermore, it gives good results for both

Die approbierte gedruckte Originalversion dieser Diplomarbeit ist an der TU Wien Bibliothek verfügbar
The approved original version of this thesis is available in print at TU Wien Bibliothek.

dynamic and pseudo-static granular flow regimes and is therefore the rolling-friction model of choice in this work.

3.4.3. EPSD Formulation

The total rolling-friction torque M_r according to [23] is composed of an elastic spring torque M_r^k and a viscous damping torque M_r^d

$$M_r = M_r^k + M_r^d \,. \tag{3.29}$$

The rolling stiffness k_r is related to the normal contact stiffness k_n, the rolling-friction coefficient μ_r and the equivalent radius R^* as follows

$$k_r = 2.25\, k_n\, \mu_r^2\, (R^*)^2 \,. \tag{3.30}$$

The spring torque at the time $t + \Delta t$ reads

$$M_{r,t+\Delta t}^k = M_{r,t}^k + \Delta M_r^k \,, \tag{3.31}$$

where ΔM_r^k is the incremental spring torque due to the incremental relative rotation $\Delta\theta_r$ between two particles

$$\Delta M_r^k = -k_r\, \Delta\theta_r \,. \tag{3.32}$$

The spring torque is truncated to fulfill the condition

$$M_{r,t+\Delta t}^k \leq \Delta M_r^m \,, \tag{3.33}$$

where M_r^m is the limiting torque at the full mobilization rolling angle determined by the coefficient of rolling-friction μ_r, the equivalent radius R^* and the normal force component F_n

$$\Delta M_r^m = \mu_r\, R^*\, F_n \,. \tag{3.34}$$

The viscous damping torque M_r^d is defined as a function of the relative rolling angular velocity $\dot{\theta}_r$ and the rolling viscous damping coefficient C_r

Die approbierte gedruckte Originalversion dieser Diplomarbeit ist an der TU Wien Bibliothek verfügbar
The approved original version of this thesis is available in print at TU Wien Bibliothek.

$$M^d_{r,t+\Delta t} = \begin{cases} -C_r\,\dot{\theta}_r & \text{if } \left|M^k_{r,t+\Delta t}\right| < M^m_r\,, \\ 0 & \text{if } \left|M^k_{r,t+\Delta t}\right| = M^m_r\,. \end{cases} \tag{3.35}$$

The rolling viscous damping coefficient C_r can be expressed as

$$C_r = \eta_r\, C_r^{crit}\,, \qquad C_r^{crit} = 2\,\sqrt{I_r\,k_r}\,, \tag{3.36}$$

where η_r is the rolling viscous damping ratio and I_r is the equivalent moment of inertia of two particles i and j, according to

$$I_r = \left(\frac{1}{I_i + m_i R_i^2} + \frac{1}{I_j + m_j R_j^2}\right)^{-1}\,. \tag{3.37}$$

3.5. Conductive Heat Transfer

Heat transfer in granular flows takes place by the following mechanisms [24]:

- Thermal conduction within solids.
- Thermal conduction between two contacting particles.
- Thermal radiation between particle surfaces.
- Thermal conduction within the fluid.
- Thermal convection between particles and an interstitial fluid.

According to [21], uniform particle temperature is assumed and thus the thermal conduction within the solid material is neglected. This is a necessary simplification to ensure reasonable computation time. Radiation between particles is not taken into account in this work. The energy balance for a particle i can be written as

$$m_i\,c_{p,i}\,\frac{dT_i}{dt} = \sum_j \dot{Q}_{ij} + \dot{Q}_{source}\,, \tag{3.38}$$

where $c_{p,i}$ is the specific heat capacity, $\dot{Q}_{ij}$ is the convective heat flux between particle i and j and $\dot{Q}_{source}$ is the heat flux due to other sources, e. g. chemical reactions or convective heat transfer between a particle and an ambient fluid, see 6.4.3. The heat flux between two contacting particles is calculated as follows

Die approbierte gedruckte Originalversion dieser Diplomarbeit ist an der TU Wien Bibliothek verfügbar
The approved original version of this thesis is available in print at TU Wien Bibliothek.

$$\dot{Q}_{ij} = h_{ij} \ (T_i - T_j) \ , \tag{3.39}$$

with inter-particle conductance h_{ij} stemming from two individual thermal conductivities λ_i and λ_j and the contact area A_{ij}^c

$$h_{ij} = \frac{4\,\lambda_i \lambda_j}{\lambda_i + \lambda_j} \sqrt{A_{ij}^c} \, . \tag{3.40}$$

The contact area of two particles is calculated from their overlap. In case that the Young's Modulus is reduced to speed up DEM simulations (see 4.2.2), the contact area is over-predicted and has to be corrected.

3.6. Non-Contact Forces

An introduction to non-contact forces other than gravitational forces or fluid-particle interaction can be found in [5]. Examples for such forces are:

- Electrostatic (Coulomb) forces,
- Van der Waals forces,
- Liguid bridges (capillary forces) between particles.

Commonly used model formulations in the Discrete Element Method are listed in [12], [13]. The above mentioned non-contact forces are negligible for the prevailing problem of this work and are therefore not further investigated.

3.7. Neighbor List Algorithm

In DEM codes, a combination of the Verlet list algorithm and the cell linked algorithm is often used to improve the efficiency of particle collision detection. This is achieved through reduction of the possible interaction partners [25]. In the following, only the fundamentals of both algorithms are discussed. Further details can be found in [8], [26] and [27].

Die approbierte gedruckte Originalversion dieser Diplomarbeit ist an der TU Wien Bibliothek verfügbar
The approved original version of this thesis is available in print at TU Wien Bibliothek.

3.7.1. Verlet Lists

In the Verlet algorithm, a list of close neighbors for every particle is constructed. Close means that the distance between two particles $|\vec{r_i} - \vec{r_i}|$ is smaller than the sum of their radius R_i and R_j plus a certain length c, called *'Verlet parameter'* or *'skin parameter'*

$$|\vec{r_i} - \vec{r_i}| - R_i - R_j < c\,. \tag{3.41}$$

The idea of Verlet lists is, that the neighborhood of a particle changes only slowly, i. e. particles that are close at a given time-step will stay close to each other at least the following few time-steps. Afterwards the neighbor list is rebuilt. The list of potential particle contacts is checked for interaction pairs every time-step. The Verlet algorithm provides efficient force evaluation due to few possible contact partners, but the major drawback is the inefficient construction of the neighbor list.

3.7.2. Cell Linked Algorithm

In the cell linked algorithm, the computational domain is decomposed into a spatial grid with equally sized cells. Particles are assigned to a certain cell due to their position. Sometimes this procedure is also called *'binning'*. Under the assumption that cells are bigger than the particle diameter, neighbors and therefore potential collision partners can only be found in the cell of the particle itself and the neighboring cells. The cell linked algorithm features fast and efficient construction of neighbor lists, but a high number of particles have to be checked for force evaluation.

3.7.3. Combined Approach

The algorithm proposed in [26] combines the advantages of both Verlet list algorithm and cell linked algorithm. The neighbor list construction results from the following approach:

- Decomposition of the computational domain into several cells (bins).
- Assignment of particles to the cells according to the position.
- Construction of neighbor list by searching only neighboring cells.

Die approbierte gedruckte Originalversion dieser Diplomarbeit ist an der TU Wien Bibliothek verfügbar
The approved original version of this thesis is available in print at TU Wien Bibliothek.

3.8. Non-spherical particle shape

Instead of accounting for non-spherical particle shapes by a rolling-friction model (non-resolved approach), particles can be lumped together to consider complex shaped surfaces (multi-sphere method), see Figure 3.4 (a). Another possibility is the implementation of superquadric particles in the DEM code to resolve non-spherical shapes, see Figure 3.4 (b). An introduction to sharp-edged or polygonal particles is given in [7], [8].

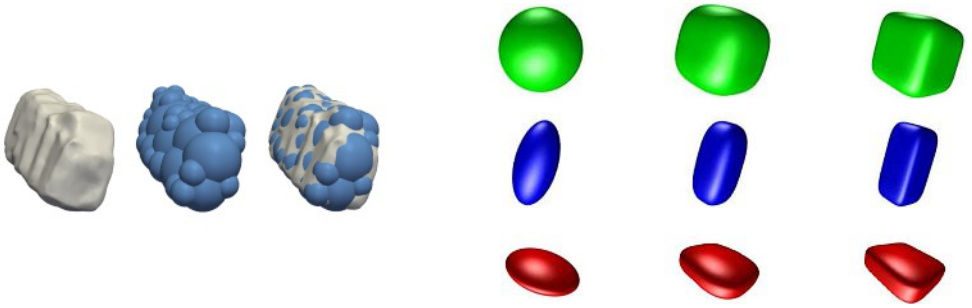

(a) Multi-sphere method, from [11]

(b) Superquadric partiles, from [28]

Figure 3.4.: Methods to resolve non-spherical particle shapes.

Die approbierte gedruckte Originalversion dieser Diplomarbeit ist an der TU Wien Bibliothek verfügbar
The approved original version of this thesis is available in print at TU Wien Bibliothek.

4. Speed-Up of DEM Simulations

Numerous ways to speed up numerical simulations of granular flows exist. An overview on frequently used methods for DEM simulations is given below. An increase of computational performance can be achieved on the basis of algorithms or due to sophisticated modeling approaches. It is of vital importance that the reproduction of realistic physical behavior in the simulation has to be maintained in both cases.

4.1. Algorithms

The Discrete Element Method is basically a mesh-free method since it utilizes a Lagrangian frame of reference [29]. Nevertheless, background grids are used to increase the efficiency of DEM codes.

4.1.1. Neighbor Lists

Neighbor lists are among the most commonly used methods in DEM to speed up simulations. The objective of these algorithms is to reduce the number of possible interaction pairs. To check if a particle is in contact with any other particle within the computational domain, basically a mathematical operation of $\mathcal{O}({N_p}^2)$ has to be performed, in which N_p is the number of particles [26]. To reduce the number of possible collisions, neighbor list algorithms are applied. Since at least simple algorithms are implemented in all recent DEM codes, it can probably be seen as a part of the Discrete Element Method. Neighbor lists are discussed in more detail in 3.7.

4.1.2. Parallelization

The idea of parallelization is to split a mathematical problem into parts which are processed in parallel, i. e. at the same time. Highly sophisticated algorithms were developed for DEM codes [25]. Here, only a short introduction into the basics of a static domain decomposition method and dynamic load balancing is given.

4.1.2.1. Static Domain Decomposition

Static domain decomposition denotes spatial decomposition of the simulation domain into several sub-domains (sub-ares, boxes) with a fixed size. The Newton-Euler equations for particles allocated in a certain box are solved by the corresponding processor [8]. Data of particles located at the boundary of the sub-areas (e. g. particle positions, velocities or forces) need to be

Die approbierte gedruckte Originalversion dieser Diplomarbeit ist an der TU Wien Bibliothek verfügbar
The approved original version of this thesis is available in print at TU Wien Bibliothek.

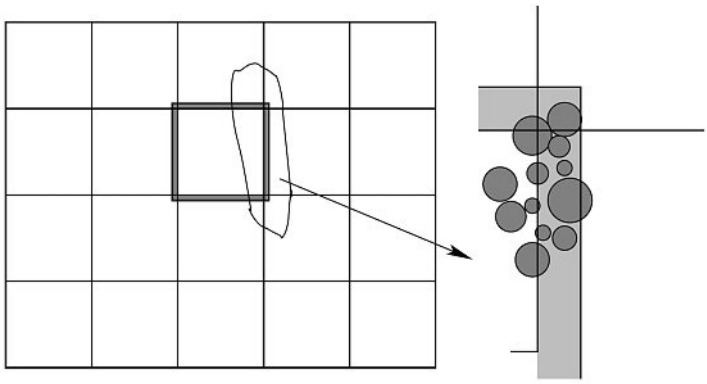

Figure 4.1.: Decomposition of the simulation domain into sub-areas and boundaries for data exchange between processes, from [8].

exchanged between adjacent sub-domains. This ensures that no information is lost and particle interactions are calculated correctly. For this purpose the Message Passing Interface (MPI) can be used. The boundaries of the sub-domains are sometimes called *'ghost region'* and the corresponding particles are referred to as *'ghost particles'* [30]. Particles can also migrate from one sub-area to another. In Figure 4.1 the decomposition of a computational domain is depicted and the boundaries of a sub-domain are highlighted.

4.1.2.2. Dynamic Load Balancing

In DEM simulations, the workload of a processor is approximately proportional to the number of associated particles [30]. Hence, static domain decomposition works basically well for homogeneous problems. But many problems that are simulated with DEM are of inhomogeneous nature [25]. In this case particles are not always distributed evenly among processors which causes performance inefficiencies. Dynamic load balancing algorithms perform spatial decomposition of the simulation domain, so that every processor owns approximately the same number of particles. The impact on the subdivision of the computational domain is shown in Figure 4.2.

4.2. Modeling Approach

The calculation time of DEM simulations can be significantly reduced by introducing simplifications or a lower level of detail in utilized models. Some established approaches are listed below. It has to be indicated, that the scaling techniques come with different prerequisites. If more than one approach is used, it has to be ensured that those prerequisites are not violated.

Die approbierte gedruckte Originalversion dieser Diplomarbeit ist an der TU Wien Bibliothek verfügbar
The approved original version of this thesis is available in print at TU Wien Bibliothek.

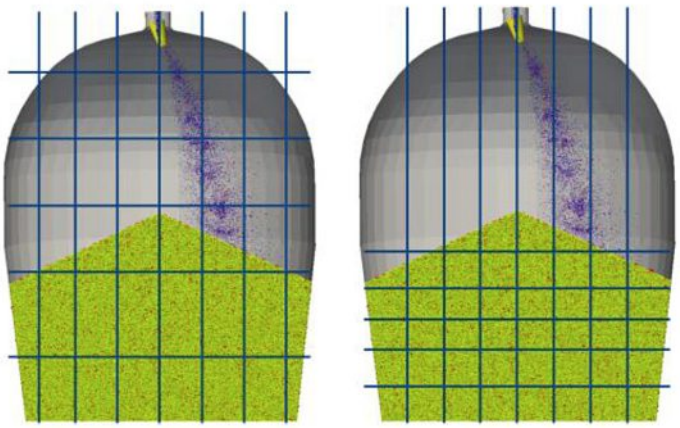

Figure 4.2.: Static domain decomposition (left) compared to domain composition with dynamic load balancing (right), from [11].

4.2.1. Coarse-Graining

An effective and easy-to-use coarse-graining approach based on an appropriate adjustment of particle interaction laws was proposed by Bierwisch [31], [32], [33]. The concept of enlarging particles through scaling of the diameter d_p with the coarse-graining factor c_{cg} yields the reduction of the number of particles in the simulation domain. Thus, a decrease in computational time can be achieved.

It is of utmost importance to know if an adequate scaling of mechanical parameters leads to unchanged macroscopic properties. In other words, the influence on the granular material and its flow pattern has to be insignificant. Dimensional analysis have shown that the coarse-graining scheme is valid for both

- dilute granular flows (based on force scaling), and
- dense granular flows (based on scaling via the stress tensor).

Coarse-graining naturally fails for effects that depend intrinsically on the particle size. The scaling factor is also limited by the characteristic length scale L_c of a simulated system, e. g. a geometrically constricted passage (bottleneck). If the particle diameter is scaled, the condition $L_c \gg c_{cg}\, d_p$ has to be fulfilled.

Coarse-graining of particles can also be interpreted as representing a number of small particles as a larger one. Hence, the terms *"particle parcels"* or *"lumping particles together"* are sometimes used in literature [34], [35]. This must not be confused with the multi-sphere method to model non-spherical particle shapes, see 3.8.

Die approbierte gedruckte Originalversion dieser Diplomarbeit ist an der TU Wien Bibliothek verfügbar
The approved original version of this thesis is available in print at TU Wien Bibliothek.

If coarse-graining is applied in a coupled DEM-CFD simulation, source terms for momentum and energy exchange between the fluid and solid phase are influenced. The fluid flow field is affected by the particle size, therefore correction is needed. A detailed discussion on the effect of coarse-graining on the governing equations is given in 6.5. Simulation test cases investigating the coarse-graining code implementation are performed in 7.1.

4.2.2. Young's Moldulus

It is common practice in DEM simulations to use an artificially decreased Young's modulus. Particles with a lower Young's modulus are softer and thus the collision duration is higher. This effect on the contact time becomes apparent with regard to the Hertz time (3.7), which is inversely proportional to the Young's modulus.

It has been shown that the Young's modulus can be decreased significantly without influence on the simulation results [31], [33]. However, the artificial decrease is limited by the nature of the simulation problem. This can especially be an issue in static problems. In [31] it is reported that the volume fraction can be significantly influenced by an unrealistic low Young's modulus.

In the Discrete Element Method, particles are permitted to overlap to account for surface deformation during collisions, see 3.3. A lower Young's modulus causes artificial increase of the overlap and the contact area. If heat conduction between particles is considered in the simulation, a correction factor has be introduced to account for the artificially increased contact area [21].

4.2.3. Density-Scaling

Density-scaling can be applied to increase the critical time-step in DEM simulations. Since the Rayleigh time (3.6) is proportional to the particle density, the time-step size can be increased if the density is scaled up. In [36], problems in conjunction with scaling of particle density are critically reviewed. Application of a density-scaling approach in quasi-static problems has been reported in [37], [38].

However, this approach has to be used with caution. Especially the application in a coupled DEM-CFD simulation is questionable. For example the fluid-solid energy balance is only influenced on the solid-side in case of density-scaling. This disequilibrium has to be corrected.

Die approbierte gedruckte Originalversion dieser Diplomarbeit ist an der TU Wien Bibliothek verfügbar
The approved original version of this thesis is available in print at TU Wien Bibliothek.

4.2.4. Time-Scaling

For transient simulations with long time-scales, a possible approach to reduce the computational effort is to decrease through-put time or residence time of solids in the simulation. This can be achieved by increasing solid velocities or massflows. The procedure is justified, if the influence on the simulation outcome is negligible, e. g. if the fluid velocity u_f in a counter flow cooler is much bigger than the solid velocity u_s and the condition $u_f \gg u_s$ is still fulfilled after time-scaling is applied.

A time-scaling method is employed in this work. The governing equations of the simulated system are analyzed in 6.4 and a correction factor is introduced in 6.6.

A similar approach to reduce computation time is reported in [11]. The authors use the term *'temporal speed-up'* instead of time-scaling.

Die approbierte gedruckte Originalversion dieser Diplomarbeit ist an der TU Wien Bibliothek verfügbar
The approved original version of this thesis is available in print at TU Wien Bibliothek.

5. Software

There are plenty of commercial and open-source codes available for both DEM and CFD simulations. In this work, the most important selection criteria was the coupling of DEM and CFD code. There are commercial as well as open-source packages that offer coupling possibilities to a greater or lesser extent.

One big advantage of open-source software is the distribution of the source-code. This allows easy implementation of new simulation models and customization of the code. Therefore, the DEM-CFD framework consisting of the software packages LIGGGHTS, OpenFOAM and CFDEM-coupling is chosen.

5.1. LIGGGHTS and CFDEMcoupling

The LIGGGHTS and CFDEMcoupling software packages are available as public and premium version, but only the public version is free to use. In both cases the public version is used for the simulations. In the following LIGGGHTS-PUBLIC and CFDEMcoupling-PUBLIC are referred to as LIGGGHTS and CFDEMcoupling respectively.

LIGGGHTS stands for *'LAMMPS Improved for General Granular and Granular Heat Transfer Simulations'* [21]. It is an open-source software package for particle simulations using the Discrete Element Method. The code implementation is based on the top of the Molecular Dynamics simulator LAMMPS, which is an acronym for *'Large-scale Atomic/Molecular Massively Parallel Simulator'* [39], [40]. Both code packages are written in C++ and are characterized by an excellent parallel efficiency and scalability [30]. An input script language, which is basically a text file, is used instead of a graphical user interface (GUI).

The main difference between LIGGGHTS and LAMMPS lies i. a. in the handling of complex geometries, granular models for particle contacts or a conductive heat transfer model [25].

CFDEMcoupling is a parallel coupled DEM-CFD framework [41] combining LIGGGHTS and OpenFOAM. OpenFOAM is an open-source Computational Fluid Dynamics toolbox written in C++ [42], [43]. Both LIGGGHTS and OpenFOAM use MPI parallelization, therefore CFDEM-coupling permits fully parallel coupled DEM-CFD simulations.

An insight on topics such as parallel performance, computational efficiency and scalability or dynamic load balancing as well as several validation cases of both LIGGGHTS and CFDEM-coupling is presented in [30], [44], [45].

Die approbierte gedruckte Originalversion dieser Diplomarbeit ist an der TU Wien Bibliothek verfügbar
The approved original version of this thesis is available in print at TU Wien Bibliothek.

5.2. Drawbacks in LIGGGHTS-PUBLIC

Some drawbacks of the LIGGGHTS-PUBLIC version 3.3.1 (released 14.01.2016) encountered during this work are summarized in the following:

- No temperature dependent solid material properties, i. e. for example that the solid thermal heat capacity cannot be considered as a function of temperature.
- No parallel implementation of the multi-sphere method to model non-spherical particles, see Figure 3.4 (a).
- No particle shapes other than spheres, e. g. superquadric particles, see Figure 3.4 (b).
- No dynamic load balancing implementation, which can be problematic for spatially unbalanced simulation problems.
- No axisymmetric boundary conditions, i. e. the computational domain cannot be considered in a wedge-shaped form.

Die approbierte gedruckte Originalversion dieser Diplomarbeit ist an der TU Wien Bibliothek verfügbar
The approved original version of this thesis is available in print at TU Wien Bibliothek.

6. DEM-CFD Coupling

A large number of problems in nature and industry are dealing with multiphase flows. Especially in the fields of energy technology, process or chemical engineering, fluid-solid flows are of interest. Possible areas of application are pneumatic transport, cooling or drying of granular flows, fluid flow through a packed bed or fluidized beds.

Several modeling approaches and simulation methods for fluid-solid problems exist [29], [46]. This work concentrates on the DEM-CFD method. The Discrete Element Method is used to model the granular flow in a Lagragian frame of reference, whereas Computational Fluid Dynamics is used to resolve the fluid flow in an Eulerian frame of reference. Pioneering work on this field was carried out by Tsuji et al. [47], [48]. A review on prevailing models for particle-fluid interaction is given in [12], [49].

An introduction into granular materials and the Discrete Element Method is given in 2 and 3 respectively.

6.1. Computation Fluid Dynamics (CFD)

Analytical solutions for fluid mechanics problems exist only for a limited number of flows. This is due to the fact that the governing equations, also known as Navier-Stokes equations, form a set of partial differential equations.

One way to solve fluid flows is the Computational Fluid Dynamics (CFD) method, which can be considered as combination of fluid mechanics and numerical analysis. The geometry of a problem is discritized into a spatial grid and the resulting system of equations composed of all grid cells is solved using a computer. This is only an oversimplified description of Computational Fluid Dynamics, but a detailed discussion is far beyond the scope of this work. The interested reader is referred to [50], which gives an excellent introduction and summary on the topic.

6.2. Coupling Approach

Two coupling approaches for the DEM-CFD method are discussed in the following. The difference lies in the resolution of particle shape and inter-particle flow and the thereby associated computational effort. For a more detailed explanation, the interested reader is referred to [13].

Die approbierte gedruckte Originalversion dieser Diplomarbeit ist an der TU Wien Bibliothek verfügbar
The approved original version of this thesis is available in print at TU Wien Bibliothek.

6.2.1. Unresolved DEM-CFD Coupling

In the so-called unresolved or point-force DEM-CFD coupling approach, the shape of particles is not resolved in the CFD simulation. Averaging models are used to convert Lagrangian particle data into an Eulerian frame of reference (void fraction, etc.) [13]. Hence, the fluid flow between the particles is not resolved. The averaged particle data appear as volumetric source terms in the Navier-Stokes equations. Different coupling schemes (drag models, heat transfer models) are available to consider the impact of the fluid phase on individual particles [12], [46].

To ensure that averaging models give good results, particles are usually desired to be smaller than the CFD mesh, see Figure 6.1. Depending on the particle size and the computational domain (geometry) of the simulation, this can be a problematic constraint on the cell size of the mesh.

Unresolved DEM-CFD coupling is a comparatively cheap computational model and therefore the method of choice in this work.

6.2.2. Resolved DEM-CFD Coupling

The resolved DEM-CFD coupling approach makes use of the Fictitious Domain Method (FDM). Terms such as Immersed Boundary (IB) method [51], [52] or Fully Resolved Numerical simulation (FRS) method [53] are also used in this context. A classification of existing methods with regard mesh handling is provided in [54].

The characteristic of the resolved method lies in the separate treatment of the computational domain for the fluid and solid phase. The cell size of the computational grid is smaller than the particles, see Figure 6.1, and the inter-particle fluid flow is calculated. Resolved DEM-CFD coupling is computationally more expensive than an unresolved approach.

6.3. Solver Modifications

Modifications of available solvers are necessary due to the choice of software and the objectives of this work, see 5 and 8.2 respectively. In CFDEMcoupling-PUBLIC, only incompressible solvers are available. However, in this work it is essential to consider the change of density due to temperature.

Die approbierte gedruckte Originalversion dieser Diplomarbeit ist an der TU Wien Bibliothek verfügbar
The approved original version of this thesis is available in print at TU Wien Bibliothek.

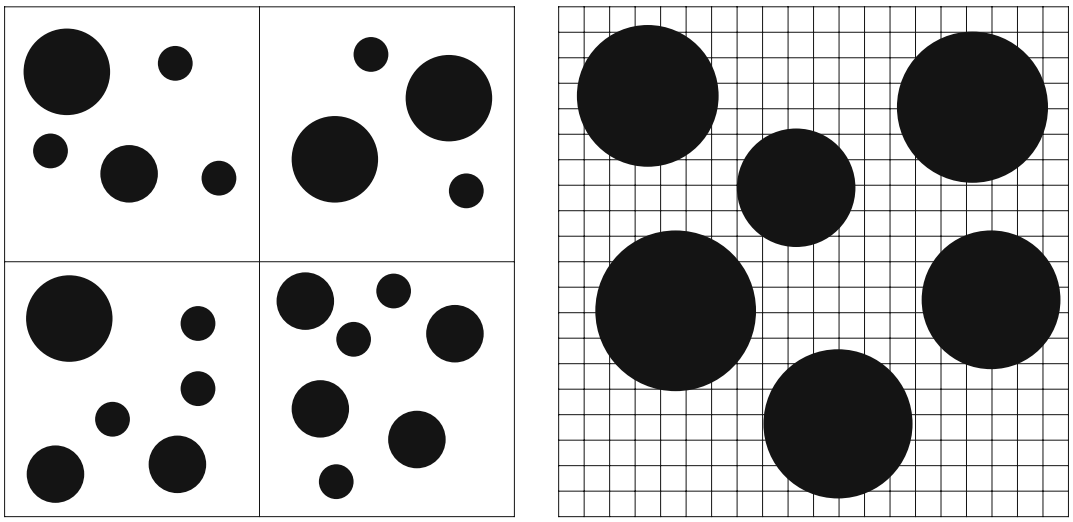

Figure 6.1.: Comparison of unresolved (left) and resolved (right) DEM-CFD method with regard to the relation of cell and particle size.

6.3.1. Void Fraction

As explained in 6.2.1, the unresolved DEM-CFD coupling approach makes use of a source term to account for the volume fraction of a fluid cell occupied by particles. The void fraction α_f is defined as

$$\alpha_f = \frac{V_f - \sum V_p}{V_f} = 1 - \frac{\sum V_p}{V_f} \,. \tag{6.1}$$

In particle free space, the void fraction is equal to $\alpha_f = 1$. If a volume is completely occupied by solids, i. e. no fluid is present, the void fraction is equal to $\alpha_f = 0$. The complement, the solid void fraction α_s, can be written as

$$\alpha_s = 1 - \alpha_f \,. \tag{6.2}$$

6.3.2. Relative Density

In OpenFOAM, incompressible solvers use the so-called *'reduced pressure'*, which is the quotient of the pressure p and the fluid density ρ_f

$$\overline{p} = \frac{p}{\rho_f} \,. \tag{6.3}$$

Die approbierte gedruckte Originalversion dieser Diplomarbeit ist an der TU Wien Bibliothek verfügbar
The approved original version of this thesis is available in print at TU Wien Bibliothek.

To retain the framework of the source code and reduce modifications of already available solvers to a minimum, the *'relative density'* R_f is introduced. It is a dimensionless quantity calculated from the ratio of fluid density ρ_f and a reference density ρ_{ref}

$$R_f = \frac{\rho_f}{\rho_{ref}} \,. \tag{6.4}$$

If the governing equations are extended by the relative density to account for density change, an additional equation is needed for closure of the system. The equation of state is used for this purpose.

6.3.3. Incompressible Ideal Gas Law

The equation of state for an ideal gas is basically a function of temperature T and pressure p

$$\rho = \rho(p, T) = \frac{p}{R_s\, T} \,, \tag{6.5}$$

with R_s being the specific gas constant. The dependency of the density is investigated with regard to pressure and temperature. Previous examinations of the sinter cooler facility have shown that the pressure difference across the shaft cooler is approximately in the range of 2000 Pa to 6000 Pa. In 8, the air temperature is specified in a range from 30 °C to 500 °C.

The change of density based on a pressure gradient of 6000 Pa is compared to the change with respect to the above mentioned temperature range. The outcome is related to the density at 30 °C and 1.013 25 bar. This results in a density change due to pressure of 5.92 % compared to a change due to temperature of 60.79 %.

Since the density change due to the pressure gradient is much smaller, the equation of state is considered to be only a function of the temperature at a constant reference pressure (operating pressure)

$$\rho = \rho(T) = \frac{p_{ref}}{R\, T} \,. \tag{6.6}$$

As a result of the elimination of the pressure dependency, better convergence properties of the modified solver are expected. Equation (6.6) is sometimes called *'incompressible ideal gas law'* [55] or equation of state for an *'incompressible perfect gas'* [43].

Combining (6.4) and (6.6), the relative density can also be written as

Die approbierte gedruckte Originalversion dieser Diplomarbeit ist an der TU Wien Bibliothek verfügbar
The approved original version of this thesis is available in print at TU Wien Bibliothek.

$$R_f = \frac{\rho_f}{\rho_{ref}} = \frac{T_{ref}}{T_f}\,. \tag{6.7}$$

6.4. Governing Equations

The governing equations for the modified solver are derived from the equations for compressible flow through division by a reference density ρ_{ref} and employment of the relative density definition in (6.4). The constitutive equations for compressible and incompressible flow can be found in B.1 and B.2 respectively.

6.4.1. Continuity Equation

No species transport between the solid and the fluid phase is considered, hence the source term on the right-hand side of the continuity equation is equal to zero.

$$\frac{\partial(R_f\alpha_f)}{\partial t} + \nabla\cdot(R_f\alpha_f\vec{u}_f) = 0\,, \tag{6.8}$$

where R_f is the relative density according to (6.4), α_f the void fraction according to (6.1) and $\vec{u}_f$ the velocity vector.

6.4.2. Momentum Equation

Gidaspow [56] proposed two models to predict the pressure drop for multiphase flows, referred to as Model A and Model B. Model A assumes that the pressure drop acts on both the fluid and solid phase. Model B considers the pressure drop in the fluid phase only. According to [12], comparison between the experimental and simulation results suggest Model B is favored. However, the authors also note that further studies may be necessary for confirmation. In this work, Model B is employed and the momentum equation can be written as

$$\frac{\partial(R_f\alpha_f\vec{u}_f)}{\partial t} + \nabla\cdot(R_f\alpha_f\vec{u}_f\vec{u}_f) = \nabla\cdot(\nu_{ref}\alpha_f\nabla(\vec{u}_f)) - \nabla\overline{p}_{ref} + \frac{R_f\vec{S}_m(\rho_{ref})}{\rho_{ref}}\,, \tag{6.9}$$

with the kinematic viscosity ν_{ref} at the temperature T_{ref}

Die approbierte gedruckte Originalversion dieser Diplomarbeit ist an der TU Wien Bibliothek verfügbar
The approved original version of this thesis is available in print at TU Wien Bibliothek.

$$\nu_{ref} = \frac{\mu_f}{\rho_{ref}}\,, \tag{6.10}$$

and the reduced pressure gradient

$$\nabla \overline{p}_{ref} = \frac{\nabla p}{\rho_{ref}}\,. \tag{6.11}$$

The momentum source term $\vec{S}_m(\rho_{ref})$ is calculated according to the incompressible model implemented in the CFDEMcoupling framework, which is based on the reference density ρ_{ref} and the reference kinematic viscosity ν_{ref}. As shown in (6.16) and (6.17), the momentum source term can be written as a linear function of the density. Consequently, the incompressible momentum source term is corrected by multiplication with the relative density R_f to account for density change, which yields the compressible momentum source term

$$\vec{S}_m(\rho_f) = R_f \vec{S}_m(\rho_{ref})\,. \tag{6.12}$$

Momentum Source Term

The source term in the momentum equation according to [56] is based on the Ergun equation for $\alpha_f \leq 0.8$ and on the drag force for a single sphere for $\alpha_f > 0.8$. A problem connected with the utilization of this model is the sharp transition from one formulation to the other at $\alpha_f = 0.8$.

Ergun Equation ($\alpha_f \leq 0.8$)

The pressure gradient (pressure drop) across a packed bed can be described using the Ergun equation in consideration of a laminar and a turbulent part (linear and quadratic dependency on the velocity respectively), e. g. given in [13] or [57],

$$\nabla p_x = \frac{\Delta p}{\Delta x} = \underbrace{150\frac{(1-\alpha_f)^2}{\alpha_f^3}\frac{\mu_f U_0}{(\Phi d_p)^2}}_{laminar} + \underbrace{1.75\frac{(1-\alpha_f)}{\alpha_f^3}\frac{\rho_f U_0^2}{\Phi d_p}}_{turbulent}\,, \tag{6.13}$$

where Φ denotes the particle shape factor. Inserting the superficial velocity $U_0 = \alpha_f(u_f - u_s)$ according to [56], it follows

Die approbierte gedruckte Originalversion dieser Diplomarbeit ist an der TU Wien Bibliothek verfügbar
The approved original version of this thesis is available in print at TU Wien Bibliothek.

$$\frac{\Delta p}{\Delta x} = (u_f - u_s) \underbrace{\left[150 \frac{(1-\alpha_f)^2}{\alpha_f^2} \frac{\mu_f}{(\Phi d_p)^2} + 1.75 \frac{(1-\alpha_f)}{\alpha_f} \frac{\rho_f (u_f - u_s)}{\Phi d_p} \right]}_{\beta_B} . \tag{6.14}$$

Substituting the dynamic viscosity by $\mu_f = \nu_f \rho_f$ in (6.14), the friction coefficient β_B (according to Model B) can be written as a linear function of density $\beta_B = \beta_B(\rho_f)$. For $\alpha_f \leq 0.8$ it can be written as

$$\beta_B(\rho_f) = \left[150 \frac{(1-\alpha_f)^2}{\alpha_f^2} \frac{\nu_f}{(\Phi d_p)^2} + 1.75 \frac{(1-\alpha_f)}{\alpha_f} \frac{(u_f - u_s)}{\Phi d_p} \right] \rho_f . \tag{6.15}$$

The source term in the momentum equation based on the Ergun equation yields

$$S_m(\rho_f) = (u_f - u_s) \beta_B(\rho_f) . \tag{6.16}$$

Following the procedure according to (6.12), a discrepancy in the laminar term of the Ergun equation occurs due to the substitution of the dynamic viscosity with $\mu_f = \nu_f \rho_f$. As mentioned in 10.4, the fluid properties are assumed to be constant in the CFD simulation, i. e. temperature independent. If the kinematic viscosity is equal to a constant mean value $\overline{\nu}_f$, the dynamic viscosity $\mu_f = \overline{\nu}_f \rho_f$ is not constant because of the temperature dependent density ρ_f.

Hence, an error is made if the incompressible model for the calculation of the momentum source term is used. To estimate the impact of this error, the regarding quantities are summarized for some temperature values in Table 6.1.

Table 6.1.: Temperature dependence of the material properties for dry air, from [57].

T [°C]	ρ [kg/m^3]	ν [10^{-6} m^2/s]	μ [10^{-6} Pa s]
0	1.276	13.50	17.22
100	0.9333	23.46	21.90
200	0.7359	35.39	26.05
300	0.6075	49.07	29.81

As one can see, the density is decreasing with rising temperature. On the contrary, both the kinematic and the dynamic viscosity are increasing. Thus, the calculation of the dynamic viscosity according to $\mu_f = \overline{\nu}_f \rho_f$ gives inaccurate results.

Die approbierte gedruckte Originalversion dieser Diplomarbeit ist an der TU Wien Bibliothek verfügbar
The approved original version of this thesis is available in print at TU Wien Bibliothek.

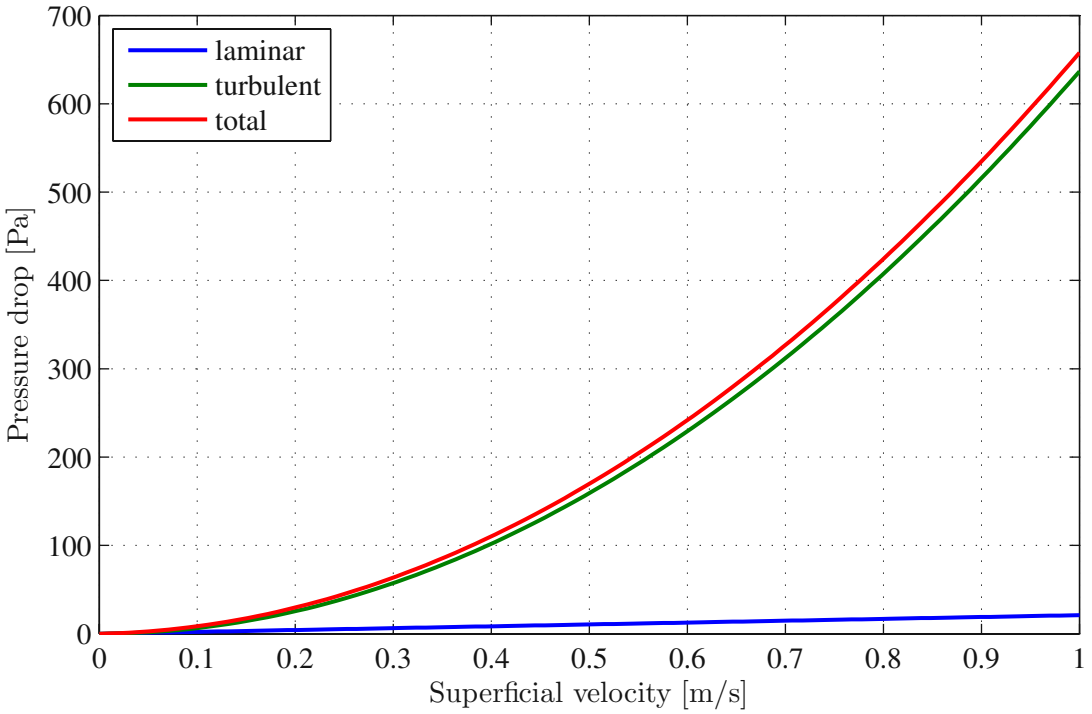

Figure 6.2.: Comparison of the laminar and the turbulent part of the Ergun equation for $d_p = 0.022\,\mathrm{m}$, $\rho_f = 1.293\,\mathrm{kg/m^3}$, $\nu_f = 1.5 \times 10^{-5}\,\mathrm{m^2/s}$, $L = 0.9\,\mathrm{m}$, $\alpha_f = 0.434\,75$ and $\Phi = 1$.

The contribution of the laminar and the turbulent term of the Ergun equation to the total pressure drop is depicted in Figure 6.2. Since the laminar part is comparably small over the entire superficial velocity range, the error introduced by the viscosity is negligible. Therefore, the model for the incompressible momentum source term is used in this work.

Alternatively, a new model for the calculation of the compressible momentum source term can be implemented to correct the viscosity error.

Single Sphere Drag ($\alpha_f > 0.8$)

For dilute regions, the friction coefficient can be calculated based on the drag coefficient for a single sphere

$$\beta_B = \frac{3}{4} C_D \frac{(1-\alpha_f)\rho_f(u_f - u_s)}{(\Phi d_p)} \underbrace{f(\alpha_f)}_{=\alpha_f^{-2.65}} . \tag{6.17}$$

Die approbierte gedruckte Originalversion dieser Diplomarbeit ist an der TU Wien Bibliothek verfügbar
The approved original version of this thesis is available in print at TU Wien Bibliothek.

The correction term $f(\alpha_f)$ takes the presence of other spheres in the fluid into account. According to [56], this term is considered to be equal to

$$f(\alpha_f) = \alpha_f^{-2.65}\,. \tag{6.18}$$

The drag coefficient is related to the particle Reynolds number (solid Reynolds number) as follows

$$C_D = \begin{cases} \frac{24}{\alpha_f\, Re_p}\left[1 + 0.15(\alpha_f\, Re_p)^{0.687}\right] & \text{if } (\alpha_f\, Re_p) < 1000\,, \\ 0.44 & \text{if } (\alpha_f\, Re_p) \geq 1000\,. \end{cases} \tag{6.19}$$

With the particle Reynolds number and the superficial velocity $U_0 = \alpha_f(u_f - u_s)$

$$Re_p = \frac{U_0\, d_p}{\alpha_f\, \nu_f} = \frac{(u_f - u_s)\, d_p}{\nu_f}\,. \tag{6.20}$$

For $(\alpha_f\, Re_p) > 1000$ the fluid flow through the packed bed is considered to be fully turbulent.

6.4.3. Energy Equation

The conservation equation for thermal energy with respect to the relative density R_f and the enthalpy $h_f = c_{p,f}T_f$ reads

$$\frac{\partial(R_f\alpha_f T_f)}{\partial t} + \nabla\cdot(R_f\alpha_f\vec{u_f}T_f) = \nabla\cdot(D_{T,ref}\alpha_f\nabla(T_f)) + \frac{S_e}{\rho_{ref}c_{p,f}}\,, \tag{6.21}$$

whereas α_f is the void fraction, T_f the fluid temperature, $\vec{u_f}$ the velocity vector and $D_{T,ref}$ the reference thermal diffusivity. The latter is equal to

$$D_{T,ref} = \frac{\lambda_f}{\rho_{ref}c_{p,f}}\,, \tag{6.22}$$

where λ_f is the thermal conductivity, ρ_{ref} the reference density and $c_{p,f}$ the specific heat capacity. The energy source term S_e accounts for convective heat transfer between the fluid and particulate phase. Radiant heat transfer is neglected in this work.

Die approbierte gedruckte Originalversion dieser Diplomarbeit ist an der TU Wien Bibliothek verfügbar
The approved original version of this thesis is available in print at TU Wien Bibliothek.

Energy Source Term

The heat transfer coefficient h can be calculated from the particle Nusselt number Nu_p as follows

$$h = \frac{\lambda_f Nu_p}{d_p}\,, \tag{6.23}$$

where λ_f denotes the thermal conductivity of the fluid and d_p is the particle diameter.

The convective heat flux $\dot{Q}_p$ between the fluid and particulate phase reads

$$\dot{Q}_p = h\, A_p\, (T_f - T_p)\,, \tag{6.24}$$

with A_p being the particle surface and T_f and T_p being the fluid and particle temperature respectively.

The volumetric source term S_e in the energy equation for the fluid phase can be written as

$$S_e = -\frac{\dot{Q}_p}{V_{cell}}\,, \tag{6.25}$$

where V_{cell} is the volume of the regarding fluid cell.

Nusselt Correlation

The particle Reynolds number as defined in (6.20) is used to calculate the Nusselt number. Numerous Nusselt correlations for the particulate phase are reported in the literature. The most important distinction is between dilute and dense granular flows. Three different correlations are investigated in the following.

Li and Mason

The Nusselt correlation according to Li and Mason [58] was found to be adequate for particle assemblies of dilute phase flows of polymer pellets.

$$Nu_p = \begin{cases} 2 + 0.6\,\alpha_f^n\, Re_p^{1/2}\, Pr^{1/3} & \text{if } Re_p < 200\,, \\ 2 + 0.5\,\alpha_f^n\, Re_p^{1/2}\, Pr^{1/3} + 0.02\,\alpha_f^n\, Re_p^{0.8}\, Pr^{1/3} & \text{if } 200 < Re_p < 1500\,, \\ 2 + 0.000045\,\alpha_f^n\, Re_p^{1.8} & \text{if } Re_p > 1500\,, \end{cases} \tag{6.26}$$

Die approbierte gedruckte Originalversion dieser Diplomarbeit ist an der TU Wien Bibliothek verfügbar
The approved original version of this thesis is available in print at TU Wien Bibliothek.

where Pr is the Prandtl number according to

$$Pr = \frac{c_{p,f}\,\nu_{ref}\,\rho_{ref}}{\lambda_f}\,. \tag{6.27}$$

Deen et al.

In [59], the Gunn correlation [60] based on experimental results was refitted using Direct Numerical Simulation (DNS)

$$Nu_p = \left(7 - 10\alpha_f + 5\alpha_f^2\right)\left(1 + 0.17Re_p^{0.2}Pr^{1/3}\right) + \left(1.33 - 2.31\alpha_f + 1.16\alpha_f^2\right)Re_p^{0.7}Pr^{1/3}\,. \tag{6.28}$$

This correlation is suited for dense particle-fluid systems [41]. However, the authors only extracted Nusselt numbers at Reynolds numbers between 0 and 100.

VDI Heat Atlas

In [57], the average heat transfer coefficient is calculated from a Nusselt correlation for a single sphere and a shape factor accounting for an increased heat transfer for flow through a packed bed. The Nusselt correlation for a single sphere consists of a laminar and a turbulent part

$$Nu_p = f_a\left(2 + \sqrt{Nu_{p,lam}^2 + Nu_{p,turb}^2}\right)\,. \tag{6.29}$$

The laminar part of the Nusselt number $Nu_{p,lam}$ can be written as

$$Nu_{p,lam} = 0.664\,Re_p^{1/2}Pr^{1/3}\,. \tag{6.30}$$

The turbulent part of the Nusselt number $Nu_{p,turb}$ can be expressed as

$$Nu_{p,turb} = \frac{0.037\,Re_p^{0.8}\,Pr}{1 + 2.443\,Re_p^{-0.1}\left(Pr^{2/3} - 1\right)}\,. \tag{6.31}$$

To convert the Nusselt number for a single sphere to a packed bed, the shape factor f_a is used

$$f_a = 1 + 1.5\left(1 - \alpha_f\right)\,. \tag{6.32}$$

Die approbierte gedruckte Originalversion dieser Diplomarbeit ist an der TU Wien Bibliothek verfügbar
The approved original version of this thesis is available in print at TU Wien Bibliothek.

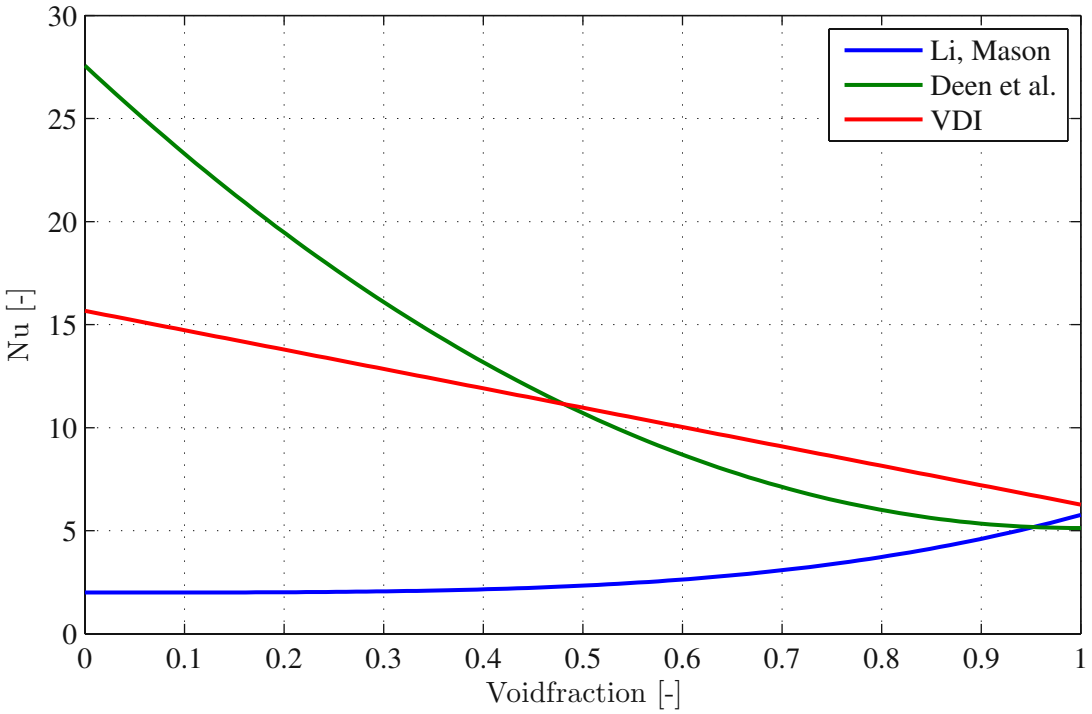

Figure 6.3.: Nusselt number with dependece on the void fraction for $Re = 50$ and $Pr = 0.7$.

This correlation is reported to be valid for a range of $0.1 < Re_p < 10^4$. However, it has to be highlighted that it is intended for the calculation of the heat flux through a packed bed using the average heat transfer coefficient derived from (6.29) and the logarithmic temperature difference of inlet and outlet temperature of the fluid.

Comparison

The above mentioned Nusselt correlations are compared as a function of void fraction for a constant Prandtl number of $Pr = 0.7$ and Reynoldsnumbers of $Re = 50$, see Figure 6.3, and $Re = 5000$, see Figure 6.4.

It is noticeable that the correlation of Li and Mason [58] shows a different tendency with regard to the void fraction. This might be due to the fact that is developed for dilute flows. The Nusselt numbers according to Deen et al. [59] and VDI Heat Atlas [57] are evolving similarly, whereas the former one seems to predict a better heat transfer between the fluid and particulate phase, especially for higher Reynolds numbers.

The void fraction for the packed bed is mainly in the range of $0.4 < \alpha_f < 0.45$, see Figure 12.3 (c). Both Nusselt correlations suitable for dense particulate flows show comparable results in this range, especially for smaller Reynolds numbers. It this work, the correlation of Deen et al. [59]

Die approbierte gedruckte Originalversion dieser Diplomarbeit ist an der TU Wien Bibliothek verfügbar
The approved original version of this thesis is available in print at TU Wien Bibliothek.

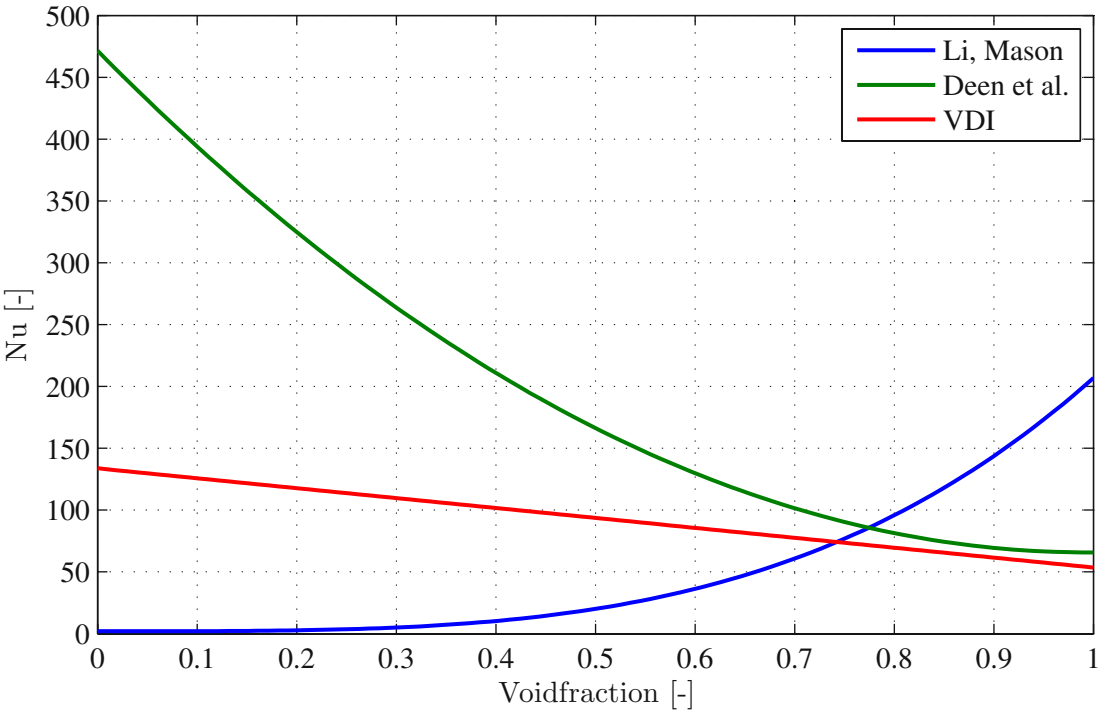

Figure 6.4.: Nusselt number with dependece on the void fraction for $Re = 5000$ and $Pr = 0.7$.

is used because it was developed for granular simulations rather than calculation of an average heat transfer coefficient in a packed bed.

6.5. Coarse-Graining Correction

In 4.2.1, a coarse-graining approach to scale up the particle size is described. In this work, the particle diameter is scaled according to

$$d_{cg} = d_p \, c_{cg} \, . \tag{6.33}$$

Due to spherical shape of the particles, the particle volume and mass is scaling with a factor of c_{cg}^3 as follows

$$V_{cg} = \frac{d_{cg}^3 \pi}{6} = \frac{(d_p c_{cg})^3 \pi}{6} = c_{cg}^3 \frac{d_p \pi}{6} = c_{cg}^3 V_p \, , \tag{6.34}$$

$$m_{cg} = \rho_s V_{cg} = \rho_s c_{cg}^3 V_p = c_{cg}^3 m_p \, . \tag{6.35}$$

Die approbierte gedruckte Originalversion dieser Diplomarbeit ist an der TU Wien Bibliothek verfügbar
The approved original version of this thesis is available in print at TU Wien Bibliothek.

If coarse-graining is applied in connection with coupled DEM-CFD simulations, correction factors have to be introduced to account for realistic behavior of the scaled particles. The procedure for the momentum and energy equation is explained in the following. Simulation tests related to coarse-graining have been performed in 7.1.

6.5.1. Momentum Equation

The particle Reynolds number and the friction coefficient are calculated with the original, unscaled particle diameter to account for a realistic motion of the coarse-grained particle due to drag forces. To consider the same change of impulse, the forces on the particle have to scale with a factor of c_{cg}^3

$$m_p \underbrace{\frac{dv}{dt}}_{const} = \sum_i F_{p,i}\,, \tag{6.36}$$

$$m_{cg}\frac{dv}{dt} = c_{cg}^3 \underbrace{m_p \frac{dv}{dt}}_{(6.36)} = c_{cg}^3 \sum_i F_{p,i}\,. \tag{6.37}$$

6.5.2. Energy Equation

The dimensionless quantities (Reynolds and Nusselt number) and the particle surface area are calculated with the original particle diameter d_p to account for a realistic heat transfer coefficient. Since the mass of the particle is scaling with a factor of c_{cg}^3, also the heat flux between the particle and the interstitial fluid has to scale with a factor of c_{cg}^3 to account for the same temperature difference $\Delta T = T_f - T_p$. The first law of thermodynamics considering only the change of energy by heat transfer between the particle and the fluid can be written as

$$d\dot{Q}_p = \frac{dE_p}{dt} = m_p\, c_s \frac{dT}{dt}\,. \tag{6.38}$$

For a coarse-grained particle the first law of thermodynamics can be expressed as follows

$$d\dot{Q}_{cg} = \frac{dE_{cg}}{dt} = m_{cg}\, c_s \frac{dT}{dt} = c_{cg}^3\, m_p\, c_s \frac{dT}{dt} = c_{cg}^3\, d\dot{Q}_p\,. \tag{6.39}$$

Die approbierte gedruckte Originalversion dieser Diplomarbeit ist an der TU Wien Bibliothek verfügbar
The approved original version of this thesis is available in print at TU Wien Bibliothek.

6.6. Time-Scaling Correction

Since the residence time of a single particle in the shaft cooler is very high, the solid flow can be sped up with the time-scaling factor c_{ts} to ensure a reasonable simulation time

$$u_{s,ts} = c_{ts} u_s \,. \tag{6.40}$$

It has to be observed that the increased particle velocity does not influence the general behavior of the solid flow. The solid mass flow through a certain surface area A can be written as

$$\dot{m}_s = \rho_s u_s A \,. \tag{6.41}$$

Due to a constant particle density ρ_s, the time-scaling factor can also be directly applied to the solid mass flow

$$\dot{m}_{s,ts} = c_{ts} \dot{m}_s \,. \tag{6.42}$$

The time-scaling approach has to fulfill the condition that the effect on the relative velocity between the particle and the fluid due to scaling of the solid velocity is small ($u_f - u_s \approx u_f - u_{s,ts} \approx const$, due to $u_f \gg u_s$ and $u_f \gg u_{s,ts}$). This leads to a similar particle-fluid heat transfer coefficient, see 6.4.3 and 6.4.3, and momentum source term 6.4.2.

The energy balance for convective heat transfer between the fluid and the solid phase can be written as

$$\dot{Q}_s + \dot{Q}_f = 0 \,. \tag{6.43}$$

The temperature of the particles and the fluid have to be depicted in a realistic manner, i. e. the same temperature differences in the scaled and unscaled case apply. Therefore, the heat flux for the solid phase $\dot{Q}_s$ and the fluid phase $\dot{Q}_f$ is kept constant if time-scaling is applied

$$\dot{Q}_s = \sum_{particles} \dot{m}_p c_s \underbrace{(T_{p,1} - T_{p,2})}_{\Delta T_p} = const \,, \tag{6.44}$$

$$\dot{Q}_f = \dot{m}_f c_{p,f} \underbrace{(T_{f,1} - T_{f,2})}_{\Delta T_f} = const \,. \tag{6.45}$$

Die approbierte gedruckte Originalversion dieser Diplomarbeit ist an der TU Wien Bibliothek verfügbar
The approved original version of this thesis is available in print at TU Wien Bibliothek.

To keep the energy balance constant in case of time-scaling, the solid thermal capacity is reduced to the same degree as the particulate flow is sped up, i. e.

$$c_{s,ts} = \frac{c_s}{c_{ts}} \,. \tag{6.46}$$

Comparison of the solid heat flux before and after time-scaling following this approach yields

$$\dot{m}_{s,ts}\, c_{s,ts}\, \Delta T_p = \cancel{c_{ts}}\, \dot{m}_s \frac{c_s}{\cancel{c_{ts}}} \Delta T_p \qquad \rightarrow \qquad \dot{Q}_{s,ts} = \dot{Q}_s = const \,. \tag{6.47}$$

Die approbierte gedruckte Originalversion dieser Diplomarbeit ist an der TU Wien Bibliothek verfügbar
The approved original version of this thesis is available in print at TU Wien Bibliothek.

7. Solver Verification

As discussed in 6.3, changes of the CFDEMcoupling source-code are necessary to speed up simulations by a coarse-graining approach and to account for the change of density due to temperature. In the following, the new compressible solver is tested with regard to some minimum requirements. The term *'verification'* has to be distinguished from the term *'validation'*, which denotes the comparison of simulation results with physical experiments.

Verification in the context of this work means to ensure that simple simulation problems fulfill the conservation equations. Furthermore, simulations are compared to analytical solutions.

7.1. Coarse-Graining

In 6.5, corrections for the momentum and energy equations are proposed. In the following, the influence of particle scaling on drag forces and convective heat transfer is investigated.

7.1.1. Fluidization Test Case

In this test case particles are poured into a cylinder with a diameter of 0.0276 m and a height of 0.0553 m. An incompressible fluid enters the domain in normal direction of the bottom surface area and the gravitational acceleration acts in the negative z-direction, see Figure 7.1 (a). The fluid inlet velocity is increased according to a linear ramp from 0.002 m/s to 0.06 m/s. Heat transfer is not considered, thus the fluid density is equal to a constant value of $10\,\mathrm{kg/m^3}$ and the kinematic viscosity is equal to $1.5 \times 10^{-4}\,\mathrm{m^2/s}$.

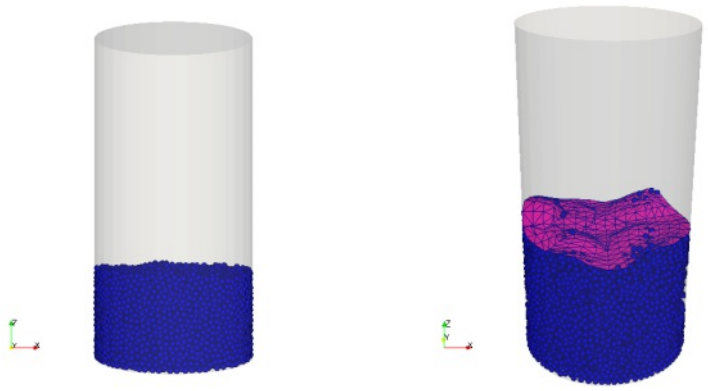

(a) Particles poured into a cylinder (b) Iso-surface for a void fraction of 0.85

Figure 7.1.: Fluidization test case setup.

Die approbierte gedruckte Originalversion dieser Diplomarbeit ist an der TU Wien Bibliothek verfügbar
The approved original version of this thesis is available in print at TU Wien Bibliothek.

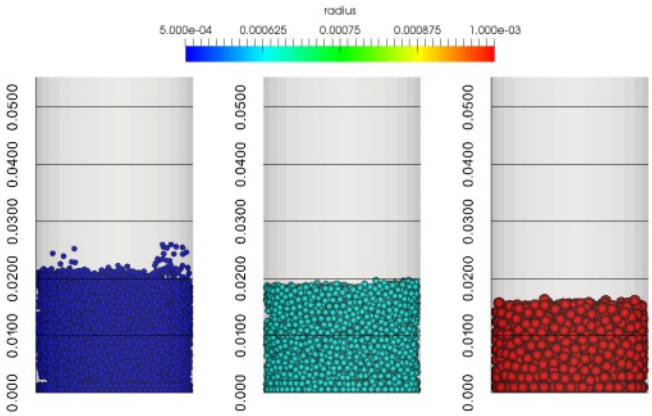

(a) Coarse-graining correction off

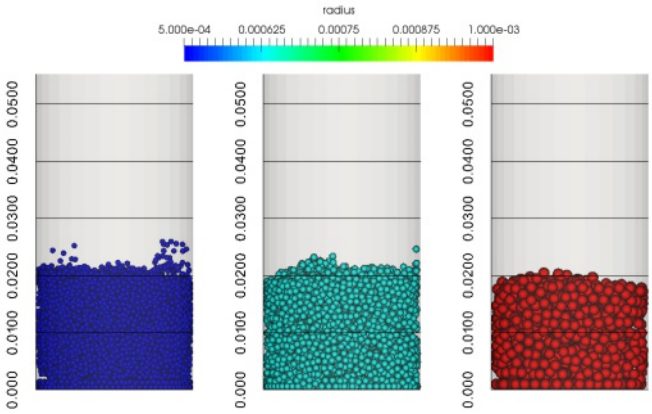

(b) Coarse-graining correction on

Figure 7.2.: Snapshot of the fluidization test case comparing different particle sizes with regard to coarse-graining correction.

The solid material parameters are summarized in Table 7.1. For the fluidization test case no rolling-friction model is applied and it is assumed that the particles and the walls of the cylinder are composed of the same material. The investigated particle diameters and the corresponding coarse-graining factors are specified in Table 7.2.

Table 7.1.: Solid material properties for the fluidization test case.

Property	Symbol	Value and dimension
Density	ρ_s	$2000\,\mathrm{kg/m^3}$
Young's modulus	E	$5.0 \times 10^6\,\mathrm{N/m^2}$
Poisson's ratio	ν_{Po}	0.45
Coeff. of restitution	e	0.3
Coeff. of sliding-friction	μ_s	0.5

Die approbierte gedruckte Originalversion dieser Diplomarbeit ist an der TU Wien Bibliothek verfügbar
The approved original version of this thesis is available in print at TU Wien Bibliothek.

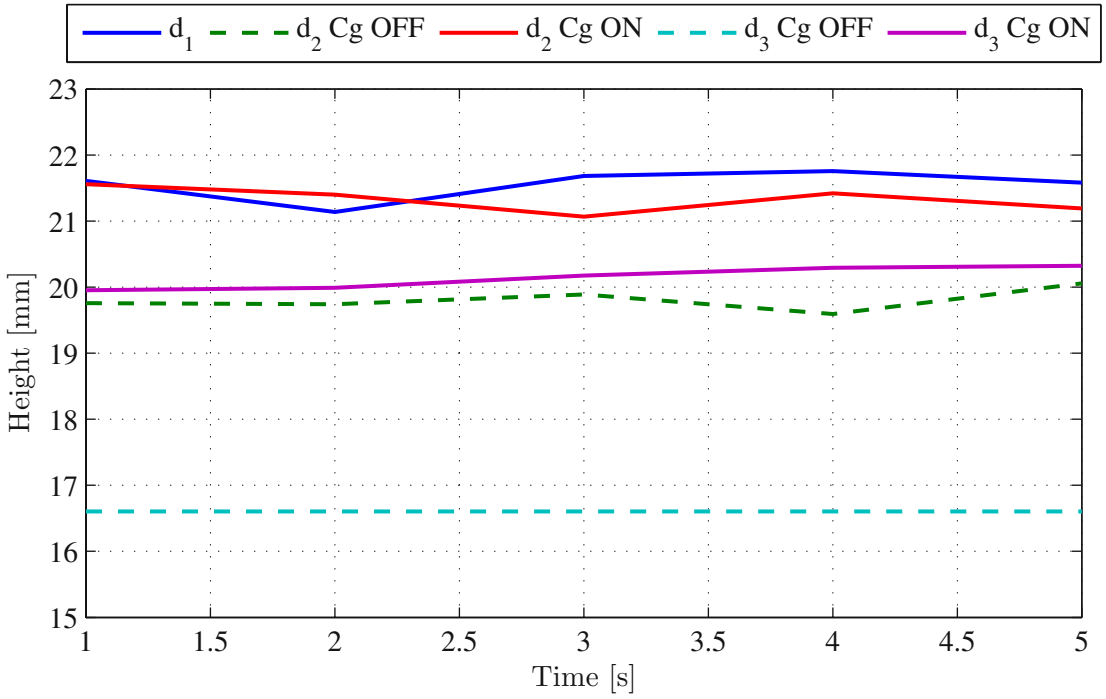

Figure 7.3.: Average height of the free surface between the particulate and fluid phase with regard to particle size and coarse-graining correction.

Figure 7.2 shows a snapshot comparing different particle sizes with regard to coarse-graining correction. It is evident that without coarse-graining correction the fluidization height is very different and the largest particles do not fluidize at all. On the contrary, the resulting height with activated coarse-graining correction seems to be similar.

However, quantitative results are necessary to evaluate the effect of the coarse-graining correction. Therefore, the free surface between the particulate and fluid phase is reflected by the iso-surface for a void fraction of $\alpha_f = 0.85$, see Figure 7.1 (b). After the maximum fluid inlet velocity is reached, the average height of the iso-surface is plotted over the time, see Figure 7.3. The plot confirms reasonable results for activated coarse-graining correction, especially if the coarse-graining factor is small. The discrepancy in fluidzation height for the largest particle size indicates that the correction law could be investigated and improved further.

Also the pressure drop across the fluidized bed is examined with regard to the simulation time, see Figure 7.4. This data again shows good agreement for small coarse-graining factors, but considerable deviation for high coarse-graining factors.

The time-averaged data from the plot of the fluidization height and the pressure drop at the end of the simulation time for activated coarse-graining correction is summarized in Table 7.2.

Die approbierte gedruckte Originalversion dieser Diplomarbeit ist an der TU Wien Bibliothek verfügbar
The approved original version of this thesis is available in print at TU Wien Bibliothek.

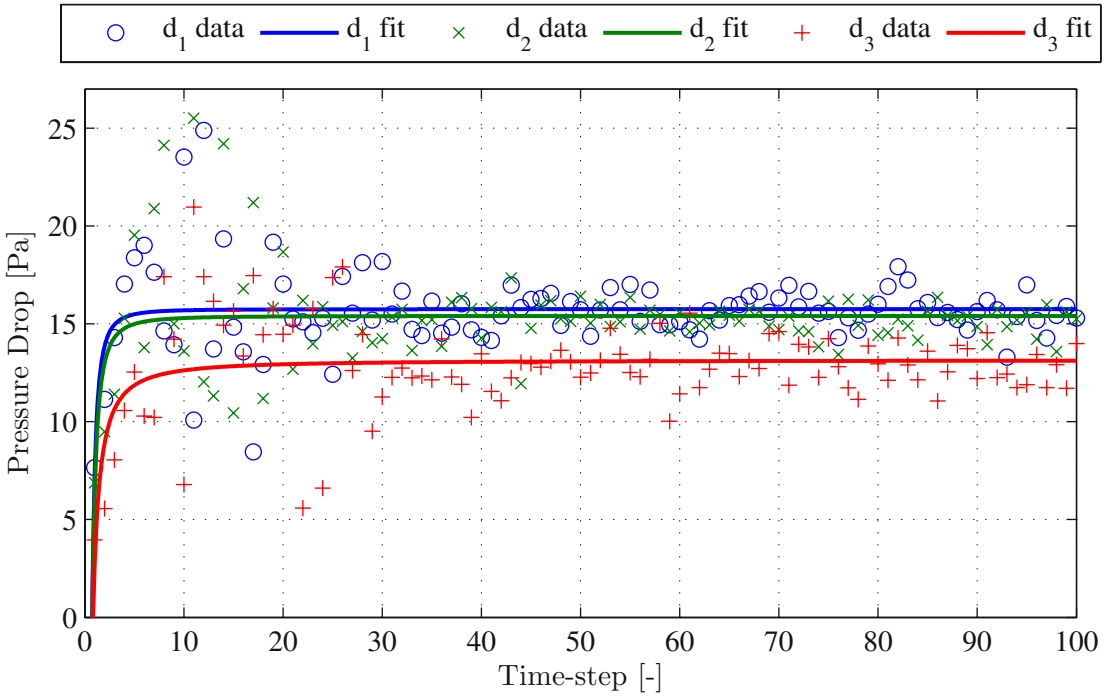

Figure 7.4.: Pressure drop across the fluidized bed with regard to particle size for activated coarse-graining correction.

7.1.2. Convection Test Case

A rectangular column with an edge length of 0.1 m and a height of 2 m is filled with particles at an initial temperature of $T_{p,0} = 300\,\mathrm{K}$. An incompressible fluid flows in at the bottom of the column with a velocity of $u_{f,in} = 1\,\mathrm{m/s}$ and a temperature of $T_{f,in} = 500\,\mathrm{K}$. The particles are heated up for a time of $t = 1.5\,\mathrm{s}$ by convective heat transfer. The solid and fluid material properties are summarized in Table 7.1 and Table 7.3. A snapshot of the particle temperature distribution at the end of the simulation is depicted in Figure 7.5 (b) and (c). On the left-hand side, 1000 particles with a diameter of $d_1 = 22\,\mathrm{mm}$ are placed in the column. On the right-hand side, the column is filled with 500 coarse-grained particles with a diameter of $d_2 = 27.72\,\mathrm{mm}$. This correlates to a coarse-graining factor of $c_{cg} = 1.26$. In case of deactivated coarse-graining

Table 7.2.: Time-averaged fluidization height with regard to particle diameter (d_p), coarse-graining correction deactivated (h_1) or activated (h_2), and area-averaged pressure drop (Δp) at the end of the simulation time for activated coarse-graining correction.

	d_p [mm]	c_{cg} [−]	h_1 [mm]	h_2 [mm]	Δp [Pa]
d_1	1.00	1.00	21.55	21.55	15.75
d_2	1.26	1.26	19.81	21.33	15.40
d_3	2.00	2.00	16.61	20.15	13.10

Die approbierte gedruckte Originalversion dieser Diplomarbeit ist an der TU Wien Bibliothek verfügbar
The approved original version of this thesis is available in print at TU Wien Bibliothek.

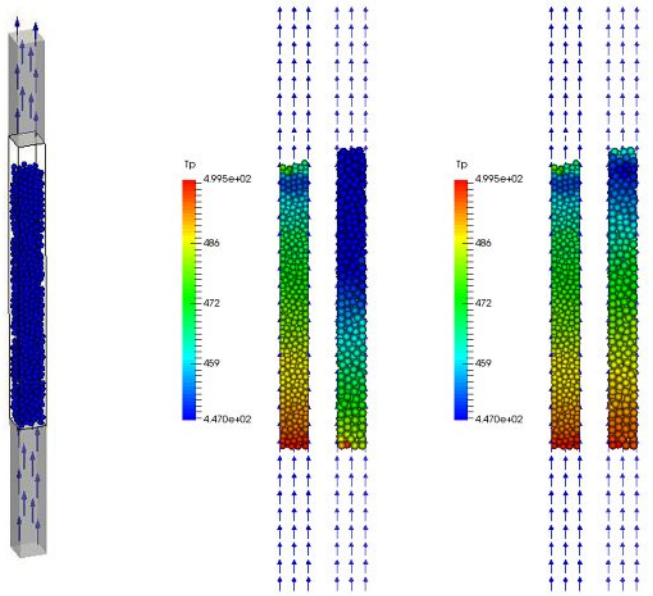

(a) Geometry setup (b) Cg-correction off (c) Cg-correction on

Figure 7.5.: Particle column geometry and snapshot of the particle temperature distribution for the convection test case at $t = 1.5\,\mathrm{s}$.

correction the bigger particles are heated up less by the fluid flow. The result for activated coarse-graining corrections appears to be similar. A plot of the temperature distribution over the normalized height is shown in Figure 7.6. This plot confirms that the coarse-graining correction for convective heat transfer provides good results.

Both above mentioned figures show an artifact that is connected with unresolved DEM-CFD coupling. The particles at the very top are heated up faster because the cell of the CFD mesh in which they are located is not completely filled with particles. Therefore, the void fraction of this cell is higher than of a completely filled one. The Nusselt correlation according to Li and Mason [58] is used for the convection test case. As one can see in Figure 6.3, a higher void fraction yields a better heat transfer coefficient and the particles at the very top are heated up faster.

Table 7.3.: Fluid and solid material properties for the convection test case.

Property	Symbol	Value and dimension
Fluid density	ρ_f	$1.188\,\mathrm{kg/m^3}$
Fluid kinematic viscosity	ν_f	$1.5 \times 10^{-3}\,\mathrm{m^2/s}$
Fluid thermal diffusion coeff.	$D_{T,f}$	$2.1399 \times 10^{-5}\,\mathrm{m^2/s}$
Solid thermal conductivity	λ_s	$5\,\mathrm{W/(m\,K)}$
Solid thermal capacity	$c_{p,s}$	$0.1\,\mathrm{J/(kg\,K)}$

Die approbierte gedruckte Originalversion dieser Diplomarbeit ist an der TU Wien Bibliothek verfügbar
The approved original version of this thesis is available in print at TU Wien Bibliothek.

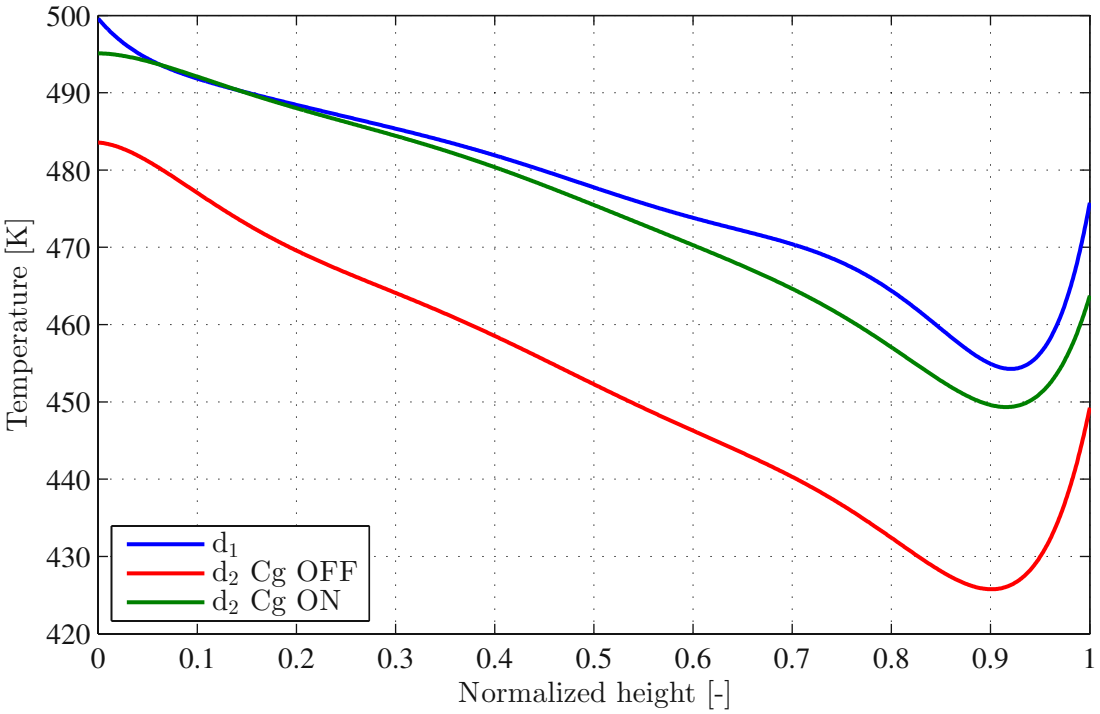

Figure 7.6.: Plot of the fluid temperature distribution of the convective test case a $t = 1.5\,\mathrm{s}$.

7.2. Cold Model

The new compressible solver is compared to an incompressible solver using a cold model, i. e. the temperature of the particles and the fluid is equal. The same settings for the geometry of the column, the particle size (without coarse-graining) and solid material properties as in 7.1.2 are used. The fluid material properties are specified in Table 7.4. The incompressible solver is already implemented in CFDEMcoupling and validated in [30].

The pressure drop across the packed bed is $\Delta p = 655.62\,\mathrm{Pa}$ for both solvers. The decrease in pressure can also be calculated analytically by means of the Ergun equation (6.13), which gives a result of $\Delta p = 657.79\,\mathrm{Pa}$. For the void fraction, the mass-averaged value is calculated from the simulation. The relative error between the simulation and the analytical solution is equal to $\Delta_{rel} = 0.33\,\%$, which indicates excellent agreement.

Table 7.4.: Fluid material properties for the cold model test case.

Property	Symbol	Value and dimension
Density	ρ_f	$1.293\,\mathrm{kg/m^3}$
Kinematic viscosity	ν_f	$1.5 \times 10^{-5}\,\mathrm{m^2/s}$
Thermal diffusion coeff.	$D_{T,f}$	$1.9661 \times 10^{-5}\,\mathrm{m^2/s}$

Die approbierte gedruckte Originalversion dieser Diplomarbeit ist an der TU Wien Bibliothek verfügbar
The approved original version of this thesis is available in print at TU Wien Bibliothek.

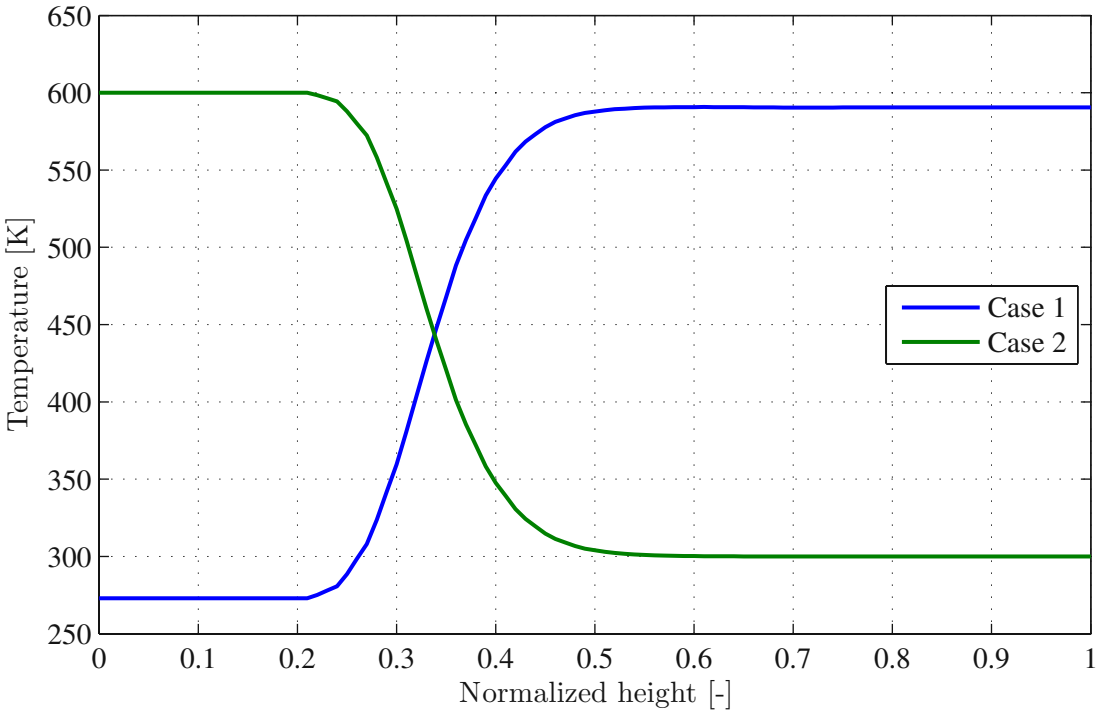

Figure 7.7.: Plot of the fluid temperature profile across the column height.

7.3. Mass Conservation

To verify that the conservation of mass for the fluid phase is satisfied, the new compressible solver is tested for two different boundary and initial condition setups. The rectangular column and the particles described in 7.1.2 are used for this purpose, only the solid thermal properties are modified. The solid thermal capacity of the particles is considered to be relatively high and the resulting temperature gradient for the two test cases is depicted in Figure 7.7.

The density and the velocity at the outlet face can be calculated from the fluid temperature and compared to the simulation results. The incompressible ideal gas law (6.6) can be rewritten as

$$\rho_{out} = \rho_{ref} \frac{T_{ref}}{T_{out}} . \tag{7.1}$$

For a constant cross section the continuity equation yields

$$u_{out} = u_{in} \frac{\rho_{in}}{\rho_{out}} . \tag{7.2}$$

Die approbierte gedruckte Originalversion dieser Diplomarbeit ist an der TU Wien Bibliothek verfügbar
The approved original version of this thesis is available in print at TU Wien Bibliothek.

Table 7.5.: Summary of the test cases for conservation of mass.

Property	Symbol	Dimension	①	②
Fluid inlet temperature	$T_{f,in}$	[K]	273	600
Reference temperature	T_{ref}	[K]	273	600
Reference density	ρ_{ref}	[kg/m^3]	1.293	0.5809
Reference kinematic viscosity	ν_{ref}	[m^2/s]	1.5×10^{-5}	5.166×10^{-5}
Reference thermal diffusivity	$D_{T,ref}$	[m^2/s]	1.9661×10^{-5}	7.464×10^{-5}
Particle initial temperature	$T_{p,0}$	[K]	600	300
Solid thermal conductivity	λ_s	[W/(m K)]	5	5
Solid thermal capacity	$c_{p,s}$	[J/(kg K)]	10	2
Fluid outlet density (simulation)	$\rho_{out,sim}$	[kg/m^3]	0.598	1.162
Fluid outlet density (calculation)	$\rho_{out,calc}$	[kg/m^3]	0.598	1.162
Fluid outlet velocity (simulation)	$u_{out,sim}$	[m/s]	2.16	0.5
Fluid outlet velocity (calculation)	$u_{out,calc}$	[m/s]	2.16	0.5
Pressure drop (simulation)	Δp_{sim}	[Pa]	1270.2	198.2
Pressure drop (calculation)	Δp_{calc}	[Pa]	1239.7	195.4

Also the pressure drop across the packed bed is calculated analytically using the Ergun equation (6.13) and compared to the simulation. The required quantities are calculated from mass-averages (temperature, density, void fraction) and area-averages (velocity).

The settings and the results for the two test cases are summarized in Table 7.5. The data shows very good agreement for density and velocity values. The small error in pressure loss might be due to the determination of the average quantities used in the Ergun equation.

7.4. Energy conservation

To check the correct calculation of the convective heat transfer between the particles and the fluid, another test case is performed. The same simulation settings as in the mass conservation test case (1) are applied, see Table 7.5. Only the solid thermal capacity is chosen equal to 1 J/(kg K). The particles in the column are cooled down for a time of $t = 5\,\mathrm{s}$. At the end of the simulation the particle temperature is equal to the fluid inlet temperature. The overall energy balance for the system can be written as

$$\sum_i \frac{m_p^{(i)}\, c_{p,s}^{(i)}\, dT_p^{(i)}}{dt} = \dot{m}_{f,in}\, c_{p,f}\, T_{f,in} - \dot{m}_{f,out}\, c_{p,f}\, T_{f,out}\,. \tag{7.3}$$

With the continuity equation $\dot{m}_{f,in} = \dot{m}_{f,out} = \dot{m}_f$ and the integral from t_0 to t_{end}, the energy balance yields

Die approbierte gedruckte Originalversion dieser Diplomarbeit ist an der TU Wien Bibliothek verfügbar
The approved original version of this thesis is available in print at TU Wien Bibliothek.

$$\sum_i m_p^{(i)}\, c_{p,s}^{(i)} \left[T_{p,end}^{(i)} - T_{p,0}^{(i)}\right] = \dot{m}_f\, c_{p,f} \int_{t_0}^{t_{end}} \left[T_{f,in} - T_{f,out}\right] dt\,. \tag{7.4}$$

The change of the fluid temperature within the domain does not have to be considered in the energy balance, because it is equal to the inlet temperature at the beginning and the end of the simulation. Therefore, the temperature change of the particles is only caused by the fluid flow due to enthalpy transport across the inlet and outlet boundary face. The inlet temperature of the fluid is constant and the area-averaged fluid outlet temperature is plotted in Figure 7.8.

With all the information given to solve the energy balance in (7.4), the total solid heat flux for all particles is equal to $\dot{Q}_s = 4557.79\,\mathrm{J}$ and the fluid heat flux is $\dot{Q}_f = 4519.16\,\mathrm{J}$. This gives an acceptable relative error of $\Delta_{rel} = 0.85\,\%$.

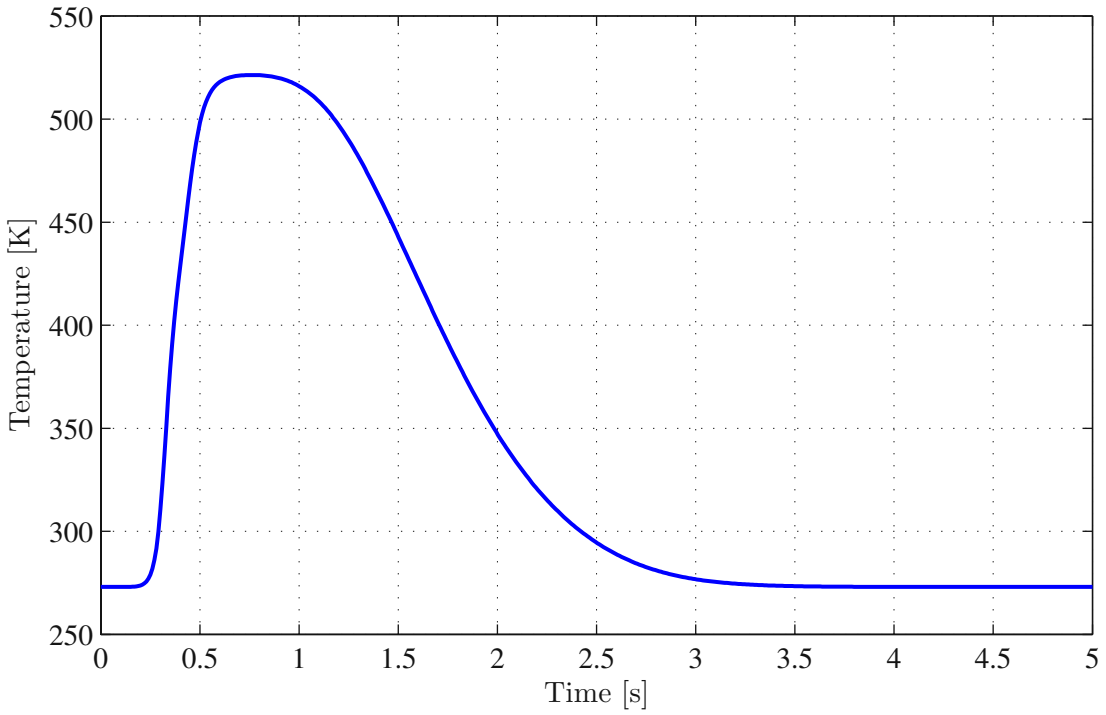

Figure 7.8.: Plot of the fluid temperature at the outlet boundary over time.

Die approbierte gedruckte Originalversion dieser Diplomarbeit ist an der TU Wien Bibliothek verfügbar
The approved original version of this thesis is available in print at TU Wien Bibliothek.

8. Objectives

As mentioned in 1.1, DEM simulations are a suitable tool to investigate local phenomena in the counter-flow sinter shaft cooler. A coupled DEM-CFD simulation is able to depict the influence of the solid flow, such as segregation, on the fluid flow and vice versa. Furthermore, the resulting temperature field for both the sinter material and the cooling air can be investigated in detail. In the following, the objectives of the simulations are summarized.

8.1. Objectives of the DEM Simulations

First, a DEM simulation neglecting the interstitial fluid is performed. The fluid flow has insignificant influence on the solid flow and the simulation run time is considerably shorter without DEM-CFD coupling. The particulate flow is investigated with regard to the following characteristics:

- Segregation due to a given particle-size distribution.
- Particle trajectories through the shaft cooler geometry.
- Through-put time of the particles.
- Formation of dead zones.
- Impact of modeling simplifications and speed-up methods such as truncated particle-size distribution and coarse-graining.

8.2. Objectives of the Coupled DEM-CFD Simulations

It is of crucial importance to understand the basic processes of the fluid-solid interaction inside the shaft cooler to guarantee reliable operation of the facility. Therefore, coupled DEM-CFD simulations are performed to examine the following phenomena:

- Local fluid velocity peaks, e. g. due to segregation.
- Influence of the temperature on the fluid velocity field.
- Pressure drop across the packed bed.
- Particle and air temperature at the corresponding outlet.
- Temperature field of the particulate and the fluid phase inside the shaft cooler.

Die approbierte gedruckte Originalversion dieser Diplomarbeit ist an der TU Wien Bibliothek verfügbar
The approved original version of this thesis is available in print at TU Wien Bibliothek.

An estimation of the temperature influence on the fluid velocity and density shows that this effect cannot be neglected for the present problem. The continuity equation considering a constant cross-section can be written as

$$\rho_1(\vartheta_1)\, u_1 = \rho_2(\vartheta_2)\, u_2\,, \qquad \frac{u_2}{u_1} = \frac{\rho_1(\vartheta_1)}{\rho_2(\vartheta_2)}\,. \tag{8.1}$$

The density of dry air with dependency on the temperature is for example tabulated in [57]. The temperature change is considered to be in the range of $\vartheta_1 = 30\,°\mathrm{C}$ to $\vartheta_2 = 500\,°\mathrm{C}$, which corresponds to the inlet air temperature and the inlet sinter temperature respectively. This yields an increase of the velocity by a factor of 2.55 and a significant influence on the pressure drop and the convective heat transfer.

Die approbierte gedruckte Originalversion dieser Diplomarbeit ist an der TU Wien Bibliothek verfügbar
The approved original version of this thesis is available in print at TU Wien Bibliothek.

9. Excel-Tool

The *"Excel-tool"* is a simulation code written in Visual Basic for Applications (VBA) to improve the engineering process of the sinter cooler facility. The program is characterized by easy utilization within the Excel-worksheet environment, short calculation time and extensive post-processing capabilities.
The gas and solid flows are solved in an axisymmetric manner using continuum models, see Figure 9.1 (a) and (b). A particle distribution of different sizes and mass fractions can be considered as well as particle species including relative humidity. Convection and conduction contribute to the heat transfer between the solid and fluid phase. At the solid outlet, the mean and surface temperature of each particle size is calculated.
Two different calculation modes are available. In forward mode, the pressure at the cooling air inlet is set and the main result of the calculation is the particle temperature at the solid outlet. In reverse mode, the desired temperature of the solid particles at the outlet can be chosen and the pressure at the air inlet is calculated.
The charts-tool facilitates easy post processing using Excel-diagrams. Information such as temperature or velocity can be extracted at different heights of the sinter cooler and plotted along the radial direction. Furthermore, contour plots of all important physical quantities in the sinter cooler calculation are automatically generated, see Figure 9.1 (c).

The main differences between the Excel-tool (version 16, 21.08.2015) and the coupled DEM-CFD simulation are summarized in the following:

- The geometry of the Excel-tool can only be modified within certain limits because the number of corner points is hard-coded. Therefore, the geometry is truncated at the bottom and top, see Figure 9.1 (a).
- The solid outlet corresponds to the entire bottom face, it is not possible to consider only a section of the face.
- The fluid inlet faces extend over the solid-fluid interface area, which is shaped due to the angle of repose, i. e. the calculated inlet velocity in the Excel-tool does not correspond to the superficial velocity set as boundary condition in the coupled DEM-CFD simulation.
- Due to code-restrictions, it is only possible to realize one fluid inlet in conjunction with the shaft cooler geometry.
- The solid flow is modeled in an Eulerian frame of reference (continuum approach) instead of a Lagrangian frame of reference (discrete approach), i. e. dead zones and their influence on the solid velocity field are not predicted.
- Segregation effects are not taken into account.

Die approbierte gedruckte Originalversion dieser Diplomarbeit ist an der TU Wien Bibliothek verfügbar
The approved original version of this thesis is available in print at TU Wien Bibliothek.

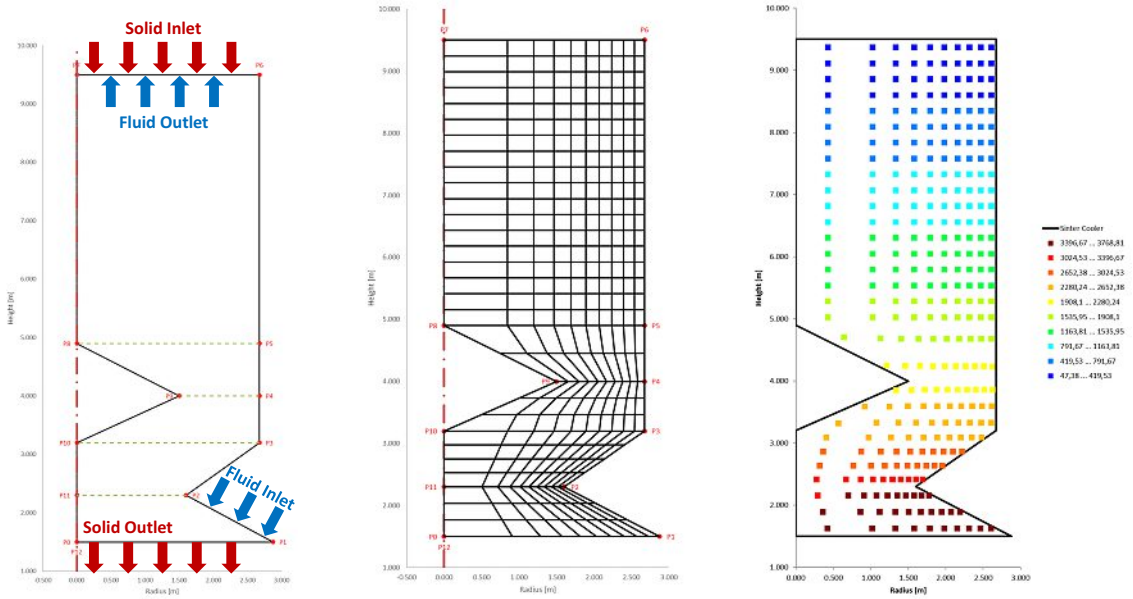

(a) Axisymmetric geometry with inlets and outlets

(b) Quadrilateral mesh

(c) Contour plot of the pressure

Figure 9.1.: Geometry, mesh and pressure contour plot of the Excel-tool.

- No friction within the solid phase and no influence of walls on the solid flow.
- A pressure boundary condition for the fluid inlet has to be specified instead of a velocity boundary condition.

Die approbierte gedruckte Originalversion dieser Diplomarbeit ist an der TU Wien Bibliothek verfügbar
The approved original version of this thesis is available in print at TU Wien Bibliothek.

10. Simulation Setup

In many industrial applications a problem in terms of different length scales connected with particle simulation persists. This also applies to the sinter shaft cooler, because its dimensions are very large compared to the diameter of the particle. If the entire three-dimensional geometry is considered without coarse-graining and truncation of the particle-size distribution, approximately 3×10^9 particles have to be simulated. This huge amount of particles cannot be simulated in a feasible way with today's computer systems. Thus, it is necessary to find suitable modeling approaches and speed-up methods to reduce the number of particles for the DEM simulation.

10.1. Geometry

In Figure 10.1 (a), the three-dimensional geometry of the sinter shaft cooler is shown. The red color indicates the particles in the cooler, whereas the dark grey regions account for dead zones. Sheet metals are depicted in yellow and turquoise.

To decrease the number of particles drastically, the 3D-geometry is reduced to a quasi-axisymmetric representation, see Figure 10.1 (b). The main dimensions are given in Figure 10.1 (c). As mentioned in 5.2, no axisymmetric boundary conditions are implemented in LIGGGHTS-PUBLIC. Thus, the axisymmetric cross-section of the geometry is expanded in the z-direction and periodic boundary conditions are applied. The thickness is equal to the largest particle diameter in the computational domain. The walls of the DEM simulation are colored in blue, the particle-insertion face in red, the symmetry axis in green and the particle-outlet in yellow. Since also no symmetry boundary condition is available in LIGGGHTS-PUBLIC, the symmetry axis has to be modeled as wall. Thus, the particles are not able to penetrate this face. A calibration test to minimize the influence of the symmetry axis on the simulation results is performed in 11.2.
The particle outlet causes problems for the given geometry setup. Clogging due to arching occurs because the symmetry axis is modeled as wall and the particle size is scaled up significantly. Hence, particles are discharged from the shaft cooler by periodic deletion inside of a small virtual volume.

The geometry for the CFD mesh is pictured in grey in Figure 10.1 (b). In principal, an axisymmetric boundary condition is available in OpenFOAM, but the simulation domain would have to be of wedge-shape. Given that the geometry for coupled DEM-CFD simulations has to be compatible, the CFD domain needs to be of rectangular shape. Symmetry boundary conditions are applied in z-direction and along the symmetry axis. Apparently, the domain for the CFD simulation is smaller than the one for the DEM simulation. The truncation is due to the fact that the filling and discharging of particles causes stability problems because of abrupt changes

Die approbierte gedruckte Originalversion dieser Diplomarbeit ist an der TU Wien Bibliothek verfügbar
The approved original version of this thesis is available in print at TU Wien Bibliothek.

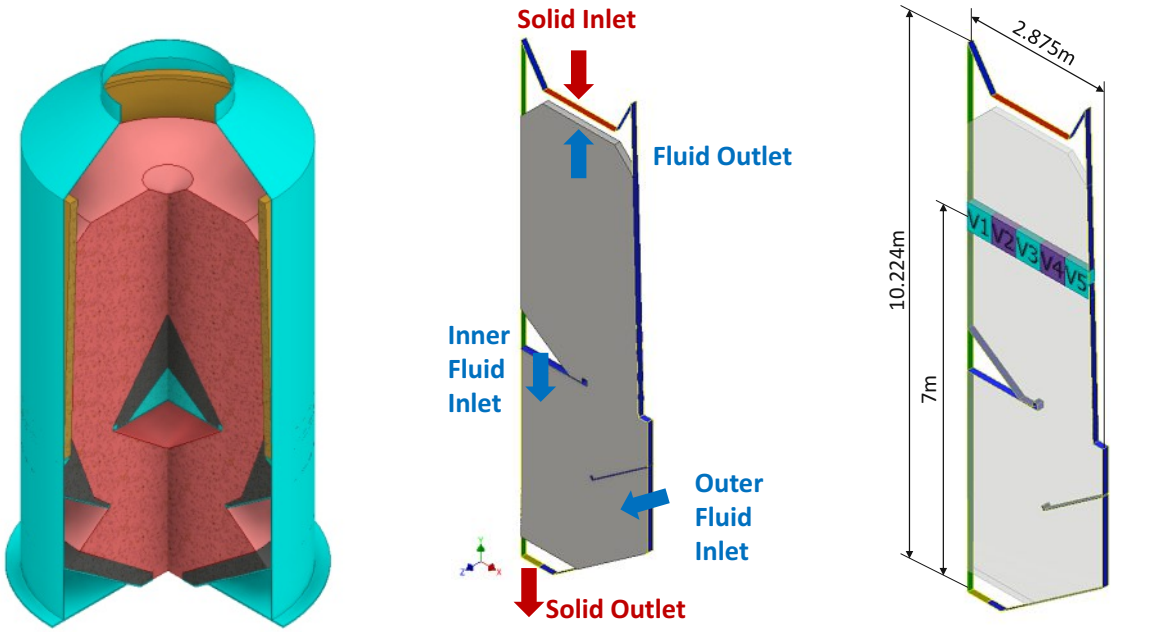

(a) 3D-geometry

(b) Quasi-axisymmetric geometry

(c) Control volumes for segregation analysis and main dimensions

Figure 10.1.: Shaft cooler geometry.

in momentum and energy source terms. The problematic regions are excluded from the CFD domain as a workaround.

10.2. Particle-Size Distribution (PSD)

The particle-size distribution according to Table 10.1 is obtained from sieve analyses. As mentioned above, this distribution yields a huge number of particles in the computational domain. The maximum coarse-graining factor is limited by the characteristic length in the system. As a workaround, the particle-size distribution is truncated, i. e. the large particles are not considered in the simulation, and higher coarse-graining factors can be applied. The mass fractions of the remaining particles are scaled up so that their sum is again equal to one. Both the truncation of the particle-size distribution and coarse-graining of particles can influence the particulate flow behavior. Investigations have to be performed to ensure that this impact is within an acceptable extent.

The examined particle-size distributions for the quasi-axisymmetric geometry are summarized in Table 10.2. The corresponding coarse-graining factors are quoted as well as the resulting

Die approbierte gedruckte Originalversion dieser Diplomarbeit ist an der TU Wien Bibliothek verfügbar
The approved original version of this thesis is available in print at TU Wien Bibliothek.

Table 10.1.: Particle-size distribution based on mass and numbers.

	Diameter [mm]	Mass-percent [%]	Number-percent [%]
d_1	2.5	25	96.6645
d_2	7.5	18	2.5777
d_3	12.5	20	0.6187
d_4	17.5	9	0.1015
d_5	30	13.5	0.0302
d_6	45	9.5	0.0063
d_7	65	5	0.0011

number of particles in the simulation domain. The different particle-size distributions are entitled according to the capital letter in the second column.

10.3. Solid Material Properties

The LIGGGHTS-PUBLIC version does not support temperature dependent material properties, see 5.2. However, often it is not desired to consider temperature dependent properties since it adds further complexity to the system. In most cases simpler simulation setups are preferred as a starting point, because problems connected with the software (bugs) or configuration issues, such as wrong choice of boundary conditions, can be identified more easily. The choice of solid material parameters in this work is summarized in the following.

The composition of the sinter is given in Table 10.3. The values for density, Young's modulus and Poisson's ratio in Table 10.4 and the coefficients of restitution, sliding-friction and rolling-friction for particle-particle and particle-wall interaction in Table 10.5 are taken from [61]. The coefficient of rolling viscous damping is determined by the angle of repose test, see 11.1. The quantities for particle-symmetry axis interaction are identified by the discharging test, see 11.2.

Table 10.2.: Truncated particle-size distributions used for the DEM and coupled DEM-CFD simulations with the corresponding coarse-graining factor and the number of particles.

Particle sizes	PSD	DEM	DEM-CFD	Cg-factor	Number of particles
1	—	✗	✗	—	—
2	A	✗	✓	16	30k
3	B	✓	✓	10	90k
4	C	✓	✗	8	170k
5	D	✓	✗	7	300k
6	—	✗	✗	—	—
7	—	✗	✗	—	—

Die approbierte gedruckte Originalversion dieser Diplomarbeit ist an der TU Wien Bibliothek verfügbar
The approved original version of this thesis is available in print at TU Wien Bibliothek.

Table 10.3.: Composition of the sinter material in mass-percent, dry analysis.

Fe_2O_3	FeO	Fe	CaO	MgO	Al_2O_3	SiO_2
74.30	8.50	2.90	6.79	1.80	2.14	3.57

The values for thermal conductivity and thermal capacity are obtained by the mean of the polynomial function with dependency on the temperature, see C.1. The temperature ranges from 30 °C to 500 °C.

Coupled DEM-CFD simulations are transient by nature. Beside the fact that in many industrial processes a problem in terms of length scale between geometry and particle size persists, also the difference in time-scales can be problematic. On the one hand, a very small time-step is needed to resolve particle contacts in soft-particle DEM, see 3.2.2. On the other hand, many industrial process involve rather large time-scales. To cope with this discrepancy, a time-scaling approach as explained in 4.2.4 is applied and a correction factor according to 6.6 is introduced. From this it follows that the thermal capacity in Table 10.4 needs to be adjusted with regard to the chosen time-scaling factor.

In 4, further methods to speed up DEM simulations are discussed, such as density-scaling or reduction of the Young's modulus, but these are not utilized in this work. For the latter the reason is that the softer particles would cause higher overlap and consequently more particles in the computational domain. Furthermore, a reduced Young's modulus leads to stronger oscillation effects due to filling and discharging of particles.

10.4. Fluid Material Properties

The fluid material properties are summarized in Table 10.6. The reference kinematic viscosity and the thermal diffusivity are calculated according to (6.10) and (6.22) respectively. The values for the dynamic viscosity, thermal conductivity and thermal capacity are obtained by the mean

Table 10.4.: Material properties of the particles (p), the walls (w) and the symmetry axis (s).

Property	Symbol	Dimension	p	w	s
Density	ρ_s	$[\mathrm{kg/m^3}]$	2284	—	—
Young's modulus	E	$[\mathrm{N/m^2}]$	3.0×10^8	2.0×10^8	2.0×10^8
Poisson's ratio	ν_{Po}	$[-]$	0.4	0.4	0.4
Thermal conductivity	λ_s	$[\mathrm{W/(m\,K)}]$	0.082	0.082	0.082
Solid thermal capacity	c_s	$[\mathrm{J/(kg\,K)}]$	834	834	834

Die approbierte gedruckte Originalversion dieser Diplomarbeit ist an der TU Wien Bibliothek verfügbar
The approved original version of this thesis is available in print at TU Wien Bibliothek.

Table 10.5.: Material parameters of the Hertz contact model and the EPSD rolling-friction model for particle-particle (p-p), particle-wall (p-w) and particle-symmetry axis (p-s) interaction.

Property	Symbol	Dimension	p-p	p-w	p-s
Coeff. of restitution	e	[−]	0.2	0.2	0.2
Coeff. of sliding-friction	μ_s	[−]	0.91	0.65	0
Coeff. of rolling-friction	μ_r	[−]	0.35	0.25	0
Coeff. of rolling visc. damping	η_r	[−]	0.35	0.25	0

of the polynomial function with dependency on the temperature, see C.2. The temperature ranges from 30 °C to 500 °C.

10.5. Boundary Conditions

The boundary conditions, which remain unchanged for all simulation cases, are summarized in Table 10.7. The other boundary conditions such as truncated particle-size distribution, air inlet velocity or number of air inlets are specified in the respective section.

The coupled DEM-CFD solver is very sensible with regard to stability. The reason is the coupling of DEM and CFD simulation and the consideration of density changes due to temperate. Therefore, a ramp for the temperature dependent boundary conditions is employed to provide better stability of the solution process.

10.5.1. Turbulent Boundary Conditions

The Reynolds-averaged Navier-Stokes equations in conjuction with the incompressible realizable k-ε model are used to account for turbulence. The default turbulence model coefficients are retained, see Table 10.8. Different turbulence models and their application as well as formulations

Table 10.6.: Fluid material properties for dry air.

Property	Symbol	Value and dimension
Dynamic viscosity	μ_f	$28.236 \times 10^{-5}\,\mathrm{Pa\,s}$
Thermal conductivity	λ_f	$4.2 \times 10^{-2}\,\mathrm{W/(m\,K)}$
Thermal capacity	$c_{p,f}$	$1041.5\,\mathrm{J/(kg\,K)}$
Reference temperature	T_{ref}	$303.15\,\mathrm{K}$
Reference density	ρ_{ref}	$1.149\,\mathrm{kg/m^3}$
Reference kinematic viscosity	ν_{ref}	$24.575 \times 10^{-6}\,\mathrm{m^2/s}$
Reference thermal diffusivity	$D_{T,ref}$	$35.097 \times 10^{-6}\,\mathrm{m^2/s}$

Die approbierte gedruckte Originalversion dieser Diplomarbeit ist an der TU Wien Bibliothek verfügbar
The approved original version of this thesis is available in print at TU Wien Bibliothek.

Table 10.7.: Boundary conditions for the coupled DEM-CFD simulation.

Property	Symbol	Value and dimension
Solid mass flow	$\dot{m}_s$	50 t/h
Solid inlet temperature	$T_{s,in}$	500 °C
Air inlet temperature	$T_{f,in}$	30 °C
Turbulent intensity	I_{turb}	1 %
Turbulent length scale at Inlet 1	$l_{turb,1}$	0.119 m
Turbulent length scale at Inlet 2	$l_{turb,2}$	0.077 m

are for example discussed in [62]. The turbulent boundary conditions can be estimated with the formulas mentioned in the following. A guideline can be found in [55]. The turbulent intensity can be calculated as a function of the inlet Reynolds number Re_L according to

$$I_{turb} = 0.16\, Re_L^{-1/8}\,. \tag{10.1}$$

The turbulent length scale can be estimated as follows

$$l_{turb} = 0.07\, L_{in}\,, \tag{10.2}$$

with the characteristic dimension of the inlet L_{in}.

10.6. Time-Step Settings

Both the DEM and the CFD time-step can be displayed and checked by the corresponding simulation software during a simulation run. Estimation rules for the DEM time-step are given in 3.2.2. A guideline for the choice of the CFD time-step is given in below. The coarse-graining factor has an impact on the DEM time-step because it depends on the size of the particles in the simulation domain. The selected time-step sizes and the coupling interval are summarized in Table 10.9.

Table 10.8.: Default turbulence model coefficients of the incompressible realizable k-ε model in OpenFOAM.

C_μ	A_0	C_2	σ_k	σ_ε
0.09	4	1.9	1	1.2

Die approbierte gedruckte Originalversion dieser Diplomarbeit ist an der TU Wien Bibliothek verfügbar
The approved original version of this thesis is available in print at TU Wien Bibliothek.

Table 10.9.: Selected time-step sizes for the DEM, CFD and coupled DEM-CFD simlation with regard to the employed particle-size distribution and the resulting fraction of the Rayleigh-time $\Delta t/t_R$ and Hertz-time $\Delta t/t_H$.

PSD [−]	Δt_{DEM} [s]	Δt_{CFD} [s]	$\Delta t_{DEM-CFD}$ [s]	$\Delta t/t_R$ [−]	$\Delta t/t_H$ [−]
A	0.00004	0.0004	0.004	0.13	0.05
B	0.00004	0.0004	0.004	0.21	0.11
C	0.00003	—	—	0.20	0.08
D	0.000025	—	—	0.19	0.08

10.6.1. CFL condition

The choice of the time-step for transient CFD simulations is essential to ensure numerical stability. The Courant–Friedrichs–Lewy (CFL) condition can be used to estimate an appropriate time-step size. It is defined as follows

$$\sigma = \frac{u_f \Delta t}{\Delta x} \leq \sigma_{max} \,, \tag{10.3}$$

where σ is the Courant number, u_f the fluid velocity, Δt the time-step size and Δx the characteristic length (smallest cell size of the CFD mesh). The maximum Courant number σ_{max} depends on the time discretization method used. It is usually equal to one for explicit schemes. In this case, the CFL condition can interpreted as the condition, that the fluid with the velocity u_f must not cover a distance which is bigger than the smallest cell size Δx within one time-step Δt. If an implicit scheme is utilized, Courant numbers bigger than one can be used to estimate the time-step size.

The actual CFD time-step size applied in the coupled DEM-CFD simulation is chosen significantly smaller than the estimated value by (10.3) to ensure a stable run of the coupled solver, see Table 10.9. The resulting Courant numbers are in the order of magnitude of around 0.1.

10.7. CFD Mesh

As mentioned in 6.2.1, the unresolved DEM-CFD coupling approach presumes that the particles are significantly smaller than the cell size of the CFD mesh. In practice this assumption can be problematic, e. g. if a particle-size distribution is used and a high coarse-graining factor is applied. Advanced void fraction models are available in CFDEMcoupling to overcome this issue. The largest particle size of PSD-B is compared to the mesh cell size in Figure 10.2 (b). In the most cases, the particles are smaller than the cells. But in some regions the mesh size is constrained by the geometry and the particles are slightly bigger than the cells. Thus, the

Die approbierte gedruckte Originalversion dieser Diplomarbeit ist an der TU Wien Bibliothek verfügbar
The approved original version of this thesis is available in print at TU Wien Bibliothek.

Divided Void Fraction model is employed, which is using satellite points to divide the volume of particles to touched cells instead of only considering the center of mass. This procedure enables particle diameters to be in order of the cell size of the CFD mesh [41].

The entire mesh is pictured in Figure 10.2 (a). The cell size is constrained by the geometry, i. e. the smallest details that are resolved. The generated structured mesh consists of 970 hexahedral cells and it features a thickness of one cell in the z-direction. The boundary layer of the fluid flow at the walls is not resolved, instead wall functions are employed.

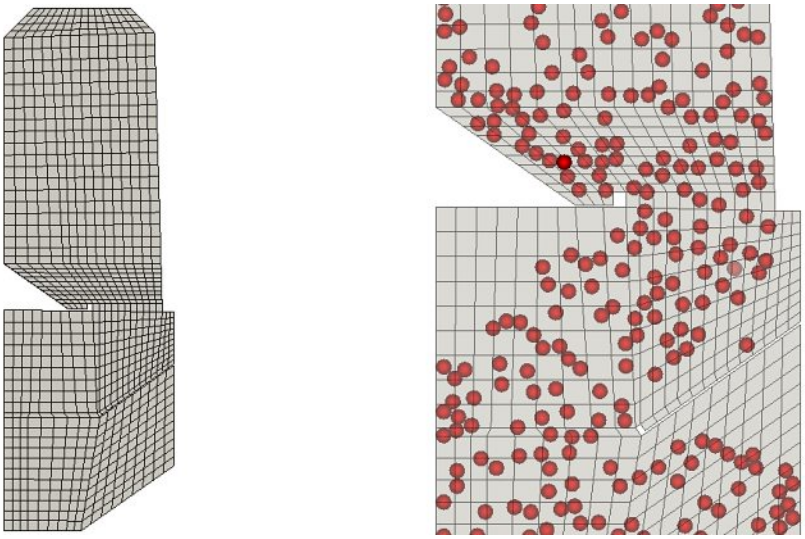

(a) CFD mesh

(b) Comparison of cell and particle size (detailed view)

Figure 10.2.: Hexahedral CFD mesh and detailed view of the mesh cell size compared to the largest particle size of PSD-B.

Die approbierte gedruckte Originalversion dieser Diplomarbeit ist an der TU Wien Bibliothek verfügbar
The approved original version of this thesis is available in print at TU Wien Bibliothek.

11. DEM Simulation Results

The objectives of the DEM simulation are summarized in 8.1. The solid flow is examined without consideration of the interstitial fluid. This kind of flow is sometimes referred to as dry granular flow. Moreover, the particle temperature and conductive heat transfer in the solid phase is neglected.

11.1. Angle of Repose Test

Three rolling-friction models are investigated with regard to the angle of repose for the truncated particle-size distribution B without coarse-graining. In LIGGGHTS these models are named CDT (constant directional torque) model, EPSD (elastic-plastic spring-dashpot) model and EPSD2 model. The latter one is in principal the EPSD model without consideration of the viscous damping torque. The advantages and disadvantages of the different rolling-friction models and the formulations for the EPSD model are discussed in 3.4.

In the angle of repose test case, particles are poured onto a flat plane. The particles settle under the influence of gravity and the resulting angle of repose is compared to experimental results. The angle of repose for the given material obtained by the experiments is equal to 38°.

As mentioned in 10.3, the coefficient of rolling viscous damping for the EPSD rolling-friction model is not provided in [61]. The angle of repose test case is used to calibrate the EPSD model to match the experimental results. A value of 0.35 for particle-particle contact and 0.25 for particle-wall contact was found to give good results compared to the experiment, see also Table 10.5.

The simulation results for the test case are depicted in Figure 11.1. As explained in 3.4.1, the CDT model shows creep-like behavior and the established pile of particles collapses slowly, thus the angle of repose is smaller compared to the other models. Both the EPSD and the EPSD2 model produce results close to 38°. Nevertheless, the angle resulting from the EPSD2 model is slightly smaller, which might be because it also shows creep-like behavior due to negligence of the viscous damping term. If the simulation time is extended and the particles are allowed to rest longer, the pile might collapse further.

The angle of repose test case is performed without coarse-graining of the particles. As explained in 2.1.1, frictional surface forces are responsible for the establishment of particle piles. These surfaces forces depend on the surface-to-volume ratio, which is affected by coarse-graining of particles. Therefore, tests for every coarse-graining factor utilized in the simulations or a correction factor in the rolling-friction model to account for the scaling of particles would be needed to guarantee reliable results.

Die approbierte gedruckte Originalversion dieser Diplomarbeit ist an der TU Wien Bibliothek verfügbar
The approved original version of this thesis is available in print at TU Wien Bibliothek.

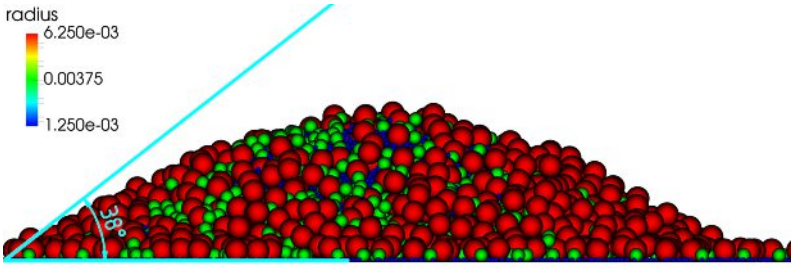

(a) CDT model

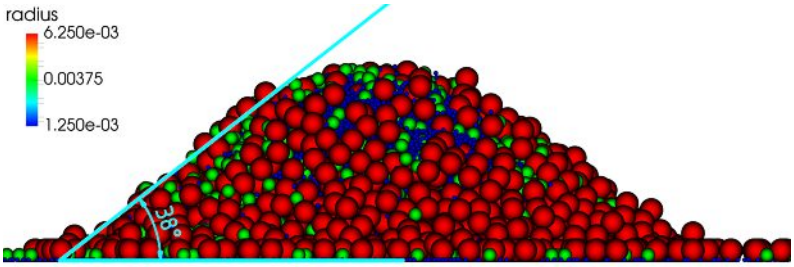

(b) EPSD model

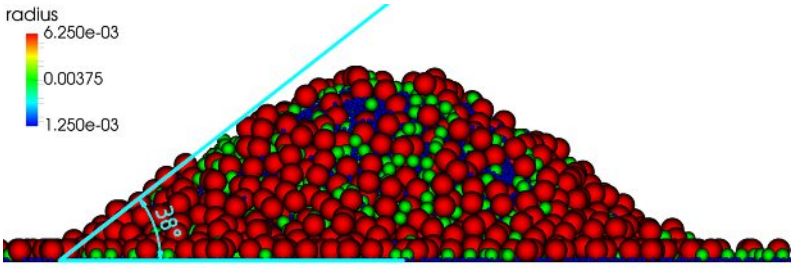

(c) EPSD2 model

Figure 11.1.: Comparison of rolling-friction models with regard to the angle of repose on a flat plane.

11.2. Discharging Test

As described in 10.1, the sinter cooler is reduced to a quasi-axisymmetric geometry in the simulation and the symmetry axis is modeled as wall. To minimize the influence of the symmetry axis on the simulation results, the friction parameters are determined by a discharging test. The quasi-axisymmetric geometry in Figure 10.1 (b) and a symmetric geometry are compared. The symmetric geometry is composed of the axisymmetric geometry and its mirrored counterpart and the symmetry axis is removed. Both geometries are filled up with particles, see Figure 11.2. Then the outlet at the bottom is opened and the particles are discharged. The truncated particle-size distribution B is used for this test case. The number of particles for the completely filled quasi-axisymmetric geometry amounts to 86178, while the symmetric geometry contains 172550 particles. This yields a relative difference of 0.11 % considering twice the amount of particles for

Die approbierte gedruckte Originalversion dieser Diplomarbeit ist an der TU Wien Bibliothek verfügbar
The approved original version of this thesis is available in print at TU Wien Bibliothek.

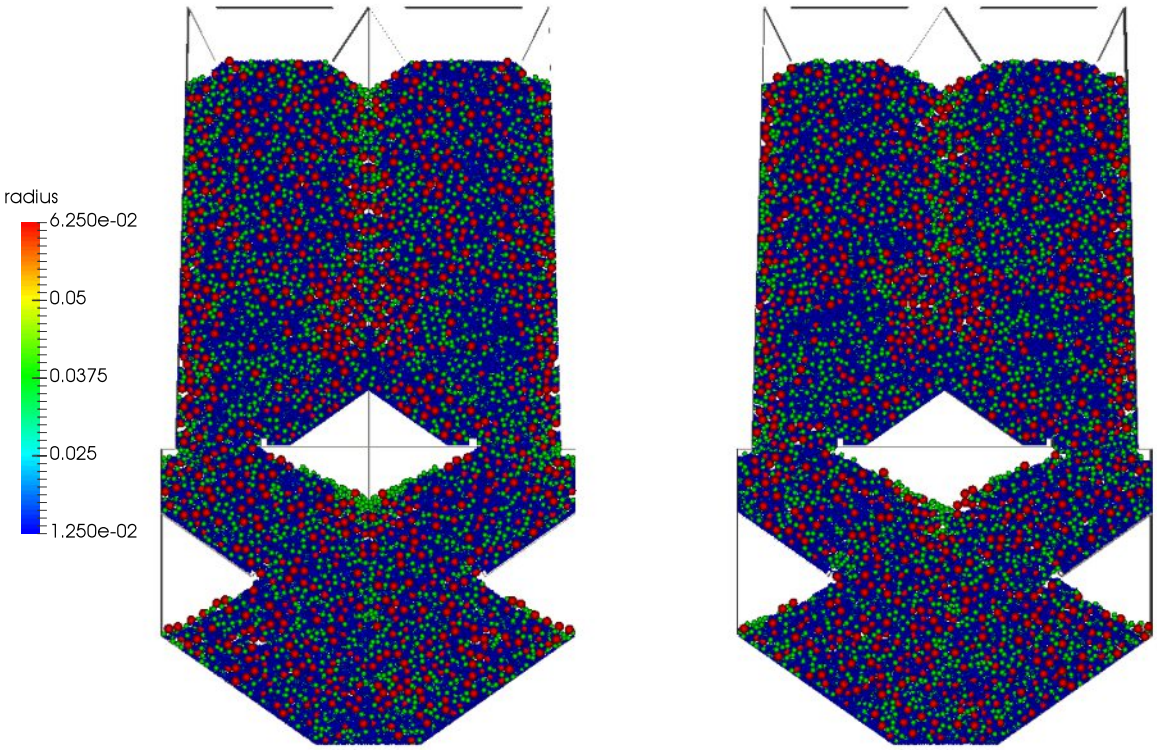

Figure 11.2.: Comparison of the mirrored quasi-axisymmetric geometry (left) and the symmetric geometry (right), both filled up with particles.

the quasi-axisymmetric case. For a meaningful comparison of the two simulations, the number of particles in the computational domain is normalized and plotted along the simulation time.

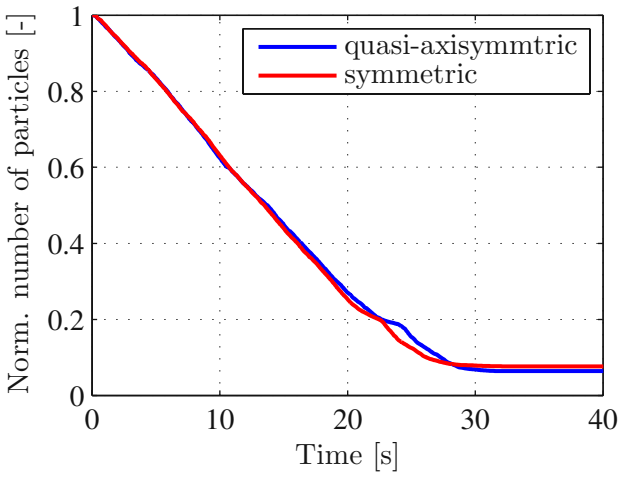

Figure 11.3.: Comparison of the normalized number of particles inside the shaft cooler during the discharging test.

Die approbierte gedruckte Originalversion dieser Diplomarbeit ist an der TU Wien Bibliothek verfügbar
The approved original version of this thesis is available in print at TU Wien Bibliothek.

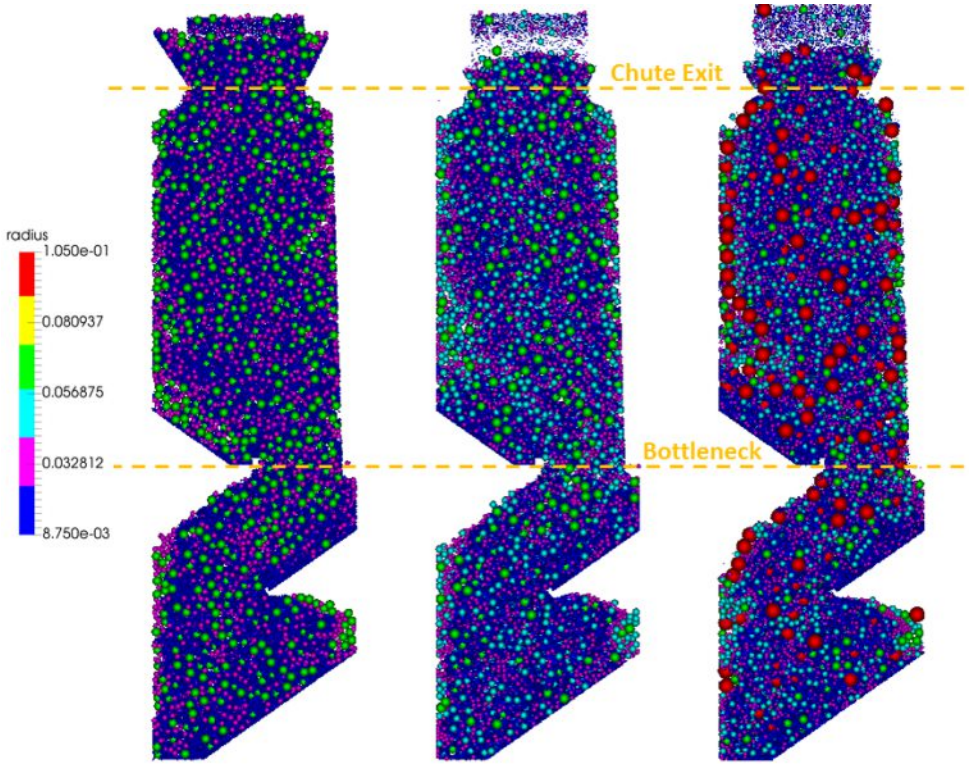

Figure 11.4.: Snapshot of segregated particle flows for PSD-B (left), PSD-C (middle) and PSD-D (right) with indication of the supply chute exit and the geometrical bottleneck.

Good results are achieved if the coefficients for sliding and rolling-friction and rolling viscous damping are set to zero for the symmetry axis. The plot in Figure 11.3 shows similar progression of the number of particles inside the cooler and good agreement of the discharging time. However, the number of particles that remain inside the cooler, e. g. in dead zones, differs slightly.

11.3. Segregation Analysis

Segregation effects occur due to different phenomena, see 2.1.1. These non-trivial features are not always easy to predict, thus a DEM simulation is used to investigate segregation in the shaft cooler. At a height of 7 m, five equally sized control volumes are created to analyze segregation due to charging of the sinter cooler. The control volumes are depicted in Figure 10.1 (c). At this height segregation is expected to occur mainly as a result of larger particles rolling down on the already established pile when exiting the supply chute.

In Figure 11.5 (a) to (c) the time-averaged discrete data from the DEM simulation for the truncated particle-size distributions B, C and D are analyzed. A comparison of these figures reveals that the mass fraction of the smallest particles is relatively high in the inner control

Die approbierte gedruckte Originalversion dieser Diplomarbeit ist an der TU Wien Bibliothek verfügbar
The approved original version of this thesis is available in print at TU Wien Bibliothek.

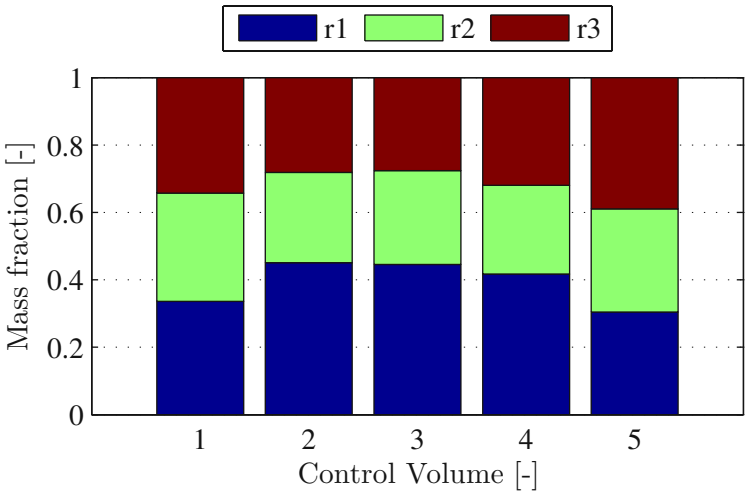

(a) Particle-size distribution B

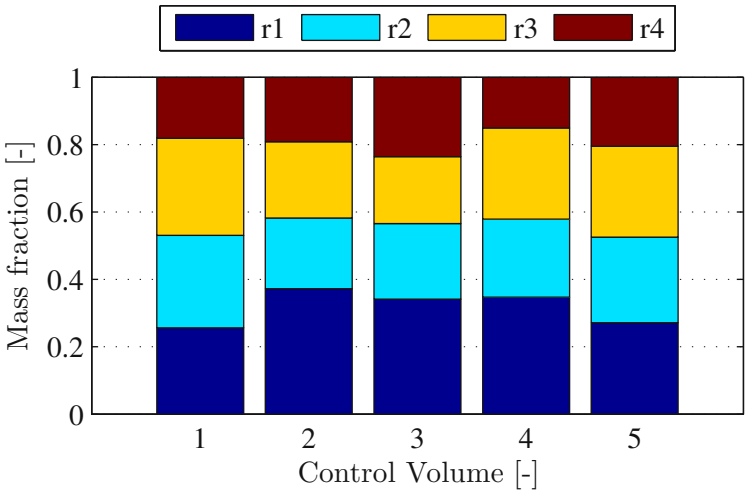

(b) Particle-size distribution C

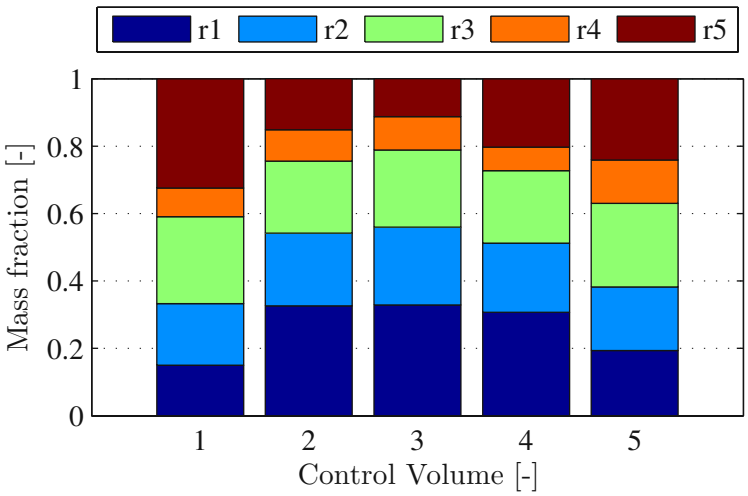

(c) Particle-size distribution D

Figure 11.5.: Time-averaged segregation analysis for the truncated particle-size distributions.

Die approbierte gedruckte Originalversion dieser Diplomarbeit ist an der TU Wien Bibliothek verfügbar
The approved original version of this thesis is available in print at TU Wien Bibliothek.

volumes (2, 3, 4), whereas the larger particles tend to gather in the outer volumes (1, 5). This behavior resembles the expectations. However, on closer inspection of Figure 11.5 (b) it can be noticed that the distribution of the larger particles deviates from the other particle-size distributions. This might be due to the discrete nature of DEM simulations or the randomness of the insertion method. Another reason might be the effect of other segregation phenomena such as percolation or influence on the trajectory, see 2.1.1.

A snapshot of the segregated particle flows is presented in Figure 11.4. The exit of the supply chute is highlighted to indicate the place where segregation due to the charging process occurs. Furthermore, the bottleneck of the cooler geometry is pointed out. There segregation occurs once again because larger particles are rolling down on an established particle pile.

11.4. Dead Zones

The Lagrangian point data from the DEM simulations is converted into an Eulerian frame of reference by mapping the particle data onto a mesh and calculation of the cell-average. The contour plot of the solid velocity is used to identify dead zones and zones with lower velocity magnitude. The velocity range is rescaled to emphasize differences.

For all simulated particle-size distribution (B, C, D), three zones are highlighted in Figure 11.6. Region (1) cannot be referred to as a dead zone. A time-scaling and coarse-graining approach is employed in the simulations to speed up the computation time significantly. Thus, the artificially increased solid velocity might influence the formation of dead zones in this region. Furthermore, the drastically increased particle size might disadvantage the pile up of particles due to the relation of the particle size and the characteristic length scale of the geometry. The modified surface-to-volume ratio and its impact on the angle of repose could prevent the establishment of a particle pile on the sheet metal. However, a zone with lower velocity magnitude is identified. This is also confirmed by the deflection of the particle trajectory through the sinter cooler, see Figure 11.7. For lower coarse-graining factors applied in the simulation (PSD-C and PSD-D) this zone is pronounced more. In region (2) and (3) dead zones evolve from geometrical conditions for all truncated particle-size distributions tested.

The velocity peak at the top of the sinter cooler is due to the insertion method of the DEM simulation. The insertion velocity has to be raised with increasing particle size, but the higher kinetic energy of the particles is absorbed by the supply chute which is modeled as a hopper. In the middle of the cooler the particles are sped up because of the geometrical bottleneck. The hot spot indicates particles rolling down on the top of the bulk flow. The high velocity at the bottom is caused by the discharging method of the sinter cooler.

Die approbierte gedruckte Originalversion dieser Diplomarbeit ist an der TU Wien Bibliothek verfügbar
The approved original version of this thesis is available in print at TU Wien Bibliothek.

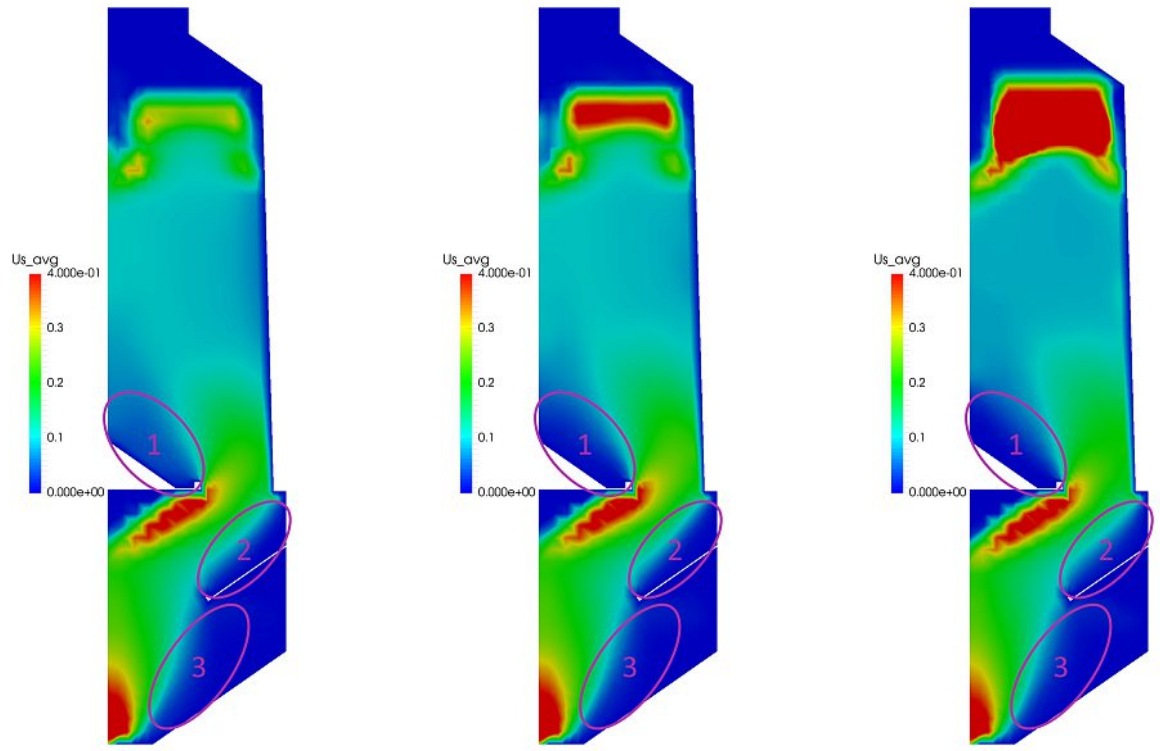

(a) PSD-B (b) PSD-C (c) PSD-D

Figure 11.6.: Solid velocity contour plot with a region of low velocity magnitude (1) and two dead zones (2) and (3).

11.5. Particle Trajectories

The trajectory of different particle sizes and inlet positions is investigated. The particles are released close to the symmetry axis (inside), at the center of the quasi-axisymmetric geometry (center), or close to the outer wall (outside). The path is tracked while the sinter is being transported through the cooler, see Figure 11.7. The bulk particles are colored according to their particle ID in the simulation, i. e. blue are the particles that are in the cooler since longer time and red are the ones recently added to the computational domain.

For each particle-size distribution, three particles are released simultaneously at different positions. The particles on the inside and the center move significantly faster through the shaft cooler. The outer particles did not reach the outlet of the sinter cooler within the simulated real-time of 420 min. The through-put time of the traced particles at the inside and the center is presented in Table 11.1. This data is in good agreement with the estimated average through-put time of 265 min calculated by the Excel-tool. As pointed out in 9, the simulation domain in

Die approbierte gedruckte Originalversion dieser Diplomarbeit ist an der TU Wien Bibliothek verfügbar
The approved original version of this thesis is available in print at TU Wien Bibliothek.

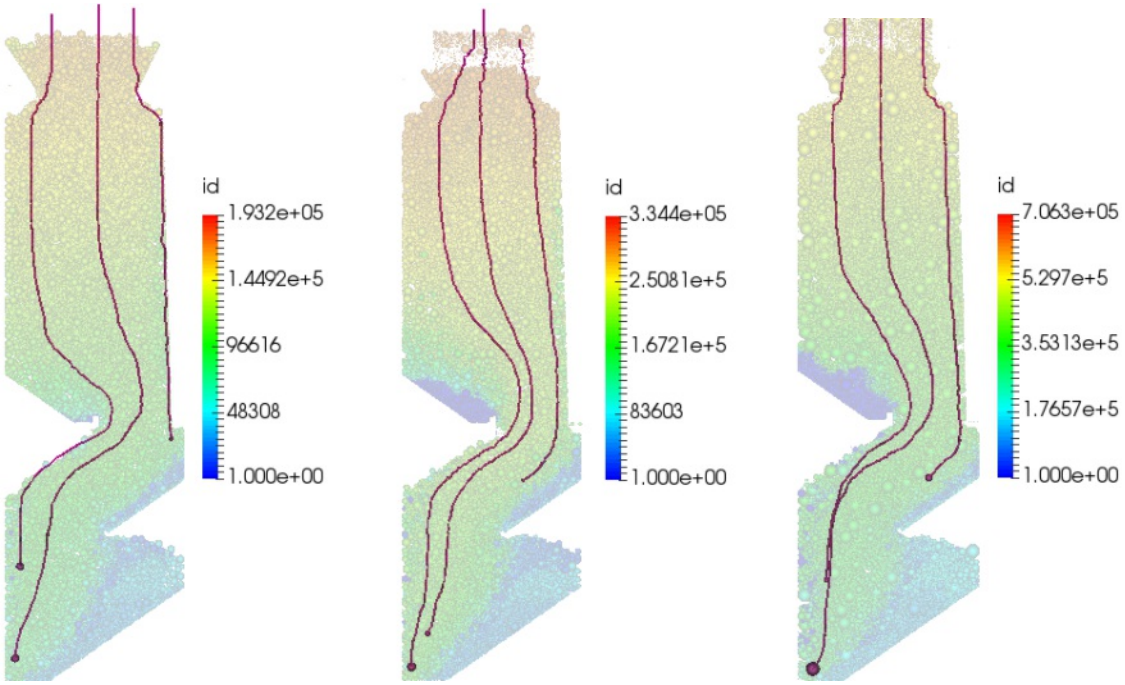

(a) PSD-B (b) PSD-C (c) PSD-D

Figure 11.7.: Particle trajectories for different particle-size distributions (in magenta) and particle ID (transparent).

Excel is truncated and no dead zones are depicted due to the use of a continuum model. These two effects counteract on each other if the through-put time of the fast particles is considered.

A dependency on the particle size is detected in addition to the influence of the insertion position. The particle-size ratio with respect to the smallest particle of the simulated particle-size distribution is given in brackets in Table 11.1. The particle-size ratio in conjunction with the through-put time suggests that larger particles are transported faster than smaller ones. This might be due to the higher surface-to-volume ratio of smaller particles, which slows them down more efficiently due to frictional forces, see 2.1.1 (Trajectory).

It has to be underlined that particular discrete particles are used for the conclusions above. This data is not necessarily representative for all other particles, but it can be used to examine and understand the basic phenomena of the solid flow in the shaft cooler. To obtain more significant data, a higher number of particles have to be investigated with regard to the insertion position and the particle size. Subsequently more meaningful averaged values could be calculated.

Die approbierte gedruckte Originalversion dieser Diplomarbeit ist an der TU Wien Bibliothek verfügbar
The approved original version of this thesis is available in print at TU Wien Bibliothek.

Table 11.1.: Through-put time of selected particles in minutes. The particle-size ratio with respect to the smallest particle of the PSD is specified in brackets.

	PSD-B	PSD-C	PSD-D
center	265 (5)	275 (5)	256 (12)
inside	283 (5)	265 (7)	273 (7)

Die approbierte gedruckte Originalversion dieser Diplomarbeit ist an der TU Wien Bibliothek verfügbar
The approved original version of this thesis is available in print at TU Wien Bibliothek.

12. Coupled DEM-CFD Simulation Results

The objectives of the coupled DEM-CFD simulation are specified in 8.2. According to Table 10.2, two truncated particle-size distributions are simulated, but PSD-A is mainly used for test purposes because of its significant lower computation time. However, the results could also be used for evaluation of the coarse-graining influence on the simulation outcome.

As mentioned in 10.5, the coupled simulations are started with ramp boundary conditions due to stability issues. Subsequently the simulation is continued until a steady-state solution is obtained.

12.1. Verification of the Simulation Results

The validation of simulation results is generally a crucial step. Usually experiments are used to validate numerical solutions and solver implementations. Unfortunately experimental results are not available for the present problem. Therefore, several verification cases for the solver modifications are performed in 7. It is also desirable to verify that the chosen boundary conditions and simulation setup give reasonable results.

As explained in 9, a simulation code in Excel-VBA is available for the sinter cooler facility. The Excel-tool is derived from simulation tools which are well-proven for similar industrial applications. Therefore, it is suitable for the assessment whether the coupled DEM-CFD simulation gives reasonable results. Nevertheless, there are some obstacles that have to be considered if these two different simulation tools are compared. An overview is given in Table 12.1.

12.1.1. Critical Review of the Quasi-Axisymmetric Representation

The DEM software LIGGGHTS does not support axisymmetric geometries, therefore the sinter cooler is modeled in a quasi-axisymmetric manner, see 5.2 and 10.1. The three-dimensional geometry is transformed into a quasi-axisymmetric representation by extrusion of the axially symmetric cross-section area. Thus, the area-ratio of the inlets and outlets is not constant. This discrepancy is illustrated by means of the overall mass balance of the sinter cooler, which can be written as follows

$$\dot{m}_{s,in} + \dot{m}_{f,in} = \dot{m}_{s,out} + \dot{m}_{f,out} \,, \tag{12.1}$$

Die approbierte gedruckte Originalversion dieser Diplomarbeit ist an der TU Wien Bibliothek verfügbar
The approved original version of this thesis is available in print at TU Wien Bibliothek.

Table 12.1.: Differences between the Excel-tool and the coupled DEM-CFD simulation.

	Excel-Tool	Coupled DEM-CFD Simulation
Particle model	continuum	discrete
Particle-size distribution	entire PSD	truncated PSD
Void fraction	constant input value	obtained from the simulation
Segregation	no	yes
Dead zones	no	yes
Time-scaling	no	yes
Coarse-graining	no	yes
Time-dependency	stationary	transient
Fluid inlet BC	pressure	velocity
Solid outlet BC	entire bottom face	section of the bottom face
Geometry (height)	truncated	entire geometry
Symmetry	axisymmetric	quasi-axisymmetric
Wall-influence on solid flow	no	yes

with the solid mass flow $\dot{m}_s$ and the fluid mass flow $\dot{m}_f$ at the corresponding inlet and outlet. If a quasi-axisymmetric instead of the three-dimensional geometry is examined, only the equivalent fraction of the mass flow has to be considered by the relation

$$K_i = \frac{\dot{m}_i}{\dot{m}'_i} = \frac{A_i}{A'_i}\,, \tag{12.2}$$

where the mass flow $\dot{m}_i$ and the surface are A_i are denoted with prime in the quasi-axisymmetric representation and without prime in the three-dimensional case. The quantity K_i is referred to as area-ratio. A combination of (12.1) and (12.2) gives

$$\dot{m}'_{s,in}\,K_{s,in} + \dot{m}'_{f,in}\,K_{f,in} = \dot{m}'_{s,out}\,K_{s,out} + \dot{m}'_{f,out}\,K_{f,out}\,. \tag{12.3}$$

Only in case of a two-dimensional geometry the area-ratio is equal for all inlets and outlets and can be canceled out in (12.3). For the quasi-axisymmetric case, a correction factor accounting for the varying area-ratio has to be considered. If the solid inlet mass flow is chosen as reference value, the mass balance can be expressed as

$$\dot{m}'_{s,in} + \dot{m}'_{f,in}\,\frac{K_{f,in}}{K_{s,in}} = \dot{m}'_{s,out}\,\frac{K_{s,out}}{K_{s,in}} + \dot{m}'_{f,out}\,\frac{K_{f,out}}{K_{s,in}}\,. \tag{12.4}$$

In general, the mass flow can be written as $\dot{m} = \rho\,u\,A$. Both fluid and solid density as well as the surface areas are preset in the simulation. From this it follows that the area-ratio effects the resulting velocities. This means the simulation results for the quasi-axisymmetric geometry

Die approbierte gedruckte Originalversion dieser Diplomarbeit ist an der TU Wien Bibliothek verfügbar
The approved original version of this thesis is available in print at TU Wien Bibliothek.

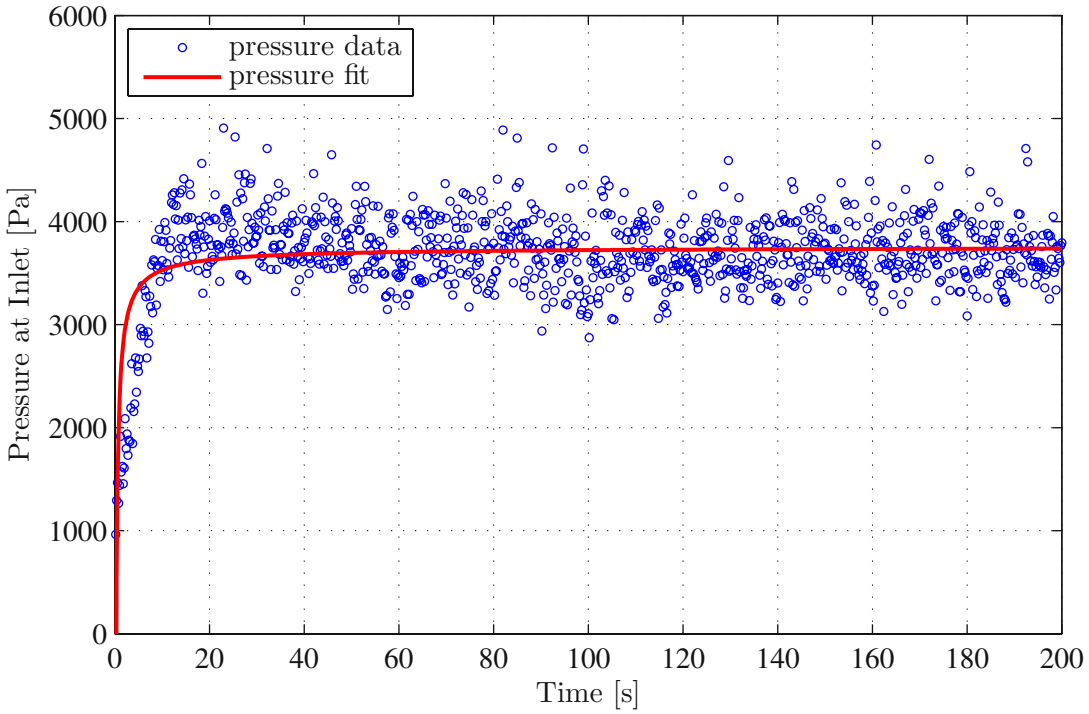

Figure 12.1.: Progression of the pressure drop across the sinter bed in the shaft cooler for a velocity boundary condition of 0.25 m/s at the outer air inlet.

have to be reviewed critically with regard to the velocities and other dependent quantities such as pressure drop.

12.1.2. Excel-Tool vs. DEM-CFD Simulation

In the following, the coupled DEM-CFD simulation is compared to the results of the Excel-tool. Most of the settings for the simulation such as material properties or boundary conditions are specified in 10 and are valid for both calculations. Due to restrictions of the Excel-tool, only the outer fluid inlet is considered, see Figure 10.1.

A velocity boundary condition of 0.25 m/s normal to the surface is set for the DEM-CFD simulation. The pressure drop is monitored and plotted in Figure 12.1. The fluctuations are due to the discrete nature of the Discrete Element Method, i. e. the results for coupled DEM-CFD simulations are usually noisy. The average pressure drop is obtained by a fit of the data and amounts to 3738 Pa. This value is used as a boundary condition for the Excel simulation. An appropriate region to compare the velocity field is between the bottleneck of the geometry and the fluid outlet, i. e. at an altitude range of 5 m to 7 m. Furthermore, the outcome of the DEM-CFD simulation is corrected with respect to the area-ratio of the outer fluid inlet according to (12.4).

Die approbierte gedruckte Originalversion dieser Diplomarbeit ist an der TU Wien Bibliothek verfügbar
The approved original version of this thesis is available in print at TU Wien Bibliothek.

Table 12.2.: Comparison of the simulation results for one fluid inlet (pressure drop Δp, average velocity $\bar{v}$ at an altitude range of 5 m to 7 m, inlet standard volume flow $\dot{V}_{in}^{n}$ and solid outlet mean temperature $\bar{T}_{s,out}$).

	DEM-CFD	Corrected DEM-CFD	Excel-forward	Excel-backward
Δp [Pa]	3738	3738	3738	2600
$\bar{v}$ [m/s]	0.96	0.44	0.53	0.41
$\dot{V}_{in}^{n}$ [Nm^3/h]	24452	11186	15076	11689
$\bar{T}_{s,out}$ [°C]	337	337	287	337

A reverse-calculation in the Excel-tool is performed to match the solid outlet mean temperature of the DEM-CFD simulation. The results are summarized in Table 12.2.

The following conclusions are drawn for the quasi-axisymmetric DEM-CFD simulations on the basis of the results in Table 12.2:

- For a given solid mass flow, the fluid inlet velocity boundary condition has to be corrected according to the area-ratios to match the actual relation between solid and fluid mass flow (also valid for two fluid inlets).
- The solid outlet temperature gives reasonable results in consideration of the solid-fluid mass flow ratio, while the pressure drop is overestimated due to the use of a quasi-axisymmetric geometry and a time-scaling approach, see 4.2.4 and 6.6. Since the pressure drop is a quadratic function of the velocity according to(6.13), introduction of a correction factor is not straight-forward.
- The comparison of the results with the Excel-tool has to be observed with caution due to numerous model-assumptions and their consequences on the simulation outcome.
- No validation for the Excel-tool was performed so far. From experience it is known that the values obtained by the simulation code are within a reasonable range, but conformity with experiments is not proved.

12.2. DEM-CFD Results for PSD-B

A coupled DEM-CFD simulation for the truncated particle-size distribution B with two velocity inlets is performed, see Figure 10.1. The velocity boundary conditions are equal to 0.25 m/s at the outer inlet and 0.2 m/s at the inner inlet. Both vectors point into the normal direction of the boundary face. The simulation is started with ramp boundary conditions for the temperature dependent quantities. Then the simulation run is proceeded until a stationary solution is obtained. Due to the coupling of the CFD with the DEM simulation, the data is noisy. Thus,

Die approbierte gedruckte Originalversion dieser Diplomarbeit ist an der TU Wien Bibliothek verfügbar
The approved original version of this thesis is available in print at TU Wien Bibliothek.

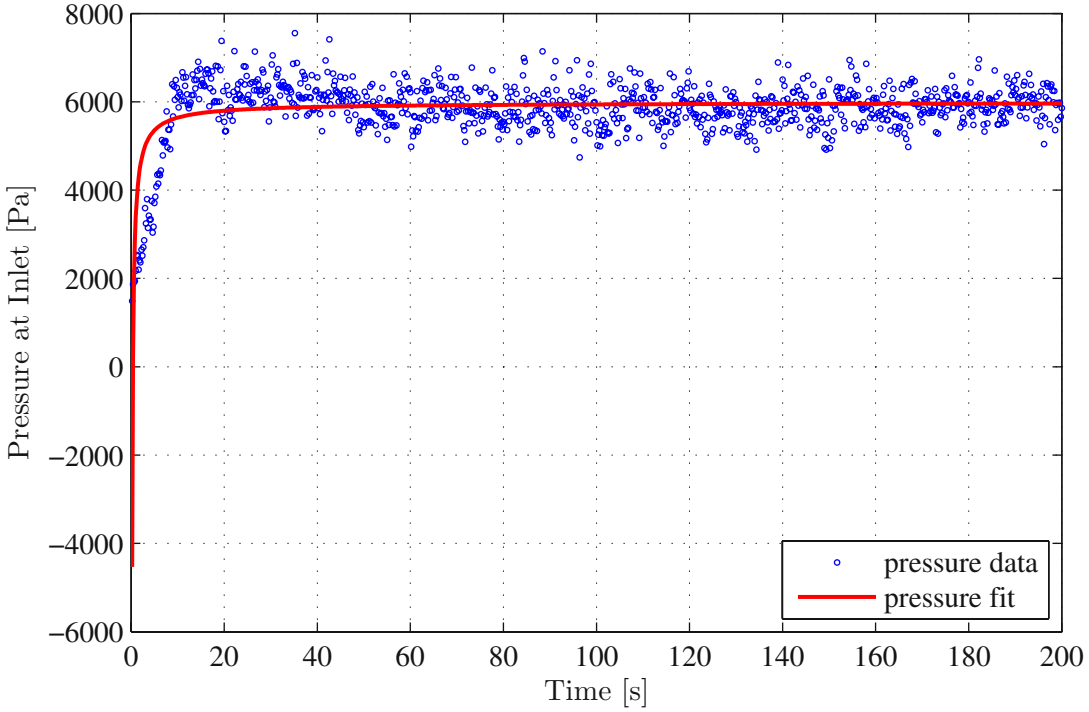

Figure 12.2.: Progression of the pressure drop across the sinter bed in the shaft cooler for a velocity boundary condition of 0.25 m/s at the outer and 0.20 m/s at the inner air inlet.

the time-average is calculated for the post-processing. The contour plots for the fluid phase and the particle temperature field are depicted in Figure 12.3.

As exemplified in 12.1.1, the fluid mass flow (and also the fluid volume flow) calculated from the boundary condition of the coupled DEM-CFD simulation does not correlate to the actual fluid-solid mass flow relation. The corrected fluid inlet boundary conditions are equal to 0.114 m/s at the outer inlet and 0.478 m/s at the inner inlet. This corresponds to a standard volume flow rate of 11 186 Nm^3/h at the outer inlet and 5816 Nm^3/h at the inner inlet.

The pressure drop across the sinter bed is monitored during the simulation and the measured values are fitted, see Figure 12.2. This value is in good agreement with the pressure drop in Figure 12.3 (a). However, there are two main reasons why the pressure drop obtained in the simulation might not resemble the actual value in a shaft cooler facility:

1) The inlet velocities in the simulation are not equal to the real values because of the area-ratio correction factors. For the outer inlet the correction factor is equal to 2.186, for the inner inlet it is equal to 0.4182. These values might counteract on each other, but the mass flow at the outer inlet is considerably higher. This may lead to an overprediction of the pressure loss.

Die approbierte gedruckte Originalversion dieser Diplomarbeit ist an der TU Wien Bibliothek verfügbar
The approved original version of this thesis is available in print at TU Wien Bibliothek.

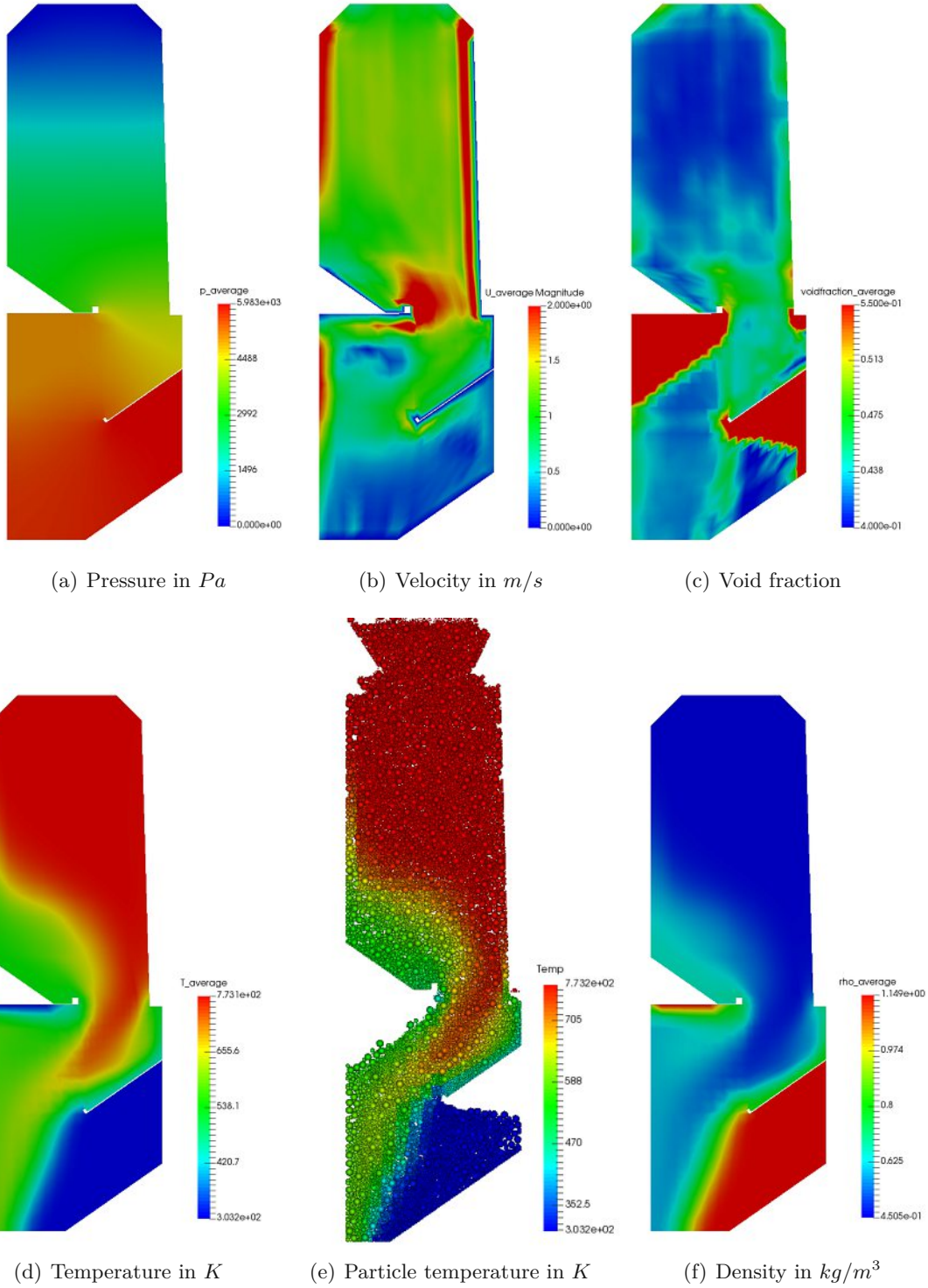

(a) Pressure in Pa (b) Velocity in m/s (c) Void fraction

(d) Temperature in K (e) Particle temperature in K (f) Density in kg/m^3

Figure 12.3.: Contour plots of the time-averaged fluid data and particle temperature field.

Die approbierte gedruckte Originalversion dieser Diplomarbeit ist an der TU Wien Bibliothek verfügbar
The approved original version of this thesis is available in print at TU Wien Bibliothek.

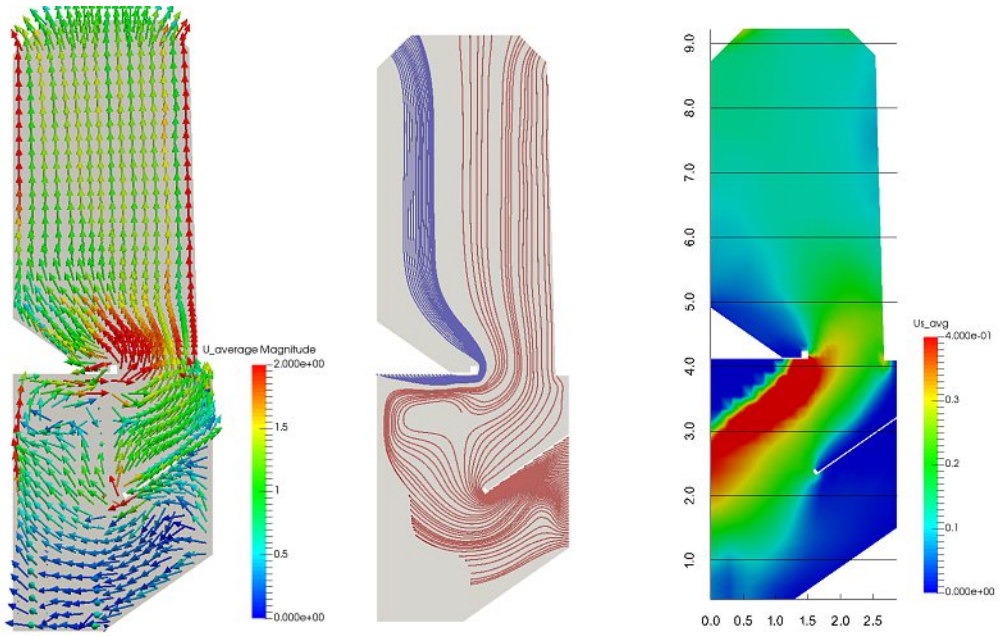

(a) Velocity vector field (b) Streamlines (c) Solid velocity contour

Figure 12.4.: Velocity vector plot and streamline plot for the fluid phase and time-averaged solid velocity contour plot.

2) An excessive time-scaling factor of 214 is used to achieve reasonable simulation time. Because of the strong influence on the solid velocity, the condition $u_f \gg u_s$ is not fulfilled anymore, see 6.6. Thus, the substantial increase of the relative velocity between fluid and particles leads to overestimation of the pressure drop.

Figure 12.3 (b) represents the fluid velocity field. The range is rescaled to emphasize the velocity peaks. Most of the hot spots can be explained on the basis of a higher void fraction, see Figure 12.3 (c). Also the geometrical constriction in the middle of the sinter cooler causes the fluid to speed up. The increased velocity at the outer wall and the symmetry axis is provoked by the void fraction on the one hand, and by the shorter distance through the particle bed due to the formation of an angle of repose on the other hand.

In the temperature plots in Figure 12.3 (d) and (e), the same dead zones as in 11.4 are identified. The temperature of the fluid and the solids is lower in these regions because of the higher residence-time of particles.
The area-averaged fluid outlet temperature amounts to 499.84 °C, which is almost equal to the solid inlet temperature of 500 °C. The reason for this vanishing temperature difference might be due to influence of the artificially increased particle velocity (time-scaling) on the particle Reynolds number (6.20) and consequently the impact on the Nusselt number (6.28) and the heat transfer coefficient (6.23). Furthermore, it can be questioned if the chosen Nusselt correlation

Die approbierte gedruckte Originalversion dieser Diplomarbeit ist an der TU Wien Bibliothek verfügbar
The approved original version of this thesis is available in print at TU Wien Bibliothek.

Table 12.3.: Mean particle outlet temperatures of PSD-B.

	overall	d_1	d_2	d_3
Mean temperature [°C]	213.58	212.61	225.79	265.95

according to Deen et al. [59] is suitable for the prevailing problem.
The overall mean particle temperature and the mean temperatures for the individual particle diameters of the truncated particle-size distribution B at the solid outlet are presented in Table 12.3. As expected, the mean temperature of the larger particles is higher than the one of the smaller particles. From this it follows that the truncation of the particle-size distribution has the consequence, that the largest and probably hottest particles are not represented in the simulation. Suggestions for possible workarounds are given in 13.2.

The density plot in Figure 12.3 (f) is in good accordance with the fluid temperature field. This corresponds to the assumption of the incompressible ideal gas law (6.6) applied in this simulation, which states that the density is a function of the temperature only.

The vector plot of the velocity field in Figure 12.4 (a) indicates that the inflowing air from the inner inlet turns immediately into the outer radial direction and rises to the top of the sinter cooler. This effect is also illustrated by the streamline plot in Figure 12.4 (b). Furthermore, it reveals that the air of the inner inlet (blue) takes the path along the symmetry axis and the air of the outer inlet (red) flows alongside the outer wall of the shaft cooler.

The solid velocity contour plot is depicted in Figure 12.4 (c). The contour shows the same pattern as the plots in Figure 11.6. Since the geometry for the DEM-CFD simulation is truncated at the bottom and top, the velocity peaks due to insertion and discharging are not depicted. The solid velocity profile at various heights of the shaft cooler is illustrated in Figure 12.5. The x-axis is normalized to the respective width of the sinter cooler geometry. The heights are specified in the vertical axis of Figure 12.4 (c).

Die approbierte gedruckte Originalversion dieser Diplomarbeit ist an der TU Wien Bibliothek verfügbar
The approved original version of this thesis is available in print at TU Wien Bibliothek.

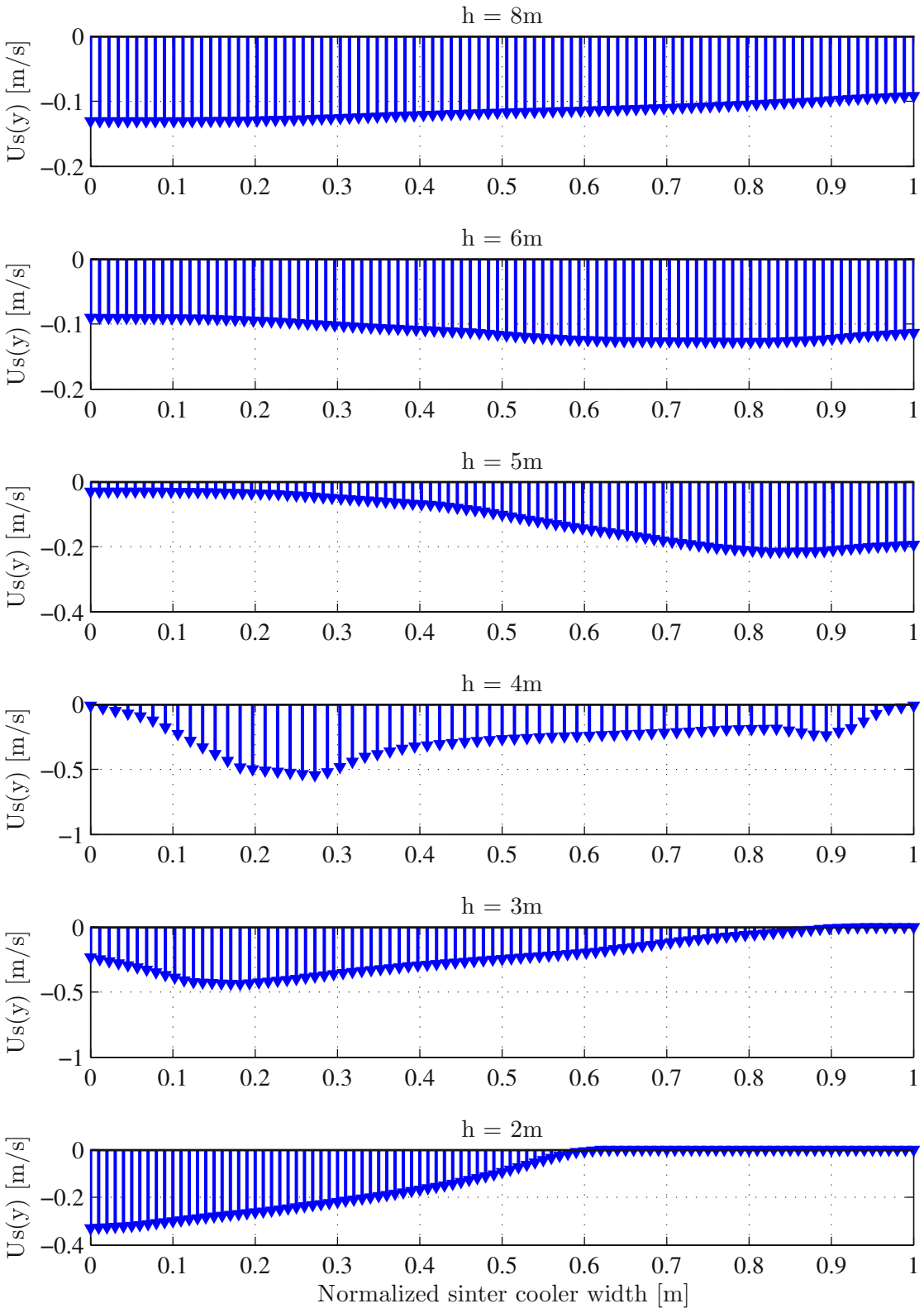

Figure 12.5.: Solid velocity profile at various heights of the sinter cooler, the heights are specified in the vertical axis of Figure 12.4 (b).

Die approbierte gedruckte Originalversion dieser Diplomarbeit ist an der TU Wien Bibliothek verfügbar
The approved original version of this thesis is available in print at TU Wien Bibliothek.

13. Conclusion and Outlook

The Discrete Element Method proves to be a suitable tool to investigate the solid flow in the sinter cooler facility. It provides the possibility to reproduce the influence of the cooler walls on the granular flow. Furthermore, effects such as segregation and the formation of dead zones or trajectories of particles moving through the shaft cooler are analyzed in detail with regard to the particle diameter and the particle-size distribution. The modification of the provided incompressible solver enables to account for the fluid density as a function of the temperature. This solver extension and the coupling of the software packages LIGGGHTS and OpenFOAM allows to examine the fluid flow in the sinter cooler. The effect of the heat transfer between the solid and the fluid phase on the corresponding temperature field is depicted as well as the pressure drop across the packed bed.

13.1. Model Assumptions

Throughout the course of this work, numerous models are applied to reduce the computation time. The involved assumptions affect simulation results, thus it is important to be aware of the consequences.

13.1.1. Solid Flow

- A coarse-graining approach is used to scale up the particles significantly. This might have an influence on the solid flow field.
- The DEM software LIGGGHTS does not support axial symmetric simulation domains (wedge shape). To reduce the number of particles for the calculations, a quasi-axisymmetric geometry is used.
- The particle size-distribution is truncated for the simulation, i. e. the large particles are not considered.
- A rolling-friction model is applied to account for non-spherical particle shapes (non-resolved approach).
- The EPSD rolling-friction model is employed. The associated rolling viscous damping coefficient is calibrated by an angle of repose test case, which does not account for coarse-graining.
- Temperature independent solid material properties are utilized, i. e. mean values with respect to the temperature range are calculated.

Die approbierte gedruckte Originalversion dieser Diplomarbeit ist an der TU Wien Bibliothek verfügbar
The approved original version of this thesis is available in print at TU Wien Bibliothek.

- Uniform particle temperature is assumed.

13.1.2. Fluid Flow and Heat Transfer

- A symmetric fluid domain is employed in the CFD simultion due to the use of a quasi-axisymmetric geometry in LIGGGHTS. The reason is that a axisymmetric CFD simulation requires a wedge-shaped domain, which would not be compatible with the domain of the DEM simulation. Since the area-ratio of the inlet and outlet faces are varied, the corresponding velocities have to be adapted to reflect the equivalent mass flow ratios. The altered velocities have an impact on the pressure drop and heat transfer.
- The diameter of the particles is in the range of the mesh cell size, which can cause problems for the exchange quantities of the coupled simulation, e. g. void fraction or momentum exchange.
- Fluid properties are assumed to be temperature independent and mean values with respect to the temperature range are used.
- The density is calculated according to the incompressible ideal gas law, i. e. the pressure influence is neglected.
- An incompressible turbulence model is used, although the compressibility effect of the temperature is considered.
- Extensive coarse-graining might have an impact on the calculation of the pressure drop and the convective heat transfer, although correction factors are introduced.
- The Nusselt correlation used in this work is obtained by a fit of data for Reynolds numbers in a range of 0 to 100. The occurrent particle Reynolds numbers are significantly higher though.
- The temperature of the large particles is not depicted due to the truncation of the particle-size distribution.

13.2. Improvements and Future Work

Many of the previously mentioned shortcomings have to be accepted due to limited computational power. Increased computing capacity enables the consideration of a higher number of particles, lower coarse-graining factors and even the simulation of a three-dimensional geometry. Alongside enhanced processing power, improved modeling approaches can be applied. Some concepts are given in the following.

Die approbierte gedruckte Originalversion dieser Diplomarbeit ist an der TU Wien Bibliothek verfügbar
The approved original version of this thesis is available in print at TU Wien Bibliothek.

- Further drag models are available in CFDEMcoupling. In a first test, the Koch-Hill [63] and Di Felice [64] drag models predict lower pressure drops than the Gidaspow drag model. More investigations have to be performed to identify the most suitable drag model for the sinter cooler simulation.
- Frictional heating of the solid material is not considered. Future versions of LIGGGHTS might include a model to account for this phenomenon.
- A chimera or overset mesh approach can be used to overcome the problem that particle diameter and mesh cell size are of the same order. The fluid flow is solved on a finer grid and exchange quantities between DEM and CFD simulation, such as momentum or energy source terms, are calculated on a coarser grid [44].
- The material parameters for the symmetry axis modeled as wall can be investigated in more detail. Further possibilities might be the reduction of the Young's modulus to allow for a higher overlap in the particle-wall contact or a velocity boundary condition in the solid flow direction can be applied to reproduce the influence of neighboring particles.
- A symmetric instead of a quasi-axisymmetric geometry can be used for the simulation to exclude the influence of the symmetry axis, see 11.2.
- A quarter-symmetric geometry can be used to account for three-dimensional effects.
- The DEM simulation can be coupled to a compressible OpenFOAM solver. The rhoPimpleFoam solver might offer better stability properties and a larger applicable time-step size. A compressible solver would also allow the utilization of other equations of state for the fluid phase, e. g. the ideal gas law.
- Use of a compressible turbulence model instead of an incompressible.
- More particle types can be defined in LIGGGHTS to assign different material properties, e. g. thermal capacity, or coarse-graining factors. This enables to account for the higher temperature of larger particles, which are truncated in the particle-size distribution.
- A resolved approach to model non-spherical particles can be applied, such as the multi-sphere method or superquadric particle shapes.
- The results of the DEM simulation might be used to calibrate a continuum model, which can be coupled to a CFD simulation more efficiently.
- The intra-particle temperature gradient can be analyzed using a model for non-uniform particle temperature. The open-source software package ParScale can be used for this purpose. ParScale stands for *'Particle Scale Models'* and it can be coupled to LIGGGHTS and CFDEMcoupling.

Die approbierte gedruckte Originalversion dieser Diplomarbeit ist an der TU Wien Bibliothek verfügbar
The approved original version of this thesis is available in print at TU Wien Bibliothek.

A. Nomenclature

A.1. List of Abbreviations and Acronyms

CDT	Constant Directional Torque
CFD	Computational Fluid Dynamics
CFDEM	Computational Fluid Dynamics Discrete Element Method
CFL	Courant-Friedrichs-Lewy
DEM	Discrete Element Method
DNS	Direct Numerical Simulation
DSMC	Direct Simulation Monte Carlo
EPSD	Elastic-Plastic Spring-Dashpot
FEM	Finite Element Method
GUI	Graphical User Interface
LAMMPS	Large-scale Atomic/Molecular Massively Parallel Simulator
LIGGGHTS	LAMMPS Improved for General Granular and Granular Heat Transfer Simulations
MD	Molecular Dynamics
MPI	Message Passing Interface
OpenFOAM	Open Field Operation And Manipulation
ParScale	Particle Scale Models
PSD	particle-size distribution

A.2. List of Symbols

Latin Symbols

A	area [m^2]
$\vec{a}$	particle acceleration [m/s^2]
c	Verlet parameter, skin parameter [m]
c_{cg}	coarse-graining factor [-]
C_D	drag coefficient [-]
c_p	thermal capacity, specific heat capacity [J/(kg K)]
C_r	the rolling viscous damping coefficient [N m s]
c_s	solid thermal capacity [J/(kg K)]
c_{ts}	time-scaling factor [-]
d_p	particle diameter [m]
D_T	thermal diffusivity [m^2/s]

Die approbierte gedruckte Originalversion dieser Diplomarbeit ist an der TU Wien Bibliothek verfügbar
The approved original version of this thesis is available in print at TU Wien Bibliothek.

E	energy [J]
e	coefficient of restitution [-]
$\vec{e}$	unit vector [-]
f_a	shape factor for the VDI Nusselt correlation [-]
$\vec{F_i}^f$	particle-fluid interaction force [N]
$\vec{F_i}^g$	gravitational force acting on a particle [N]
$\vec{F_{ij}}^c$	particle contact force [N]
$\vec{F_{ik}}^{nc}$	non-contact particle force [N]
G	shear modulus [N/m^2]
h	heat transfer coefficient [W/(m^2 K)]
h_f	fluid enthalpy [J/kg]
h_{ij}	inter-particle conductance [W/K]
I_i	particle moment of inertia [kg m^2]
I_{turb}	turbulent intensity [-]
k	turbulent kinetic energy [m^2/s^2]
k^n	normal elastic stiffness coeficient [N/m]
k_r	rolling stiffness [N m]
k^t	tangential elastic stiffness coeficient [N/m]
L_c	characteristic length scale [m]
l_{turb}	turbulent length scale [m]
m_i	particle mass [kg]
$\vec{M}_{ij}$	particle contact torque [N m]
$\dot{m}_s$	Mass flow [kg/s]
N_p	number of particles in the simulation domain [-]
p	pressure [Pa]
$\dot{Q}$	heat flux [W]
R	particle radius [m]
$\vec{r}$	particle position [m]
R_f	relative fluid desnsity [-]
R_s	specific gas constant [J/(kg K)]
S	shear stiffness [N/m]
$\vec{S}_e$	energy source term [W/m^3]
$\vec{S}_m$	momentum source term [N/m^3]
T	temperature [K]
t_H	Hertz time [s]
t_R	Rayleigh time [s]
U_0	superficial velocity [m/s]
$\vec{u}_f$	fluid velocity [m/s]
$\vec{u}_s$	solid velocity [m/s]

Die approbierte gedruckte Originalversion dieser Diplomarbeit ist an der TU Wien Bibliothek verfügbar
The approved original version of this thesis is available in print at TU Wien Bibliothek.

V	volume [m^3]
$\vec{v}$	particle velocity [m/s]
Y	Youngs' modulus [N/m^2]

Greek Symbols

α_f	void fraction, fluid volume fraction [-]
α_s	solid void fraction, solid volume fraction [-]
β	damping factor [-]
β_B	friction coefficient according to Gidaspow model B [$N\,s/m^4$]
γ	damping coefficient [$N\,s/m$]
Δ_{rel}	relative error [-]
Δt	time-step size [s]
Δx	smallest cell size of the CFD mesh [m]
$\Delta\theta_r$	incremental relative rotation [-]
η_r	rolling viscous damping ratio [-]
ε	turbulent kinetic dissipation [$J/(kg\,s)$]
$\dot{\theta}_r$	relative rolling angular velocity [1/s]
λ	thermal conductivity [$W/(m\,K)$]
μ	dynamic viscosity [$Pa\,s$]
μ_r	rolling-friction coefficient [-]
μ_s	sliding-friction coefficient [-]
ν	kinematic viscosity [m^2/s]
ν_{Po}	Poisson's ratio [-]
ξ_{ij}	spatial particle overlap [m]
ρ	density [kg/m^3]
σ	Courant number [-]
Φ	particle shape factor for the Ergun equation [-]
$\vec{\varphi}$	particle orientation [-]
$\vec{\omega}$	particle angular velocity [1/s]

Die approbierte gedruckte Originalversion dieser Diplomarbeit ist an der TU Wien Bibliothek verfügbar
The approved original version of this thesis is available in print at TU Wien Bibliothek.

Subscripts

cg	coarse-grained quantity
f	fluid quantity
i, j, k	particle indices
lam	laminar
n	normal component or quantity
p	particle
ref	reference value
s	solid quantity
t	tangential component or quantity
$turb$	turbulent

Superscripts

n	normal component or quantity
t	tangential component or quantity
$*$	effective or equivalent quantity of contacting particles

Dimensionless Quantities

Nu	Nusselt number
Pr	Prandtl number
Re	Reynolds number

Miscellaneous

∇	nabla operator

Die approbierte gedruckte Originalversion dieser Diplomarbeit ist an der TU Wien Bibliothek verfügbar
The approved original version of this thesis is available in print at TU Wien Bibliothek.

B. Governing Equations for Multiphase Flows

B.1. Compressible

The constitutive equations for compressible flows are discussed in [12], [49].

Continuity Equation

$$\frac{\partial(\rho_f \alpha_f)}{\partial t} + \nabla \cdot (\rho_f \alpha_f \vec{u}_f) = 0 \tag{B.1}$$

Momentum Equation

$$\frac{\partial(\rho_f \alpha_f \vec{u_f})}{\partial t} + \nabla \cdot (\rho_f \alpha_f \vec{u}_f \vec{u}_f) = \nabla \cdot (\mu_f \alpha_f \nabla(\vec{u}_f)) - \nabla p + \vec{S}_m(\rho_f) \tag{B.2}$$

Energy Equation

$$\frac{\partial(\rho_f \alpha_f h_f)}{\partial t} + \nabla \cdot (\rho_f \alpha_f \vec{u}_f h_f) = \underbrace{\nabla \cdot (\lambda_f \alpha_f \nabla(T_f))}_{Fourier\ law} + S_e \tag{B.3}$$

Substituting the enthalpy with $h_f = c_{p,f} T_f$ in (B.3) and in consideration of a constant specific heat capacity $c_{p,f} = const$, the energy equation can be written as follows

$$\frac{\partial(\rho_f \alpha_f T_f)}{\partial t} + \nabla \cdot (\rho_f \alpha_f \vec{u}_f T_f) = \nabla \cdot (\frac{\lambda_f}{c_{p,f}} \alpha_f \nabla(T_f)) + \frac{S_e}{c_{p,f}} \tag{B.4}$$

B.2. Incompressible

The incompressible governing equations according to [30] are given in this section. The compressible equations in B.1 can be transformed into the incompressible representation by division of the constant density $\rho_f = \rho_c = const$.

Continuity Equation

$$\frac{\partial(\alpha_f)}{\partial t} + \nabla \cdot (\alpha_f \vec{u}_f) = 0 \tag{B.5}$$

Die approbierte gedruckte Originalversion dieser Diplomarbeit ist an der TU Wien Bibliothek verfügbar
The approved original version of this thesis is available in print at TU Wien Bibliothek.

Momentum Equation

$$\frac{\partial(\alpha_f \vec{u}_f)}{\partial t} + \nabla \cdot (\alpha_f \vec{u}_f \vec{u}_f) = \nabla \cdot (\nu_f \alpha_f \nabla(\vec{u}_f)) - \nabla \overline{p} + \frac{\vec{S}_m}{\rho_c} \tag{B.6}$$

with the reduced pressure $\nabla \overline{p} = \frac{\nabla p}{\rho_c}$

Energy Equation

$$\frac{\partial(\alpha_f T_f)}{\partial t} + \nabla \cdot (\alpha_f \vec{u}_f T_f) = \nabla \cdot (D T_f \alpha_f \nabla(T_f)) + \frac{S_e}{\rho_f c_{p,f}} \tag{B.7}$$

with the thermal diffusivity $D_{T,f} = \frac{\lambda_f}{\rho_f c_{p,f}}$

Die approbierte gedruckte Originalversion dieser Diplomarbeit ist an der TU Wien Bibliothek verfügbar
The approved original version of this thesis is available in print at TU Wien Bibliothek.

C. Material Properties

To calculate reasonable mean values for the material properties, the polynomial as a functin of temperature for a certain quantity is averaged over the temperature range of the simulation. The polynomial functions of the material parameters are given in the corresponding section and the coefficients are summarized in Table C.1. The temperature ranges from the air inlet temperature to the sinter inlet temperature, i. e. from 30 °C to 500 °C. The mean of a function $y(x)$ is calculated as follows

$$\overline{y} = \frac{1}{b-a} \int_a^b y(x) dx \,, \tag{C.1}$$

where a is the lower and b is the upper limit.

Table C.1.: Polynomial coefficients for thermal conductivity (λ_s) and thermal capacity (c_s) of the sinter material, and dynamic viscosity (μ_f), thermal conductivity (λ_f) and thermal capacity ($c_{p,f}$) for dry air.

Coeff.	λ_s	c_s	μ_f	λ_f	$c_{p,f}$
a_0	2.05×10^{-4}	0	1.724×10^{-5}	0.02438	1006
a_1	1.93×10^{-4}	675	4.941×10^{-8}	7.576×10^{-5}	-0.008674
a_2	-8.48×10^{-8}	0.51	-3.068×10^{-11}	-3.661×10^{-8}	0.0006584
a_3	2.21×10^{-11}	-5.82×10^{-4}	2.142×10^{-14}	2.547×10^{-11}	-7.155×10^{-7}
a_4	0	4.34×10^{-7}	-6.766×10^{-18}	-7.903×10^{-15}	2.445×10^{-10}

C.1. Solid Material Properties

The thermal conductivity and thermal capacity for the sinter are derived from HSC, a software based on a thermochemical database to calculate material properties of chemical compounds.

The polynomial for the calculation of the thermal conductivity of the sinter material as a function of temperature can be expressed as

$$\lambda_s(T) = a_0 + a_1\, T + a_2\, T^2 + a_3\, T^3 + a_4\, T^4 \,, \tag{C.2}$$

where the temperature T has to be inserted in Kelvin.

Die approbierte gedruckte Originalversion dieser Diplomarbeit ist an der TU Wien Bibliothek verfügbar
The approved original version of this thesis is available in print at TU Wien Bibliothek.

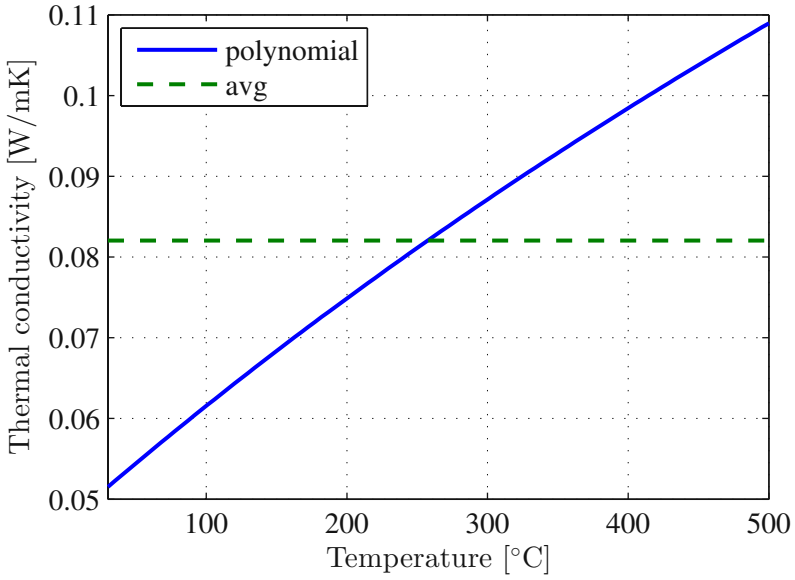

Figure C.1.: Thermal conductivity of the sinter as a function of temperature.

The polynomial for the thermal capacity of the sinter is derived from enthalpy values. It can be written as

$$c_s(T) = a_1 + 2\,a_2\,\left(T - T_{ref}\right) + 3\,a_3\,\left(T - T_{ref}\right)^2 + 4\,a_4\,\left(T - T_{ref}\right)^3\,, \tag{C.3}$$

with $T_{ref} = 298.15\,\mathrm{K}$ and the temperature T in Kelvin.

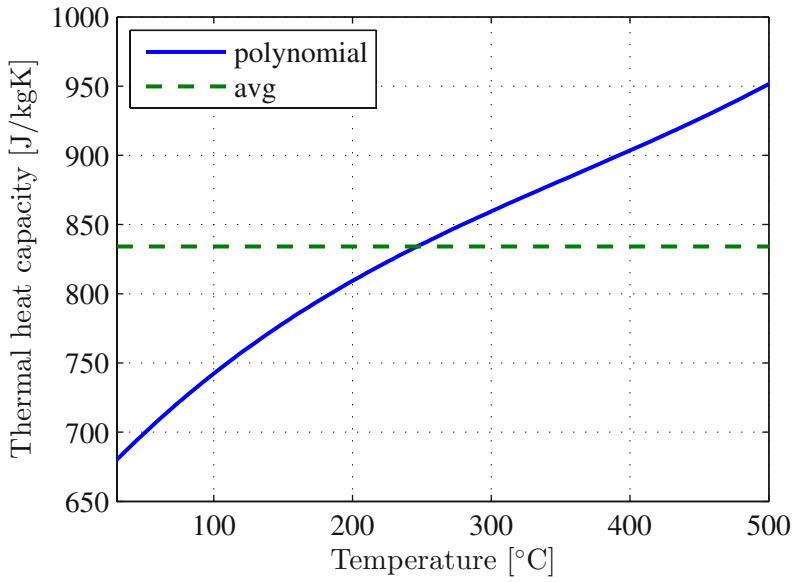

Figure C.2.: Thermal capacity of the sinter as a function of temperature.

Die approbierte gedruckte Originalversion dieser Diplomarbeit ist an der TU Wien Bibliothek verfügbar
The approved original version of this thesis is available in print at TU Wien Bibliothek.

C.2. Fluid Material Properties

In [57] the values for the material properties of dry air are tabulated. The data for the given temperature is fitted by a polynomial function so that the average value can be calculated according to (C.1). The polynomial for the dynamic viscosity, the thermal conductivity and the thermal capacity can be written in a general way

$$f(\vartheta) = a_0 + a_1\,\vartheta + a_2\,\vartheta^2 + a_3\,\vartheta^3 + a_4\,\vartheta^4\,, \tag{C.4}$$

where the function f is a place holder for the dynamic viscosity μ_f, thermal conductivity λ_f or thermal capacity $c_{p,f}$. The temperature ϑ has to be inserted in degree centigrade.

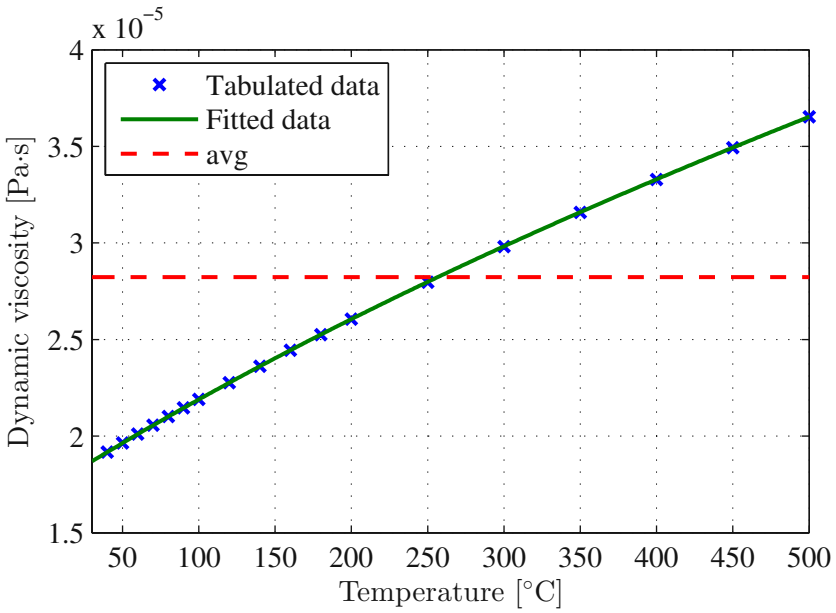

Figure C.3.: Dynamic viscosity of dry air as a function of temperature.

Die approbierte gedruckte Originalversion dieser Diplomarbeit ist an der TU Wien Bibliothek verfügbar
The approved original version of this thesis is available in print at TU Wien Bibliothek.

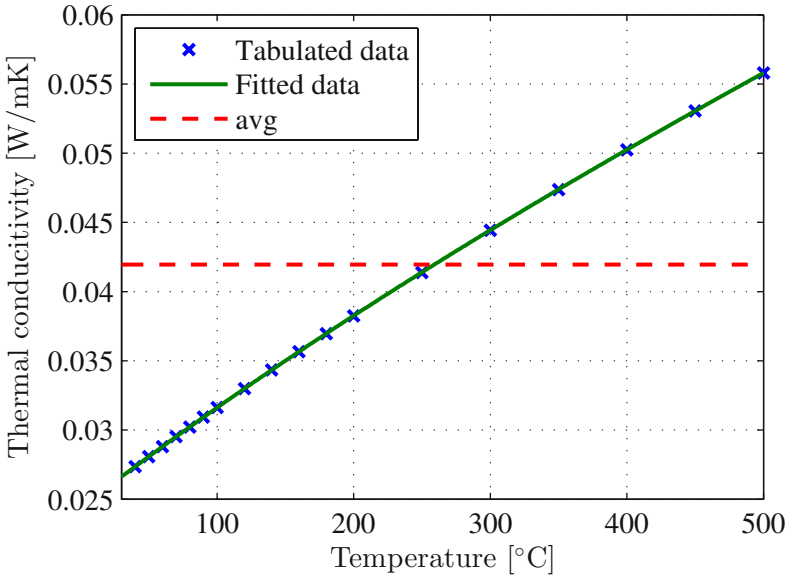

Figure C.4.: Thermal conductivity of dry air as a function of temperature.

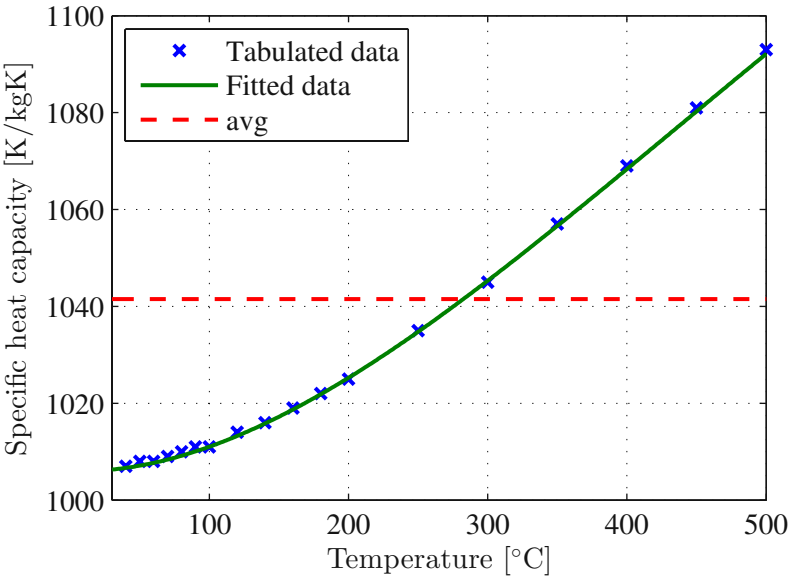

Figure C.5.: Specific heat capacity of dry air as a function of temperature.

Die approbierte gedruckte Originalversion dieser Diplomarbeit ist an der TU Wien Bibliothek verfügbar
The approved original version of this thesis is available in print at TU Wien Bibliothek.

Bibliography

[1] A. Ghosh and A. Chatterjee, *Ironmaking and steelmaking: Theory and practice*, 3. print, ser. Eastern economy edition. New Delhi: PHI Learning, 2010, ISBN: 9788120332898.

[2] A. Babich, *Ironmaking: Textbook*. Aachen: Mainz, 2008, ISBN: 9783861309970.

[3] X. Zhang, Z. Chen, J. Zhang, P. Ding, and J. Zhou, "Simulation and optimization of waste heat recovery in sinter cooling process", *Applied Thermal Engineering*, vol. 54, no. 1, pp. 7–15, 2013, ISSN: 13594311. DOI: 10.1016/j.applthermaleng.2013.01.017.

[4] M. Böberl, A. Wegerer, and S. Hötzinger, *The sinter shaft cooler: A highly energy-efficient solution for sinter cooling*, 2015.

[5] K. K. Rao and P. R. Nott, *An introduction to granular flow*, ser. Cambridge series in chemical engineering. Cambridge and New York: Cambridge University Press, 2008, ISBN: 978-0-511-45525-4.

[6] D. Schulze, *Pulver und Schüttgüter: Fließeigenschaften und Handhabung*, 3., erg. Aufl. 2014, ser. VDI-Buch. Berlin: Springer Vieweg, 2014, ISBN: 978-3-642-53884-1. DOI: 10.1007/978-3-642-53885-8.

[7] H.-G. Matuttis and J. Chen, *Understanding the Discrete Element Method: Simulation of Non-Spherical Particles for Granular and Multi-body Systems*. Hoboken: Wiley, 2014, ISBN: 978-1-118-56720-3.

[8] T. Pöschel and T. Schwager, *Computational granular dynamics: Models and algorithms*. Berlin: Springer, 2005, ISBN: 3-540-21485-2.

[9] W. R. Ketterhagen, J. S. Curtis, C. R. Wassgren, and B. C. Hancock, "Modeling granular segregation in flow from quasi-three-dimensional, wedge-shaped hoppers", *Powder Technology*, vol. 179, no. 3, pp. 126–143, 2008, ISSN: 00325910. DOI: 10.1016/j.powtec.2007.06.023.

[10] J. Sun, F. Battaglia, and S. Subramaniam, "Dynamics and structures of segregation in a dense, vibrating granular bed", *Physical Review E*, vol. 74, no. 6, 2006, ISSN: 1539-3755. DOI: 10.1103/PhysRevE.74.061307.

[11] C. Kloss, P. Seil, F. Hauzenberger, S. Amberger, C. Feimayr, S. Pirker, and C. Goniva, "Simulation of particle segregation in metallurgical furnaces for iron production", 2012.

[12] H. P. Zhu, Z. Y. Zhou, R. Y. Yang, and A. B. Yu, "Discrete particle simulation of particulate systems: Theoretical developments", *Chemical Engineering Science*, vol. 62, no. 13, pp. 3378–3396, 2007, ISSN: 00092509. DOI: 10.1016/j.ces.2006.12.089.

[13] C. T. Crowe, Ed., *Multiphase flow handbook*, ser. Mechanical engineering series. Boca Raton, FL: Taylor & Francis, 2006, ISBN: 0849312809. [Online]. Available: http://site.ebrary.com/lib/alltitles/docDetail.action?docID=10150652.

Die approbierte gedruckte Originalversion dieser Diplomarbeit ist an der TU Wien Bibliothek verfügbar
The approved original version of this thesis is available in print at TU Wien Bibliothek.

[14] A. Munjiza, *The combined finite-discrete element method*, Repr. Chichester: Wiley, 2005, ISBN: 0-470-84199-0.

[15] P. A. Cundall and O. D. L. Strack, "A discrete numerical model for granular assemblies", *Geotechnique*, vol. 29, no. 1, pp. 47–65, 1979, ISSN: 0016-8505.

[16] L. Verlet, "Computer experiments on classical fluids. i. thermodynamical properties of lennard-jones molecules", *Physical Review*, vol. 159, no. 1, pp. 98–103, 1967, ISSN: 0031-899X. DOI: 10.1103/PhysRev.159.98.

[17] Y. Li, Y. Xu, and C. Thornton, "A comparison of discrete element simulations and experiments for 'sandpiles' composed of spherical particles", *Powder Technology*, vol. 160, no. 3, pp. 219–228, 2005, ISSN: 00325910. DOI: 10.1016/j.powtec.2005.09.002.

[18] K. L. Johnson, *Contact mechanics*, 9. print. Cambridge: Cambridge Univ. Press, 2003, ISBN: 0521347963.

[19] O. R. Walton and R. L. Braun, "Viscosity, granular–temperature, and stress calculations for shearing assemblies of inelastic, frictional disks", *Journal of Rheology (1978-present)*, vol. 30, no. 5, pp. 949–980, 1986, ISSN: 0148-6055.

[20] A. Di Renzo and F. P. Di Maio, "Comparison of contact-force models for the simulation of collisions in dem-based granular flow codes", *Chemical Engineering Science*, vol. 59, no. 3, pp. 525–541, 2004, ISSN: 00092509. DOI: 10.1016/j.ces.2003.09.037.

[21] C. Kloss, *Liggghts documentation*. [Online]. Available: http://www.cfdem.com/.

[22] K. Iwashita and M. Oda, "Rolling resistance at contacts in simulation of shear band development by dem", *Journal of engineering mechanics*, vol. 124, no. 3, pp. 285–292, 1998, ISSN: 0733-9399.

[23] J. Ai, J.-F. Chen, J. M. Rotter, and J. Y. Ooi, "Assessment of rolling resistance models in discrete element simulations", *Powder Technology*, vol. 206, no. 3, pp. 269–282, 2011, ISSN: 00325910. DOI: 10.1016/j.powtec.2010.09.030.

[24] B. Chaudhuri, F. J. Muzzio, and M. S. Tomassone, "Modeling of heat transfer in granular flow in rotating vessels", *Chemical Engineering Science*, vol. 61, no. 19, pp. 6348–6360, 2006, ISSN: 00092509. DOI: 10.1016/j.ces.2006.05.034.

[25] R. Berger, C. Kloss, A. Kohlmeyer, and S. Pirker, "Hybrid parallelization of the liggghts open-source dem code", *Powder Technology*, vol. 278, pp. 234–247, 2015, ISSN: 00325910. DOI: 10.1016/j.powtec.2015.03.019.

[26] Z. Yao, J.-S. Wang, G.-R. Liu, and M. Cheng, "Improved neighbor list algorithm in molecular simulations using cell decomposition and data sorting method", *Computer Physics Communications*, vol. 161, no. 1-2, pp. 27–35, 2004, ISSN: 00104655. DOI: 10.1016/j.cpc.2004.04.004.

Die approbierte gedruckte Originalversion dieser Diplomarbeit ist an der TU Wien Bibliothek verfügbar
The approved original version of this thesis is available in print at TU Wien Bibliothek.

[27] M. P. Allen and D. J. Tildesley, *Computer simulation of liquids*, Reprint, ser. Oxford science publications. Oxford: Clarendon Press, 1990, ISBN: 0198553757.

[28] G. W. Delaney and P. W. Cleary, "The packing properties of superellipsoids", *EPL (Europhysics Letters)*, vol. 89, no. 3, p. 34 002, 2010, ISSN: 0295-5075.

[29] M. Theidel, *DEM-CFD Simulation dichter Fluid-Feststoff-Strömungen: Pneumatischer Transport von Schüttgut: Univ., Diss.–Bochum, 2011*, ser. Berichte aus der Energietechnik. Aachen: Shaker, 2011, ISBN: 978-3-8440-0354-3.

[30] C. Kloss, C. Goniva, A. Hager, S. Amberger, and S. Pirker, "Models, algorithms and validation for opensource dem and cfd-dem", *Progress in Computational Fluid Dynamics, An International Journal*, vol. 12, no. 2/3, p. 140, 2012, ISSN: 1468-4349. DOI: 10.1504/PCFD.2012.047457.

[31] C. S. Bierwisch, *Numerical simulations of granular flow and filling*. Citeseer, 2009, ISBN: 3832283382.

[32] C. Bierwisch, T. Kraft, H. Riedel, and M. Moseler, "Die filling optimization using three-dimensional discrete element modeling", *Powder Technology*, vol. 196, no. 2, pp. 169–179, 2009, ISSN: 00325910. DOI: 10.1016/j.powtec.2009.07.018.

[33] C. Bierwisch, T. Kraft, H. Riedel, and M. Moseler, "Three-dimensional discrete element models for the granular statics and dynamics of powders in cavity filling", *Journal of the Mechanics and Physics of Solids*, vol. 57, no. 1, pp. 10–31, 2009, ISSN: 00225096. DOI: 10.1016/j.jmps.2008.10.006.

[34] S. Radl, C. Radeke, J. Khinast, and S. Sunddaresan, Eds., *Parcel-based approach for the simulation of gas-particle flows*, 2011.

[35] S. Benyahia and J. E. Galvin, "Estimation of numerical errors related to some basic assumptions in discrete particle methods", *Industrial & Engineering Chemistry Research*, vol. 49, no. 21, pp. 10 588–10 605, 2010, ISSN: 0888-5885. DOI: 10.1021/ie100662z.

[36] C. O'Sullivan, *Particulate discrete element modelling: A geomechanics perspective*, 1st ed., ser. Applied geotechnics. Abingdon England: Taylor & Francis, 2011, ISBN: 9780415490368.

[37] S. C. Thakur, J. Y. Ooi, and H. Ahmadian, "Scaling of discrete element model parameters for cohesionless and cohesive solid", *Powder Technology*, 2015, ISSN: 00325910. DOI: 10.1016/j.powtec.2015.05.051.

[38] Y. Sheng, C. J. Lawrence, B. J. Briscoe, and C. Thornton, "Numerical studies of uniaxial powder compaction process by 3d dem", *Engineering Computations*, vol. 21, no. 2/3/4, pp. 304–317, 2004, ISSN: 0264-4401. DOI: 10.1108/02644400410519802.

[39] S. Plimpton, "Fast parallel algorithms for short-range molecular dynamics", *Journal of Computational Physics*, vol. 117, no. 1, pp. 1–19, 1995, ISSN: 00219991. DOI: 10.1006/jcph.1995.1039.

Die approbierte gedruckte Originalversion dieser Diplomarbeit ist an der TU Wien Bibliothek verfügbar
The approved original version of this thesis is available in print at TU Wien Bibliothek.

[40] S. Plimpton, *Lammps documentation*, March 2016. [Online]. Available: http://lammps.sandia.gov/.

[41] C. Goniva, *Cfdemcoupling documentation*, 2012. [Online]. Available: http://www.cfdem.com/.

[42] H. G. Weller, G. Tabor, H. Jasak, and C. Fureby, "A tensorial approach to computational continuum mechanics using object-oriented techniques", *Computers in Physics*, vol. 12, no. 6, p. 620, 1998, ISSN: 08941866. DOI: 10.1063/1.168744.

[43] C. J. Greenshields, *Openfoam user guide*, March 2015. [Online]. Available: http://cfd.direct/openfoam/user-guide/.

[44] C. Kloss and C. Goniva, Eds., *An open source CFD-DEM perspective*, 2010.

[45] C. Goniva, C. Kloss, and S. Pirker, Eds., *Towards fast parallel CFD-DEM: An open-source perspective*, 2009.

[46] A. B. Yu, "Powder processing: Models and simulations", in *Encyclopedia of Condensed Matter Physics*, Elsevier, 2005, pp. 401–414, ISBN: 9780123694010. DOI: 10.1016/B0-12-369401-9/00556-8.

[47] Y. Tsuji, T. Tanaka, and T. Ishida, "Lagrangian numerical simulation of plug flow of cohesionless particles in a horizontal pipe", *Powder Technology*, vol. 71, no. 3, pp. 239–250, 1992, ISSN: 00325910. DOI: 10.1016/0032-5910(92)88030-L.

[48] Y. Tsuji, T. Tanaka, and T. Ishida, "Lagrangian numerical simulation of plug flow of cohesionless particles in a horizontal pipe", *Powder Technology*, vol. 71, no. 3, pp. 239–250, 1992, ISSN: 00325910. DOI: 10.1016/0032-5910(92)88030-L.

[49] Z. Y. Zhou, S. B. KUANG, K. W. CHU, and A. B. Yu, "Discrete particle simulation of particle–fluid flow: Model formulations and their applicability", *Journal of Fluid Mechanics*, vol. 661, pp. 482–510, 2010, ISSN: 0022-1120. DOI: 10.1017/S002211201000306X.

[50] J. H. Ferziger and M. Perić, *Computational Methods for Fluid Dynamics*, third, rev. edition. Berlin, Heidelberg, s.l.: Springer Berlin Heidelberg, 2002, ISBN: 3-540-42074-6. DOI: 10.1007/978-3-642-56026-2. [Online]. Available: http://dx.doi.org/10.1007/978-3-642-56026-2.

[51] A. Hager, C. Kloss, S. Pirker, and C. Goniva, "Parallel open source cfd-dem for resolved particle-fluid interaction", *Journal of Energy and Power Engineering*, vol. 7, no. 9, p. 1705, 2013, ISSN: 1934-8975.

[52] A. Hager, C. Kloss, S. Pirker, and C. Goniva, "Parallel resolved open source cfd-dem: Method, validation and application", *The Journal of Computational Multiphase Flows*, vol. 6, no. 1, pp. 13–28, 2014, ISSN: 1757-482X. DOI: 10.1260/1757-482X.6.1.13.

Die approbierte gedruckte Originalversion dieser Diplomarbeit ist an der TU Wien Bibliothek verfügbar
The approved original version of this thesis is available in print at TU Wien Bibliothek.

[53] A. A. Shirgaonkar, M. A. MacIver, and N. A. Patankar, "A new mathematical formulation and fast algorithm for fully resolved simulation of self-propulsion", *Journal of Computational Physics*, vol. 228, no. 7, pp. 2366–2390, 2009, ISSN: 00219991. DOI: 10.1016/j.jcp.2008.12.006.

[54] S. Haeri and J. S. Shrimpton, "On the application of immersed boundary, fictitious domain and body-conformal mesh methods to many particle multiphase flows", *International Journal of Multiphase Flow*, vol. 40, pp. 38–55, 2012, ISSN: 03019322. DOI: 10.1016/j.ijmultiphaseflow.2011.12.002.

[55] ANSYS, *Fluent user's guide: Release 15.0*, November 2013.

[56] D. Gidaspow, *Multiphase Flow and Fluidization: Continuum and Kinetic Theory Descriptions*. San Diego: Elsevier Science, 1994, ISBN: 0-12-282470-9. [Online]. Available: http://site.ebrary.com/lib/alltitles/docDetail.action?docID=10597055.

[57] *VDI-Wärmeatlas: Mit 320 Tabellen*, 11., bearb. und erw. Aufl. Berlin: Springer Vieweg, 2013, ISBN: 9783642199813.

[58] J. Li and D. J. Mason, "A computational investigation of transient heat transfer in pneumatic transport of granular particles", *Powder Technology*, vol. 112, no. 3, pp. 273–282, 2000, ISSN: 00325910.

[59] N. G. Deen, E. Peters, J. T. Padding, and J. Kuipers, "Review of direct numerical simulation of fluid–particle mass, momentum and heat transfer in dense gas–solid flows", *Chemical Engineering Science*, vol. 116, pp. 710–724, 2014, ISSN: 00092509. DOI: 10.1016/j.ces.2014.05.039.

[60] D. J. Gunn, "Transfer of heat or mass to particles in fixed and fluidised beds", *International Journal of Heat and Mass Transfer*, vol. 21, no. 4, pp. 467–476, 1978, ISSN: 00179310. DOI: 10.1016/0017-9310(78)90080-7.

[61] L. Benvenuti and S. Pirker, "Materials2simulation2application: Primetals application report - 2015", 2015.

[62] ANSYS, *Fluent theory guide: Release 14.5*, October 2012.

[63] D. L. Koch and A. S. Sangani, "Particle pressure and marginal stability limits for a homogeneous monodisperse gas-fluidized bed: Kinetic theory and numerical simulations", *Journal of Fluid Mechanics*, vol. 400, pp. 229–263, 1999, ISSN: 0022-1120. DOI: 10.1017/S0022112099006485.

[64] R. Di Felice, "The particle-in-a-tube analogy for a multiparticle suspension", *International Journal of Multiphase Flow*, vol. 22, no. 3, pp. 515–525, 1996, ISSN: 03019322. DOI: 10.1016/0301-9322(96)00005-5.

Die approbierte gedruckte Originalversion dieser Diplomarbeit ist an der TU Wien Bibliothek verfügbar
The approved original version of this thesis is available in print at TU Wien Bibliothek.